

**On the Uncertainty of Biomechanical Modeling of the Aortic Wall in
Type B Dissections**

Lise Gheysen

Doctoral dissertation submitted to obtain the academic degree of
Doctor of Biomedical Engineering

Supervisors

Prof. Patrick Segers, PhD* - Prof. Nele Famaey, PhD** - Prof. Mathias Peirlinck, PhD***

* Department of Electronics and Information Systems
Faculty of Engineering and Architecture, Ghent University

** Department of Mechanical Engineering
Faculty of Engineering Science, KU Leuven

*** Department of BioMechanical Engineering
Faculty of Mechanical Engineering, Technische Universiteit Delft, the Netherlands

March 2024



ISBN 978-94-6355-819-8

NUR 954

Wettelijk depot: D/2024/10.500/24

Members of the Examination Board

Chair

Prof. Gert De Cooman, PhD, Ghent University

Other members entitled to vote

Annette Caenen, PhD, Ghent University

Prof. Cristina Cavinato, PhD, Université de Montpellier, France

Prof. Lucas Timmins, PhD, Texas A&M University, USA

Prof. Wim Van Paepegem, PhD, Ghent University

Supervisors

Prof. Patrick Segers, PhD, Ghent University

Prof. Nele Famaey, PhD, KU Leuven

Prof. Mathias Peirlinck, PhD, Technische Universiteit Delft, the Netherlands

Preface

More than five years ago, I started a hike. Equipped with well-suited shoes, a backpack and a map with some general directions, I started out full of courage, quickly realizing that many of the indicated paths were unexplored and challenging. Nevertheless, I knew that the most challenging paths often lead to the most beautiful destinations. Discovering new paths is exiting, but an almost unachievable task to complete alone. I had the luck that I could count on a lot of guides and supporters, each of them helping me to come a step closer to the amazing view at the end.

I would like to start by expressing my sincere appreciation to the members of my exam committee, to take the time to read this dissertation and enrich it with their insightful points of view. I am also grateful to the Research Foundation Flanders (FWO) to financially support this research. Of course, many thanks go out to my supervisors. Patrick, Nele and Mathias, thank you for guiding me from the start until the finish and giving me perspective at times when I couldn't see in which direction the path was going. Mathias, thank you for guiding me through the world of uncertainty and giving me the essential feedback to chose the road with the highest probability of success. Nele, without your expertise, I would be lost in the jungle of soft tissue biomechanics. Your critical questions and constructive feedback strongly helped me to stay on track. Patrick, thank you for giving me the opportunity to start this hike, for supporting me throughout all these years and for believing that I was able to reach the end, even at times when I doubted. In my opinion, a good supervisor has not only a strong expertise, but also supports people to develop their own expertise and grow as researcher as well as person. Having reached the destination, I am more than convinced that I had three very good supervisors, who guided me to this point!

Just as guidance is essential to keep on track, the support of colleagues is indispensable to find the courage to keep on moving forward at every stage.

To everyone in the STB group, thank you for welcoming me as a full member, even though we often met remotely. Thank you, for all the help, answers and clarifications! In particular, Klaas, it was always nice to know that we were following a very similar trajectory and that our paths crossed from time to time. Guillermo, thank you for all the positive energy during our update meetings. And of course, thank you, Lauranne! I don't think that you realize the importance of your support along the paths of soft tissue biomechanics, deposition stretches and growth and remodeling. Your patience, knowledge and explanations are certainly some of the key factors that helped in reaching the end.

It was a pleasure to have my base camp on the fifth floor of *Blok B* for more than five years. They often say that engineers are problem solvers. Well, Jurgen and Saskia, thank you for being the true engineers in the lab, always ready to solve all practical and organizational issues. Mathias and Gerlinde, thank you for showing me around on the fifth floor and introducing me into the world of research. I am glad that I could count on your advice during the first years! Matthias and Jolan, full of courage, we started our hike in the same year. It might have seemed impossible at some times, but the amazing view at the end is now coming very close for all of us! Good luck with the final steps! Annette and Yousof, for a long period, we made up the structural mechanics team of the group. Thank you for the fruitful discussions in structural mechanics language, for sharing the mysteries of Abaqus and for the nice non-work-related chats. Tim, Saar and Sarah, I really enjoyed working together during the sessions of *Maken, modelleren en meten, Zomerwijs* and the STEM-workshops! Sarah, we did not only collaborate in these projects, but also shared our office for more than four years. Together with Amith, we formed a coherent office team, already from the start. The discussions on all sorts of matter were the perfect afternoon breaks, the summary of how our weekends went, a perfect start of the week! I've really enjoyed our office vibe and with Simeon and Jellis joining later on, this vibe was fully continued. Although we moved to the new building, I still consider you as my office mates :-). Also outside the fifth floor, I felt a lot of support. Emma, we may not have been the fastest kayakers, but we made it and had, at least, the time to do teambuilding! Sarah, Amith, Tim, Jolan and Melissa, I appreciate it a lot that you did the effort to travel all the way to West-Flanders, some even via France ;-), to attend my concert! In brief, to all my colleagues at BioMMedA and MEDISIP, a big thank you! You all made the office so much more than just a place to work. Thanks to

you, the office was a place where work and fun collided and where serious talks were alternated by lighter topics. I doubt whether I will ever find a job where the lunch breaks are as relaxing as the ones we had in the kitchen!

Dan zijn er uiteraard nog de mensen die niet alleen in dit traject een grote rol gespeeld hebben, maar die bij alle tochten voor me klaarstaan.

Een grote dankjewel aan mijn familie en schoonfamilie! Jullie enthousiasme, lieve wensen en het meeleven bij kleine en grote gebeurtenissen in mijn leven doen me oprecht deugd. Simon, Louis, Laurent en Ruben, bedankt om mijn burgie-tijd op te fleuren met absurde humor en leuke gespreken, zowel in de beginjaren op de KULAK als later in het verre Leuven. Een speciale dankjewel daarbij aan Laurent en Simon voor het beantwoorden van mijn vele vragen en de gezellige babbels op kot! Esther, Elenora, Rebecca, Femke en Stien, op jullie steun en aanwezigheid kan ik al vele jaren rekenen! Dank jullie wel voor de vele leuke momenten die we al samen beleefd hebben! Niet in het minst onze avonden waarop ik alle stress kan loslaten en samen met jullie kan genieten. Ik kijk er alvast naar uit om binnenkort opnieuw de regelmaat van onze avonden samen op te drijven! Maxim, door jou voelde ik mij al heel snel thuis in het koor. Dankjewel voor de vele wandeltochten en de mooie vriendschap van de voorbije jaren. Dat er nog vele jaren mogen volgen!

Tot slot, zijn er nog enkele mensen, waarvoor geen enkel dankwoord kan uitdrukken hoe essentieel hun steun geweest is in het worden van de persoon die ik op vandaag ben.

Mama en papa, al heel mijn leven heb ik het geluk gehad om te mogen voelen hoe jullie naast me staan bij het zetten van elke stap, telkens op mijn manier en tempo, maar steeds in de wetenschap dat er een veilig vangnet is voor de moeilijkere passages. Dit was niet in het minst het geval tijdens mijn studies en de afgelopen vijf jaar, waarbij ik vaak niet wist welk pad ik moest volgen, hoe ik het kon bewandelen en dacht dat ik het fenomenale uitzichtpunt op het einde niet zou bereiken. Als ik vandaag kan genieten van het uitzicht, dan heb ik dat op zoveel vlakken aan jullie te danken! Een even grote dankjewel gaat uit naar jou, Lore! Jouw wijze raad, efficiënte aanpak en super-geluksbriefjes hebben mij op zoveel momenten de moed gegeven om door te zetten. Meer dan je waarschijnlijk zelf beseft, ben je mijn raadgever bij uitstek als ik er niet aan uit geraak hoe ik iets moet aanpakken. Uiteraard zijn onze gezellige babbels

minstens even essentieel! Dankjewel om gewoonweg de beste zus te zijn die een mens zich kan inbeelden! En Stijn, een dikke merci om mij te aanvaarden zoals ik ben, ondanks mijn beperkte liefde voor gezelschapsspelletjes! Ik geef het niet graag toe ;-), maar je bent stiekem wel een topschoonbroer! Lore en Stijn, samen met Noor en Thor vormen jullie een fantastisch gezin!

Iedere mens is uniek, maar soms ontmoet je toch iemand met wie er wel heel veel gelijkenissen zijn. Thomas, ik heb het geluk gehad om jou tegen te komen! Sindsdien heb ik er niet alleen een supporter bij, maar ook iemand die met mij meewandelt! Dankjewel om er gewoon te zijn, om de nodige flauwe (sorry ;-)) humor in huis te brengen, om te zijn wie je bent en van ons een topteam te maken! Ik kijk uit naar alle avonturen op ons eigen, onontgonnen pad! Want hoe uitdagend ze ook zijn... we kunnen het leven aan :-D! #Topteam for life!

Lise Gheysen

Table of contents

Preface	i
Table of contents	v
Abbreviations and symbols	xi
Summary	xv
Samenvatting	xxi
1 Introduction	1
1.1 Context	1
1.2 Outline	2
I Background	3
<hr/>	
2 Introduction into the pathophysiology of aortic dissections	5
2.1 Healthy aortic wall	5
2.1.1 Anatomy and function of the aorta	5
2.1.2 Microstructure of the aortic wall	6
2.2 Dissected aortic wall	8
2.2.1 Disease characterization and classification	8
2.2.1.1 Location	8
2.2.1.2 Duration	9
2.2.1.3 Complications	9
2.2.2 Adaptations in the microstructure of the dissected aortic wall	10
2.2.3 Origin of aortic dissections	11
2.2.4 Aortic dissection propagation	12
2.2.5 Treatment of aortic dissections	13

3	Biomechanical modeling of the dissected aortic wall	15
3.1	Nonlinear continuum mechanics	16
3.2	Acute mechanical aortic wall behavior	17
3.3	Axial load and residual stress	19
3.4	Growth and remodeling	21
3.4.1	Constrained mixture theory	22
3.4.2	Homogenized constrained mixture theory	24
3.5	Computational models of the dissected aortic wall	26
3.5.1	Acute dissected aortic wall models	26
3.5.1.1	Geometrically advanced models	26
3.5.1.2	Models with advanced material behavior	27
3.5.2	Growth and remodeling in dissected aortic wall models	28
4	Uncertainty quantification	31
4.1	Uncertainty quantification and sensitivity analysis	32
4.1.1	Sobol analysis	32
4.1.2	Delta moment-independent analysis	33
4.2	Surrogate modeling	33
4.3	Sampling strategies	35
4.3.1	Full factorial design	36
4.3.2	Random sampling	36
4.3.3	Latin hypercube sampling	36
4.3.4	Saltelli sampling	37
4.4	Uncertainty analysis in cardiovascular biomechanics	37
5	Problem statement	39
5.1	Problem statement	39
5.2	Objectives	40
II	Uncertainty in biomechanical dissected aortic wall models	41
6	Pulse wave velocity as measure to aid material parameter estimation	43
6.1	Introduction	43
6.2	Methods	45
6.2.1	Arterial reference model	45
6.2.1.1	Geometry, material and boundary conditions	45

6.2.1.2	GOH parameter selection	46
6.2.1.3	Metric for arterial stiffness	47
6.2.2	Reduction in GOH parameter space	47
6.2.2.1	Global reduction	47
6.2.2.2	Local reduction	48
6.2.3	Remaining uncertainty in material behavior . .	49
6.2.4	Practical implementation: Patient-inspired thoracic aorta	49
6.3	Results	50
6.3.1	Reduction in GOH parameter space	50
6.3.1.1	Global reduction	50
6.3.1.2	Local reduction	52
6.3.2	Remaining uncertainty in material behavior . .	53
6.3.3	Practical implementation: Patient-inspired thoracic aorta	54
6.4	Discussion	54
6.4.1	Extent of parameter space reduction	55
6.4.2	Relation of local reduction to the GOH para- meters	57
6.4.3	Remaining uncertainty with knowledge of PWV	58
6.4.4	Practical implementation: Patient-inspired thoracic aorta	58
6.4.5	Limitations	59
6.5	Conclusion	60
6.6	Appendix A: Verification case	61
6.7	Appendix B: Overview of number of parameter sets per $PWV_{110,t}$ interval	62
6.8	Appendix C: Parameter selection algorithm	63
6.9	Appendix D: Effect of variations in wall geometry . . .	64
7	Uncertainty quantification in an idealized dissected aortic wall	67
7.1	Introduction	67
7.2	Methods	69
7.2.1	Dissected wall model framework	70
7.2.1.1	Geometry and mesh	70
7.2.1.2	Material behavior	72
7.2.1.3	Finite element analysis	75
7.2.2	Uncertainty quantification of unknown thickness- and stiffness parameters	75
7.2.2.1	Input parameters and sampling	75
7.2.2.2	Output parameters	76

	7.2.2.3	Global uncertainty quantification based on finite element analyses . . .	77
	7.2.2.4	Parameter-specific contribution to global uncertainty based on surrogate models	77
	7.2.3	Additional sources of uncertainty	79
	7.2.3.1	Pressure gradient	79
	7.2.3.2	Axial dissection length	80
7.3	Results		80
	7.3.1	Reference dissected wall model	80
	7.3.2	Global uncertainty quantification based on finite element analyses	81
	7.3.3	Parameter-specific contribution to global uncertainty based on surrogate models	82
	7.3.3.1	Surrogate model of the dissected wall	82
	7.3.3.2	Delta moment-independent analysis	84
	7.3.4	Additional sources of uncertainty	85
	7.3.4.1	Pressure gradient	85
	7.3.4.2	Axial dissection length	85
7.4	Discussion		85
	7.4.1	Dissected wall model framework	85
	7.4.2	Global uncertainty quantification based on finite element analyses	87
	7.4.3	Parameter-specific contribution to global uncertainty based on surrogate models	88
	7.4.4	Physiological relevance of idealized dissected wall framework	89
	7.4.5	Lessons learned from surrogate modeling	90
	7.4.6	Limitations	92
7.5	Conclusion		93
7.6	Appendix A: Examples of maximal principal stress patterns		95
7.7	Appendix B: RMSE of Gaussian processes		96
7.8	Appendix C: Comparison of delta indices		97
7.9	Appendix D: Impact of direct coupling between the PWV_{ref} and GOH parameters		99

8 Growth and remodeling of the dissected membrane in an idealized dissected aorta 101

8.1	Introduction	101
8.2	Methods	103
	8.2.1 Model framework	103

8.2.1.1	Geometry	103
8.2.1.2	Acute material behavior	103
8.2.1.3	Loading and boundary conditions . .	105
8.2.2	Transition from acute to chronic dissection . .	106
8.2.2.1	Homogenized constrained mixture theory	106
8.2.2.2	Stress-mediated growth and remodeling	108
8.2.2.3	Inflammation-mediated growth and remodeling	108
8.2.2.4	Implications of the growth and remodeling algorithm	109
8.2.3	Parametric study of growth and remodeling parameters	110
8.2.3.1	Input parameters and sampling	110
8.2.3.2	Output parameters	111
8.3	Results	113
8.3.1	Parametric study of growth and remodeling parameters	113
8.3.2	Example cases	114
8.3.3	Thickening rates of the dissected membrane . .	115
8.3.4	Diameter expansion and volume change	115
8.3.5	Dissected membrane microstructure	117
8.4	Discussion	118
8.4.1	Limitations	123
8.5	Conclusion	124
8.6	Appendix A: Verification of slice model	126
8.7	Appendix B: Stress-mediated growth and remodeling of a healthy aortic wall	127
8.8	Appendix C: Thickening rates for the permanent inflammation patterns	128
8.9	Appendix D: Time evolution of example cases with a transient inflammation pattern	129
8.10	Appendix E: Parameter combinations with clinically observed thickening rates	130
8.11	Appendix F: Evolution of elastin and collagen content of two example samples	132

III General Discussion **135**

9 Conclusion and outlook **137**

9.1	Summary	137
-----	-------------------	-----

9.2	Discussion	139
9.2.1	Advancements in dissected aortic wall models .	139
9.2.2	Coupling between pulse wave velocity and con- stitutive parameters	139
9.2.3	Uncertainty in dissected aortic wall models . .	140
9.3	Limitations and future perspectives	141
9.3.1	Model assumptions and validation	141
9.3.2	Towards predictive dissection models	142
9.3.3	Reducing the model input uncertainty	143
9.3.4	The contribution of surrogate models	144
9.4	Take home message	146
	Bibliography	147
	Academic curriculum vitae	173

Abbreviations and symbols

The most commonly used abbreviations and symbols are summarized in the following list.

Abbreviations

2D	Two-dimensional
3D	Three-dimensional
4D	Four-dimensional
7D	Seven-dimensional
CT	Computed tomography
FL	False lumen
GOH	Gasser-Ogden-Holzapfel
GP	Gaussian process
GP _{<i>n</i>}	Gaussian process with <i>n</i> input parameters
HGO	Holzapfel-Gasser-Ogden
LHS	Latin hypercube sampling
LHS _{<i>n</i>}	Latin hypercube sampling with <i>n</i> samples
MPS	Maximal principal stress
MRI	Magnetic resonance imaging
PWV	Pulse wave velocity
RMSE	Root mean square error
TEVAR	Thoracic endovascular aortic repair
TL	True lumen

Symbols

α	Mean collagen fiber angle with respect to the circumferential direction
\mathbf{a}_g	Unit vector of the growth direction
\mathbf{C}	Right Cauchy-Green tensor
c_{10}	Elastin shear modulus

ABBREVIATIONS AND SYMBOLS

δ_i	Delta index of input parameter X_i
ΔU_{max}	Maximal distance between the dissected membrane and remaining wall
D_l^d	Diameter of part of the aortic lumen l at day d
ϵ	True strain tensor
e	Nominal strain tensor
E	Green-Lagrange strain tensor
$F^{(i)}$	Deformation gradient tensor (of constituent i)
F_{elas}^i	Elastic deformation gradient tensor of constituent i
F_g	Growth deformation gradient tensor
F_r^i	Remodeling deformation gradient tensor of constituent i
Γ_p	Permanent inflammation pattern as function of time
Γ_t	Transient inflammation pattern as function of time
g^c	Component of collagen deposition stretch in fiber direction
g_{ax}^e	Component of elastin deposition stretch in axial direction
g_{circ}^e	Component of elastin deposition stretch in circumferential direction
G^i	Deposition stretch tensor of constituent i
I	Identity matrix
I_j^i	j^{th} invariant of right Cauchy-Green tensor of constituent i with $j = 1, 4, 6$
κ	Collagen fiber dispersion
k_σ^i	Stress-mediated production rate of constituent i
$k_{\Gamma+}^i$	Inflammation-mediated production rate of constituent i
$k_{\Gamma-}^i$	Inflammation-mediated degradation rate of constituent i
k_1	Collagen fiber stiffness
k_2	Collagen fiber stiffening
$K_{GP}(\mathbf{x}, \mathbf{x}')$	Covariance or kernel function of Gaussian process
m^i	Mass production rate of constituent i in constrained mixture theory
M^f	Unit vector of the mean direction of a collagen fiber family
$m_{GP}(\mathbf{x})$	Mean function of Gaussian process
$MPS_{RW,max}$	Maximal principal stress at the location of maximal remaining wall displacement
$\Psi^{(tot)}$	(Total) strain energy density function per unit reference volume

$\Psi_{(j)}^i$	Strain energy density function per unit reference volume of constituent i (of layer j)
\mathbf{P}	1 st Piola-Kirchhoff stress tensor
PWV_p	Pulse wave velocity at a pressure of p mmHg
$PWV_{p,t}$	Target pulse wave velocity at a pressure of p mmHg
PWV_{ref}	Pulse wave velocity of a reference cylinder
q^i	Survival fraction of a mass fraction of constituent i in constrained mixture theory
ρ^i	Density of constituent i
$\dot{\rho}_+^i$	Production rate of constituent i in homogenized constrained mixture theory
$\dot{\rho}_-^i$	Degradation rate of constituent i in homogenized constrained mixture theory
R_{2D}	Local reduction in 2D parameter subspace
R_{7D}	Global reduction in 7D parameter space
R_e^l	Expansion rate of part of the aortic lumen l
R_T	Thickening rate of the dissected membrane
$\boldsymbol{\sigma}$	Cauchy stress tensor
\mathbf{S}	2 nd Piola-Kirchhoff stress tensor
T_{TW}	Total wall thickness
T_M	Medial wall thickness relative to the total wall
T_{DM}	Dissected membrane thickness relative to the media
T_{DM}^d	Absolute dissected membrane thickness at day d
\mathbf{U}	Stretch tensor
$U_{DM,max}$	Maximal displacement of the dissected membrane
U_{PWV}	Uncertainty in the global PWV-pressure behavior at 120 mmHg
$U_{RW,max}$	Maximal displacement of the remaining wall

Summary

CHAPTER 1 - INTRODUCTION

An aortic dissection is a disease in which a part of the aortic wall delaminates and a parallel channel for the blood flow, i.e. the false lumen, is formed. Severe complications, such as paraplegia and rupture, might occur if the disease is not properly treated. Despite the advancements in the treatment techniques, treated patients often suffer from dissection progression and/or the need for a reintervention. This indicates that the current treatment strategy is suboptimal. The development of computational models of aortic dissections can contribute to increased insight into the *in vivo* treatment effect and to determine the optimal patient-specific treatment of dissection patients. However, the clinical data is, up to now, often insufficient to determine all model parameters on a patient-specific basis. Quantifying the corresponding uncertainty on the model output parameters, caused by unknown or uncertain input parameters, is, therefore, essential in the further development of patient-specific dissection models.

PART I - BACKGROUND

Chapter 2 - Introduction into the pathophysiology of aortic dissections

The pathophysiology of aortic dissections, and how they are classified in clinical practice, is addressed. In this respect, the anatomy and microstructure of the healthy aortic wall is discussed, together with the adaptations in the case of a dissected aorta. Moreover, the current knowledge of the mechanisms that trigger the initiation and propagation of the dissection are considered as well as the clinical treatment strategies.

Chapter 3 - Biomechanical modeling of the dissected aortic wall

One of the essential components in biomechanical dissection models is the assumed mechanical behavior of the aortic wall. Therefore, this

chapter provides an overview of the most important characteristics of the material behavior, together with commonly applied techniques to model those. In this respect, the Gasser-Ogden-Holzapfel model is discussed as a constitutive law to represent the passive short-term, i.e. acute, arterial material behavior, which is anisotropic and hyperelastic. To reproduce a physiological response, accounting for the *in vivo* load is essential. To predict the mid- or long-term arterial behavior, growth and remodeling has to be included, for example by applying the (homogenized) constrained mixture theory.

In this respect, an overview of the existing computational dissected wall models is presented in this chapter. The acute behavior of the dissected wall has been modeled before, either with a strongly simplified geometry or material model. To date, only one model was developed that considered growth and remodeling, and thus the mid- and long-term behavior, of the dissected aortic wall.

Chapter 4 - Uncertainty quantification

Some techniques to quantify the uncertainty of an output of interest are summarized. Next to quantifying the resulting output uncertainty, the contribution of the individual input parameters can be assessed based on a global sensitivity analysis. As these analyses often require large amounts of samples, efficient sampling strategies as well as surrogate models are preferred. Gaussian process regression is considered more in detail as surrogate model, as it accounts for the remaining uncertainty on the considered output. Moreover, the full parameter space needs to be sampled, for which multiple sampling schemes are introduced.

Although global sensitivity analyses are currently non-existing in the domain of computational biomechanical modeling of aortic dissections, other types of uncertainty quantification related to aortic dissections have been performed. Some examples of global sensitivity analyses in other computational cardiovascular domains are presented as well.

Chapter 5 - Problem statement

Based on the need for an optimized patient-specific treatment decision as well as the current lack of uncertainty quantification in the framework of dissected aortic wall models, three specific objectives are defined for this dissertation. The first objective is to assess the uncertainty in healthy aortic wall behavior and the potential of pulse wave velocity to reduce this uncertainty. Quantifying the uncertainty

on the predicted wall stress and deformation of the dissected aorta as a consequence of uncertain geometrical and material parameters is the second objective. The third objective evaluates the feasibility to reproduce clinical observations regarding the growth and remodeling of the dissected aortic wall, despite the uncertainty in growth and remodeling parameters.

PART II - UNCERTAINTY IN BIOMECHANICAL DISSECTED AORTIC WALL MODELS

Chapter 6 - Pulse wave velocity as measure to aid material parameter estimation

Measuring the pulse wave velocity, which is the propagation speed of the arterial pulse, provides information on the arterial wall stiffness. As the ground-truth material parameters are usually unknown in a clinical context, the potential of clinical pulse wave velocity measurements to contribute to the parameter space reduction of a Gasser-Ogden-Holzapfel material, with seven independent parameters, is assessed. An idealized aortic wall model is, therefore, applied to quantify the corresponding reduction in the 7D parameter space and 2D subspaces as well as the uncertainty in global material behavior, represented by the relation between the blood pressure and the pulse wave velocity.

The results point out that pulse wave velocity measurements at lower pressures reduce the parameter space, and the corresponding uncertainty in global material behavior, mainly for combinations that show a stiff behavior at diastolic pressure. Pulse wave velocity measurements at higher pressures can, however, further enhance the reduction, in particular for parameter combinations that represent a compliant behavior at diastolic pressure. This reduction in parameter space, and uncertainty in global material behavior, is mainly caused by a reduction in the parameter subspaces related to the medial collagen fibers.

Chapter 7 - Uncertainty quantification of the wall thickness and stiffness in an idealized dissected aortic wall

As the default medical imaging practice for aortic dissections is restricted to computed tomography or magnetic resonance imaging, the thickness and stiffness of the dissected wall remains uncertain due to the absence of temporal and the limited spatial resolution of these imaging techniques. The impact of this uncertain information on the

predicted wall stress and deformation is, therefore, investigated. In this respect, an idealized pre-stressed dissected aortic wall model is developed in which the false lumen is deformed in response to the pre-stress release in the dissected membrane, and thus represents the deformation in the acute phase in a physiology-inspired manner.

This model is, then, utilized to quantify the uncertainty introduced by the unknown pulse wave velocity and total, medial and dissected membrane wall thickness. Based on a Latin hypercube, 300 samples of this input parameter space are modeled with a finite element analysis. The maximal principal stress, the false lumen size and the dissected membrane and remaining wall displacement are the output parameters of interest. The contribution of each input parameter to the output uncertainty is assessed based on a δ moment-independent global sensitivity analysis, which is applied to a surrogate Gaussian process regression model, which is trained using the finite element analyses.

Both the resulting wall deformations and stresses show large variations as a consequence of the input uncertainties, in particular when considering the extreme outcomes. The contribution of the input uncertainty depends on the considered output. Whereas the dissected membrane thickness has the largest impact on the resulting wall stress, the unknown pulse wave velocity is the major determinant for the modeled deformation of the dissected aortic wall.

Chapter 8 - Growth and remodeling of the dissected membrane in an idealized dissected aorta

A slice model of the idealized dissected aortic wall is subjected to the homogenized constrained mixture theory in an attempt to reproduce the clinically observed dissected membrane thickening and diameter expansion rate during the transition from the acute to the chronic phase. The evolution of the elastin and collagen content in the dissected membrane is assessed too. The growth and remodeling is assumed to be caused by a stress- and inflammation-mediated tissue response. Four inflammation patterns are applied, differing in duration, i.e. permanent or transient, and location, i.e. local or global. As no ground-truth values exist for the growth and remodeling parameters, a parametric study is performed to assess whether the clinical observations can be reproduced, despite this uncertainty.

A subset of parameter combinations results in the observed dissected membrane thickening rates for the transient inflammation patterns. These combinations, moreover, yield realistic total diameter

expansion rates and changes in elastin and collagen content, in particular for local inflammation around the false lumen.

PART III - GENERAL DISCUSSION

Chapter 9 - Conclusion and outlook

This dissertation considers the impact of uncertain parameters, related to the wall thickness and material behavior, on the predicted outcome of biomechanical dissected aortic wall models. Overall, the impact of the lack of input data on the resulting wall deformation and stress is rather large, which emphasizes the need for probabilistic rather than deterministic models. However, the use of idealized models and clinical measurements, such as the pulse wave velocity, might contribute to the reduction of the input parameter space and, thus, the corresponding output uncertainty.

Samenvatting

HOOFDSTUK 1 - INTRODUCTIE

Een aortadissectie is een aandoening waarbij een deel van de aortawand afscheurt. Hierdoor wordt er een parallel kanaal, meer bepaald het valse lumen, gevormd waar het bloed door kan stromen. Ernstige complicaties, zoals verlamming of het doorscheuren van de aortawand, kunnen hierbij optreden indien de aandoening niet op een geschikte manier behandeld wordt. Ondanks de evolutie in de ontwikkeling van behandelingstechnieken hebben patiënten frequent last van dissectie progressie en/of nood aan een bijkomende ingreep. Dit duidt erop dat de huidige behandelingsstrategie slechts suboptimaal is. De ontwikkeling van computationele modellen van aortadissecties kan bijdragen tot een verhoogd inzicht in de *in vivo* effecten van de behandeling en, bijgevolg, tot de ontwikkeling van een patiënt-specifieke behandeling voor aortadissecties. De beschikbare klinische data is tot op vandaag echter vaak onvoldoende om de nodige modelparameters te bepalen op een patiënt-specifiek niveau. Dit benadrukt de noodzaak om de onzekerheid op de berekende grootheden van deze computationele modellen, ten gevolge van de onbekende of onzekere ingangsparementers, te kwantificeren en op die manier de verdere ontwikkeling van patiënt-specifieke modellen voor aortadissecties mogelijk te maken.

DEEL I - ACHTERGRONDINFORMATIE

Hoofdstuk 2 - Introductie in de pathofysiologie van aortadissecties

De pathofysiologie van aortadissecties, en hoe ze geclassificeerd worden in de klinische praktijk, wordt besproken. Hierbij komen zowel de anatomie en de microstructuur van de gezonde aortawand aan bod, als de veranderingen die optreden bij een gedissecteerde aortawand. Er wordt bovendien een overzicht gegeven van de huidige

kennis over de initiatie en verdere ontwikkeling van aortadissecties, samen met de meest voorkomende klinische behandelingsstrategieën.

Hoofdstuk 3 - Biomechanisch modelleren van de gedissecteerde aortawand

Eén van de essentiële componenten van biomechanische dissectie-modellen is het veronderstelde mechanisch gedrag van de aortawand. Om deze reden, geeft dit hoofdstuk een overzicht van de belangrijkste karakteristieken van het materiaalgedrag en frequent gebruikte technieken om deze te modelleren. Hierbij aansluitend, wordt het Gasser-Ogden-Holzapfel model besproken als constitutieve wet om het passieve ogenblikkelijke materiaalgedrag, dat anisotroop en hyperelastisch is, weer te geven. Om het fysiologisch gedrag te reproduceren, is het noodzakelijk om de *in vivo* belasting in rekening te brengen. De voorspelling van het mechanische gedrag van de aortawand op middellange en lange termijn vereist de implementatie van de groei en hermodellering van het weefsel, wat kan gebeuren aan de hand van de (*homogenized*) *constrained mixture theory*.

Hierbij aansluitend, wordt in dit hoofdstuk een overzicht gegeven van de bestaande computationele modellen van de gedissecteerde aortawand. Het ogenblikkelijke gedrag van de gedissecteerde aortawand werd reeds gemodelleerd, waarbij ofwel de geometrie ofwel het materiaalmodel sterk vereenvoudigd werd. Tot op heden werd slechts één model ontwikkeld dat de groei en hermodellering, en dus het gedrag op (middel)lange termijn, van de gedissecteerde aortawand in beschouwing neemt.

Hoofdstuk 4 - Onzekerheidskwantificatie

Enkele technieken om de onzekerheid op de berekende grootheden te kwantificeren worden samengevat. Naast het kwantificeren van de variatie in de berekende grootheden, kan de bijdrage van iedere ingangparameter tot de totale onzekerheid bekeken worden aan de hand van een globale sensitiviteitsanalyse. Vermits dit soort analyses een selectie van een groot aantal punten in de parameterruimte vereist, is zowel het kiezen van een efficiënte strategie om de punten te selecteren als het opstellen van een surrogaatmodel aangeraden. Naar aanleiding hiervan, wordt de regressie van een Gaussisch proces meer in detail besproken. Dit surrogaatmodel houdt immers rekening met de resterende onzekerheid van de berekende grootheden. Bovendien, worden verschillende strategieën besproken om een selectie van punten te maken op basis van de volledige parameterruimte.

Hoewel globale sensitiviteitsanalyses momenteel afwezig zijn in het domein van computationele biomechanische modellen van aortadissecties, werden er reeds andere soorten onzekerheidskwantificaties uitgevoerd met betrekking tot aortadissecties. Bovendien worden ook enkele voorbeelden van globale sensitiviteitsanalyses in andere computationele cardiovasculaire domeinen weergegeven.

Hoofdstuk 5 - Probleemdefinitie

Op basis van de nood aan een geoptimaliseerde patiënt-specifieke beslissing voor de behandeling en het huidige gebrek aan onzekerheidskwantificatie in het domein van biomechanische modellen van gedissecteerde aortawanden werden er drie concrete doelstellingen gedefinieerd. De eerste doelstelling is om de onzekerheid in het materiaalgedrag van de gezonde aortawand te evalueren, samen met het potentieel van de puls golfsnelheid om deze onzekerheid te reduceren. Het kwantificeren van de onzekerheid op de gemodelleerde wandspanning en -vervorming van de gedissecteerde aorta als gevolg van onzekere materiaal- en geometrische parameters vormt de tweede doelstelling. De derde doelstelling bekijkt de mogelijkheid om klinische observaties met betrekking tot de groei en hermodellering van de gedissecteerde aortawand te reproduceren, ondanks de onzekerheid over de parameters voor groei en hermodellering.

DEEL II - ONZEKERHEID IN BIOMECHANISCHE MODELLEN VAN DE GEDISSECTEERDE AORTAWAND

Hoofdstuk 6 - Puls golfsnelheid als meting die bijdraagt tot het schatten van de materiaalparameters

Het meten van de klinische puls golfsnelheid, i.e. de propagatiesnelheid van de arteriële pulse, geeft informatie over de stijfheid van de arteriële wand. Aangezien de werkelijke materiaalparameters vaak ongekend zijn in een klinische context, wordt het potentieel van klinische puls golfsnelheidsmetingen om bij te dragen aan de reductie van de parameterruimte van een Gasser-Ogden-Holzappel materiaal, met zeven onafhankelijke parameters, geëvalueerd. Een geïdealiseerd model van de aortawand wordt bijgevolg gebruikt om de bijhorende reductie van de totale 7D parameterruimte en de 2D subruimtes in kaart te brengen, samen met de onzekerheid in globaal materiaalgedrag, voorgesteld door de relatie tussen de bloeddruk en de puls golfsnelheid.

De resultaten tonen aan dat metingen van de puls golfsnelheid bij lage drukken de parameterruimte en de bijhorende onzekerheid in globaal materiaalgedrag voornamelijk reduceren voor parametercombinaties die overeenkomen met een stijf materiaalgedrag bij diastolische druk. Metingen van de puls golfsnelheid bij hogere drukken kunnen, bovendien, de parameterruimte en onzekerheid in materiaalgedrag verder beperken, meer specifiek voor parametercombinaties die het gedrag van een soepele aortawand weergeven bij diastolische bloeddruk. Deze reductie van de parameterruimte en de onzekerheid in globaal materiaalgedrag is hoofdzakelijk te wijten aan reductie van de subruimtes van parameters gerelateerd aan de collageenvezels van de media.

Hoofdstuk 7 - Onzekerheidskwantificatie van de wanddikte en -stijfheid in een geïdealiseerde gedissecteerde aorta

Aangezien de standaard beeldvorming bij aortadissecties veelal beperkt is tot *computed tomography* of *magnetic resonance imaging*, blijft de dikte en stijfheid van de gedissecteerde aortawand onzeker door de afwezigheid van temporele en de beperkte spatiële resolutie van deze beeldvormingstechnieken. De impact van deze onzekere informatie op de voorspelde spanning en vervorming van de wand wordt, bijgevolg, onderzocht. Hiervoor wordt een geïdealiseerd model van een gedissecteerde aortawand, inclusief voorspanning, ontwikkeld, waarbij het valse lumen vervormt als reactie op het relaxeren van de voorspanning in het deel van de aortawand dat dissecteert. Op deze manier wordt de vervormde aortawand op een fysiologisch geïnspireerde manier verkregen.

Dit model wordt gebruikt om de onzekerheid te kwantificeren die geïntroduceerd wordt door onzekerheid in de puls golfsnelheid en de dikte van de totale wand, de media en het gedissecteerde membraan. Op basis van een *Latin hypercube* worden 300 punten in de parameterruimte gekozen die gemodelleerd worden op basis van een eindige elementen analyse. De maximale hoofdspinning, de grootte van het valse lumen en de verplaatsing van het gedissecteerde membraan en de resterende wand zijn de beschouwde berekende grootheden. De bijdrage van ieder van de ingangsparementen op de onzekerheid in de berekende grootheden wordt geëvalueerd op basis van een δ moment-onafhankelijke globale sensitiviteitsanalyse. Deze analyse wordt toegepast op een surrogaatmodel op basis van regressie van een Gaussisch proces dat opgesteld wordt door middel van de uitgevoerde eindige elementen analyses.

Zowel de resulterende vervormingen als spanningen van de gedissecteerde aortawand vertonen een grote variatie ten gevolge van de onzekerheid op de ingangsparameters, zeker wanneer de extreme waarden van de berekende grootheden in rekening worden gebracht. Welke bijdrage ieder van de ingangsparameters hiertoe levert, is afhankelijk van de berekende grootheden. Terwijl de dikte van het gedissecteerde membraan voor de grootste impact op de resulterende wandspanning zorgt, is de ongekende puls golfsnelheid de meest bepalende factor voor de gemodelleerde vervorming van de gedissecteerde aortawand.

Hoofdstuk 8 - Groei en hermodellering van het gedissecteerde membraan in een geïdealiseerde gedissecteerde aorta

Een geïdealiseerd model van de gedissecteerde aortawand wordt onderworpen aan de *homogenized constrained mixture theory*, in een poging om de klinische observaties met betrekking tot de snelheid van de membraanverdikking en de diameterexpansie, tijdens de evolutie van de acute naar de chronische fase, te reproduceren. De evolutie van de hoeveelheid elastine en collageen in het gedissecteerde membraan wordt ook geëvalueerd. De groei en hermodellering wordt verondersteld te zijn veroorzaakt door een spannings- en ontstekingsgedreven mechanisme. Vier patronen voor de ontsteking, verschillend qua duur, i.e. permanent of transiënt, en locatie, i.e. lokaal of globaal, worden beschouwd. Aangezien er tot op vandaag geen kennis is over de werkelijke waarde van de groei- en hermodelleringparameters, wordt er een parameterstudie uitgevoerd om na te gaan of de klinische observaties kunnen worden gereproduceerd, ondanks de onzekerheid met betrekking tot de ingangsparameters.

Een subset van de beschouwde parametercombinaties resulteert in de geobserveerde verandering van de gedissecteerde membraandikte, voor het transiënte ontstekingsgedreven mechanisme. Bovendien leiden deze parametercombinaties tot een realistische verandering in totale diameter expansie en hoeveelheid elastine en collageen, meer bepaald wanneer het ontstekingsgedreven mechanisme beperkt is tot de regio rond het valse lumen.

DEEL III - ALGEMENE DISCUSSIE

Hoofdstuk 9 - Conclusie en perspectieven

Deze thesis beschouwt de impact van onzekere parameters, gerelateerd aan de dikte en het materiaalgedrag, op het voorspelde res-

ultaat van biomechanische modellen van de gedissecteerde aortawand. Globaal gezien was de impact van ontbrekende data over deze parameters, op de resulterende vervorming en spanning van de gedissecteerde aortawand, eerder groot. Dit benadrukt de nood aan een probabilistisch, eerder dan een deterministisch, model. Desondanks, kan het gebruik van geïdealiseerde modellen en beschikbare klinische metingen, zoals de puls golfsnelheid, bijdragen tot een reductie van de grootte van de ingangsparemeterruimte en bijvolg van de gerelateerde onzekerheid op de berekende grootheden.

Introduction

1.1 CONTEXT

Aortic dissections, a disease characterized by a delamination of the inner part of the aortic wall, might lead to, for example, renal failure, paraplegia or aortic wall rupture if not treated properly [1–3]. Despite significant improvements in the treatment techniques and insight into the disease based on experimental and computational research during previous decades, the frequent occurrence of disease progression and need for reintervention indicates that the optimal treatment strategy for patients with a type B dissection, i.e. a dissection of the descending thoracic aorta, is yet to be determined [2, 4].

Computational models of aortic dissections have the potential to gain insight into the effect of the treatment on the acute situation and disease progression and might, therefore, contribute to the *a priori* determination of the optimal patient-specific treatment strategy. Different types of computational models are required to represent the aortic dissection and its response on a particular treatment strategy. Indeed, the interaction between the dissected aortic wall, blood flow and selected treatment defines the acute situation, while additional models of thrombus formation and soft tissue growth and remodeling will be required to assess the long-term outcome.

Developing clinically applicable models that predict the optimal patient-specific treatment is, therefore, not only technically challenging, it also requires a lot of non-invasive patient-specific information.

For the dissected aortic wall in particular, the clinical information is currently limited to computed tomography (CT) or magnetic resonance imaging (MRI) scanning, which provides the geometry of the lumen in the aortic wall. However, more details about the wall itself, along with its behavior and how it changes over time, cannot be retrieved from these data. This lack of data introduces uncertainty in the computational model input and, thus, on the predicted outcome. Insight into the impact of these uncertain input parameters on the outcome, both on the short- and long-term, is, consequently, a prerequisite for the further development of patient-specific models of type B aortic dissections to support clinical decision making. Therefore, this dissertation attempts to gain insight into the impact of uncertainty related to the knowledge gap between the clinical practice and the required input for biomechanical models of type B aortic dissections.

1.2 OUTLINE

In this context, more background is given on the state-of-the-art knowledge of aortic dissections, the related biomechanical computational models and uncertainty quantification in part I (chapters 2-4). Chapter 2 gives an overview of the current knowledge regarding the origin, characteristics and propagation of the disease as well as clinical treatment strategies. As computational models might contribute to an increased insight into the *in vivo* aortic wall behavior, chapter 3 discusses the most common techniques to model the short-term, i.e. acute, and long-term behavior of the aortic tissue. An overview of the existing computational models of dissected aortic walls is presented as well. Assessing the sensitivity of dissected wall models to uncertain or incomplete non-invasive data is essential to accurately interpret the results. Therefore, chapter 4 discusses some general methodologies to quantify the impact of uncertain input parameters and provides a brief overview of the existing research in the framework of aortic dissections related to uncertainty quantification. The problem statement and the specific objectives of this dissertation are defined in chapter 5.

Part II (chapters 6-8) consists of original research papers and focuses on quantifying the uncertainty in dissected aortic wall models as a consequence of the limited patient-specific clinical data. Finally, part III (chapter 9) discusses the implications of the results of chapters 6-8 on the further development of computational biomechanical models of aortic dissections.

I

Background

CHAPTERS

2	Introduction into the pathophysiology of aortic dissections	5
3	Biomechanical modeling of the dissected aortic wall	15
4	Uncertainty quantification	31
5	Problem statement	39

Introduction into the pathophysiology of aortic dissections

This chapter elucidates the current understanding of the pathophysiology of aortic dissections and the state-of-the-art clinical treatment strategies. First of all, the general anatomy and microstructure of a healthy aortic wall (section 2.1) is discussed. More information on the dissected aortic wall is provided in section 2.2. There, the disease characteristics and classifications, the state-of-the-art knowledge regarding the microstructural adaptations, disease origin, propagation and treatment of aortic dissections are summarized.

2.1 HEALTHY AORTIC WALL

2.1.1 Anatomy and function of the aorta

The aorta is the central artery of the human vascular system, transporting oxygenated blood from the heart towards the organs and buffering the pulsatile flow, ejected by the heart, to a more continuous flow downstream. This buffering is performed by the elastic behavior of the aortic wall, which distends upon blood ejection of the heart into the aorta, i.e. in the systolic phase, and gradually retains its

diameter in the diastolic phase, i.e. during relaxation and filling of the heart.

Divided by the diaphragm, the aorta can be split into a thoracic and an abdominal part (figure 2.1). Within the thoracic aorta, an ascending and descending part is distinguished, with the aortic arch in between. Multiple side branches sprout from the aorta with the aim of continuing the transport of oxygenated blood towards the organs. The brachiocephalic, left common carotid and left subclavian artery branch off the aortic arch. In the descending aorta, the celiac trunk, superior mesenteric, renal and inferior mesenteric arteries are the major side branches. Minor side branches, which are situated in between the ribs, are present as well.

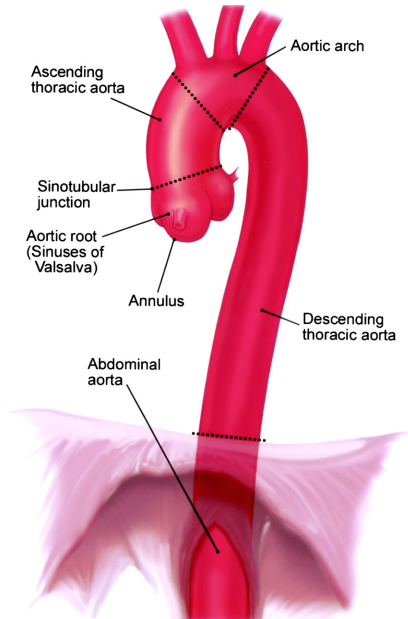


Figure 2.1: Anatomy of the aorta, with the side branches of the aortic arch. The diaphragm separates the thoracic from the abdominal aorta. This figure was adopted from Isselbacher et al. [5].

2.1.2 Microstructure of the aortic wall

The aortic wall consists of three layers, being the intima, media and adventitia (figure 2.2). The intimal layer, situated closest to the lumen, contains a single layer of endothelial cells supported by an elastic membrane, thus providing a negligible effect to the mechanical load bearing of the aortic wall [6]. The media and adventitia are considered as the most important aortic wall layers from a mechanical

perspective, with a respective thickness of 65-85% and 35-15% of the total wall [6–9]. In the thoracic part, where the aorta is an elastic artery, the medial layer consists of a series of elastic lamellae, which are interconnected by, amongst others, collagen fibers, smooth muscle cells, elastic fibers and glycosaminoglycans/proteoglycans [10]. More distally, the aortic wall shows more similarities to a muscular-type artery, in which the amount of smooth muscle cells increases and the layered structure of elastic lamellae in the media tends to disappear [11]. The adventitial layer primarily contains collagen fibers and a limited amount of elastin [12]. In the adventitia as well as in the outer part of the medial layer, the vasa vasorum is located, which is a network of blood vessels that supply oxygen and nutrition to the aortic wall [13]. While the media is assumed to contribute to the load bearing at physiological *in vivo* blood pressures, the main role of the adventitia is found at supra-physiological pressures [14].

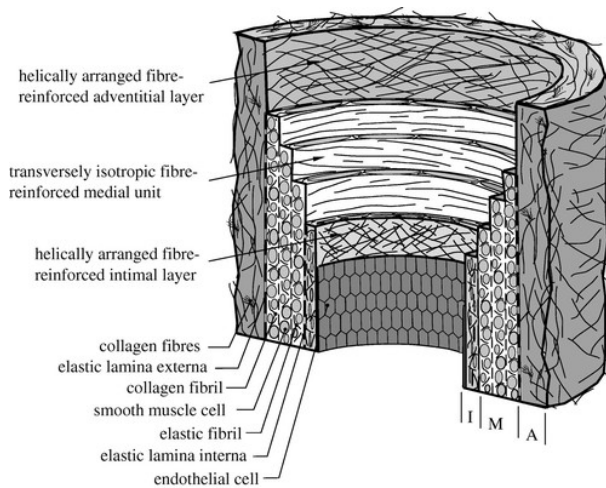


Figure 2.2: Schematic representation of the microstructure of the aortic wall, which is divided into the intimal (I), medial (M) and adventitial (A) layer. This figure was taken from Gasser et al. [15].

Both in the medial and adventitial layer, the collagen fibers are bundled in two to four families, which are dispersed within the circumferential-axial plane and, to a smaller extent, in the circumferential-radial plane [7, 16]. The mean angle of the collagen fibers differs between families and aortic wall layers. Indeed, while fiber angles of 0° to 45° (and -45° to 0°), with respect to the circumferential direction, were observed in the media, angles of 45° to 90° (and -90° to -45°) were found in the adventitia [7, 16]. Moreover, the collagen fibers have a wavy structure in the stress-free

state [17]. When a tensile force is exerted, the fibers start to stretch, which results in a stiffening behavior for an increasing elongation of the fibers. While the collagen fiber families cause a direction dependent, and thus anisotropic, behavior, the behavior exerted by the elastin and the smooth muscle cells, is commonly assumed to be isotropic [15, 18]. It is generally accepted that elastin and collagen provide the major contribution to the passive soft tissue behavior, while the smooth muscle cells allow the artery to actively respond in their contractile state [19, 20].

2.2 DISSECTED AORTIC WALL

2.2.1 Disease characterization and classification

An aortic dissection is a disease that is characterized by a delamination of the inner part of the thoracic aortic wall that contains one or multiple tears (figure 2.3). These allow the blood to enter the space between the delamination and the remaining part of the wall, which leads to the formation of a parallel channel, i.e. the false lumen, next to the normal pathway, i.e. the true lumen. This delamination of the wall is often referred to as the intimal flap or the dissected membrane and can either occur locally or extend from the ascending up to the abdominal aorta [21, 22]. Although the incidence rate is limited to 4.4-6.0/100,000, the consequences of an aortic dissection might be severe if the dissection is not properly treated [1, 23]. Indeed, a dissection can result in an expanded aortic diameter, branch vessel malperfusion, paraplegia and/or rupture of the aortic wall [1–3, 24].

Aortic dissections are commonly classified based on the location of the delamination, the duration of the symptoms and the presence or absence of complications [24].

2.2.1.1 Location

Both the Stanford and the DeBakey classification refer to the location of the dissection (figure 2.3). The Stanford classification distinguishes aortic dissections involving the ascending aorta, i.e. type A aortic dissections, from dissections which are limited to the descending part of the aorta, i.e. type B aortic dissections [26]. In case of type A dissections, the location of the entry tear, and thus the assumed origin of the dissection, is undetermined. An incidence rate of 58-71% and 42-29% was found for type A and B dissections, respectively [1, 23]. The DeBakey classification involves three classes, depending on the location of the entry tear [27]. A dissection of class I comprises both

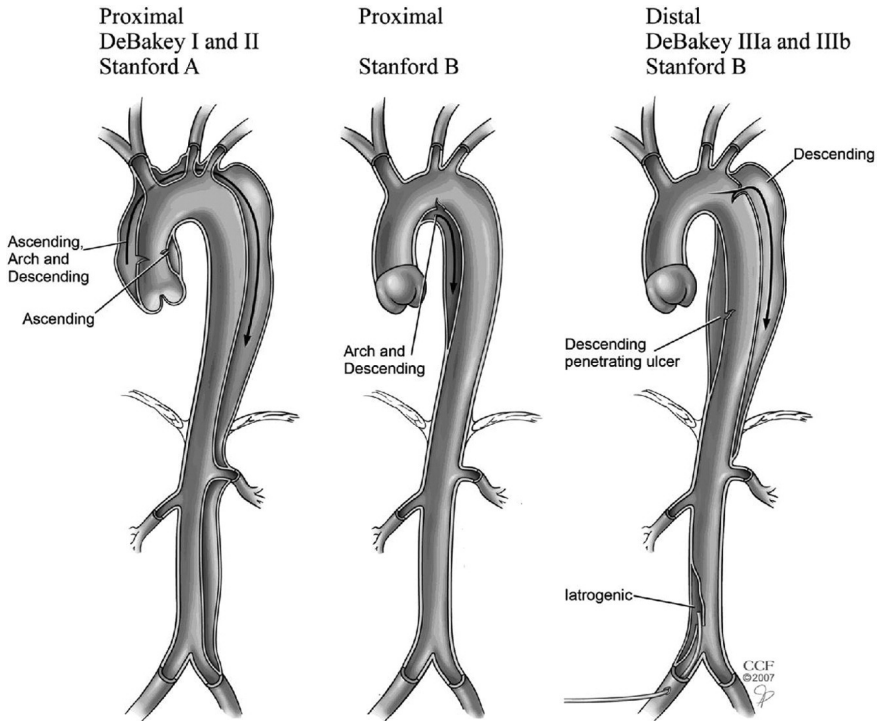


Figure 2.3: Overview of the Stanford and DeBakey classification system based on the dissection location. This figure was obtained from Hiratzka et al. [25].

the ascending and descending aorta with an entry tear in the ascending aorta. In class II, the dissection, and consequently the entry tear, is limited to the ascending aorta. Class III refers to dissections with an entry tear in the descending part of the aorta. In the remainder of this dissertation, the definitions of the Stanford classification are adopted.

2.2.1.2 Duration

The duration of the dissection refers to the time after the onset of the symptoms [24, 28]. A dissection is defined as acute within 14 days after the symptoms have started and as subacute within 2 weeks to 3 months. Thereafter, the dissection is defined as chronic.

2.2.1.3 Complications

A dissection is classified as complicated if one of the following complications is present: involvement of the aortic valve, cardiac tamponade, aortic wall rupture, malperfusion of branch vessels, dissection propagation, uncontrollable hypertension, uncontrollable clinical

symptoms, fast dilation of the false lumen and/or aortic diameter [24]. Otherwise, the dissection is defined as uncomplicated.

In particular for type B dissections, 25% of the cases was defined as complicated [29]. The mortality rate of type A dissections increases, as a rule of thumb, with 1%-2% per hour after onset of the symptoms and in-hospital mortality rates close to 60% were observed [30–32]. Type A dissections are, thus, all considered as life-threatening and the distinction between complicated and uncomplicated is not explicitly made.

2.2.2 Adaptations in the microstructure of the dissected aortic wall

Although the main constituents of the dissected aortic wall are the same as those of the healthy aorta, some microstructural adaptations have been observed in dissected aortas, already in the acute phase. Indeed, medial degeneration was present, which includes apoptosis of smooth muscle cells, fragmentation of elastic fibers and collagen degradation [33, 34]. Moreover, inflammatory cells, e.g. lymphocytes and macrophages, were found in the media, close to the false lumen, and in the adventitia [34, 35]. Similarly, an increased amount of glycosaminoglycans/proteoglycans, in particular localized in pools, was observed in aortic dissections [36, 37]. In this acute phase, the elastin concentration of the media was decreased compared to the healthy aorta, in particular when considering the circumferential direction [38, 39]. For collagen, decreased, similar and increased concentrations were observed in the media of dissected samples [38–40]. Other studies did not unambiguously indicate in which phase, i.e. acute, subacute or chronic, they considered the dissections and reported elastin fragmentation, elastin fiber loss, collagen defects and fibrosis in the medial layer [33, 41, 42]. In this respect, a clear decrease in elastin and increase in collagen in the medial layer was established [42, 43]. An increase in adventitial collagen was observed too [43]. It was, however, not specified whether the constituent increase/decrease was defined in terms of content or concentration.

The observed microstructural adaptations might affect the overall soft tissue behavior. Indeed, the acute dissected membrane was found to behave differently compared to the healthy aorta as a rather linear, but still anisotropic, behavior was observed [38]. Moreover, the behavior of the dissected membrane changes during the transition from the acute to chronic phase from highly dynamic to barely moving, which is most likely a consequence of the stiffening and thickening of the membrane [22, 44].

2.2.3 Origin of aortic dissections

Although hypertension, aortic atherosclerosis and connective tissue diseases, such as Marfan syndrome, have been frequently observed in patients with aortic dissections, the cause of initiation of an aortic dissection has not yet been elucidated [1, 2, 45–47].

Over the past decades, multiple theories have been proposed. On the one hand, it has been suggested that a tear in the inner layer of the aortic wall allowed the blood to enter the wall and, consequently, create a false lumen [48, 49]. The formation of this initial tear has been attributed to an elevated mean and systolic pressure as well as to the degree of anisotropy of the wall tissue, which is in particular weaker in the radial direction [50, 51]. On the other hand, it was pointed out that a bleeding within the aortic wall, potentially caused by rupture of the vasa vasorum, might be present before a tear in the dissected membrane occurs [49, 52, 53]. The importance of the vasa vasorum in the dissection initiation was formulated by Osada et al. too, based on the correspondence between the location of the vasa vasorum and the dissection, as both are often situated in the outer third of the media [54]. Besides, a correlation between the presence of inflammatory cells, e.g. macrophages and T lymphocytes, and aortic dissections was found [55–57]. Moreover, inflammatory cells have been associated with medial degeneration, which might indicate that inflammation plays a role in the formation of dissections [55, 57]. It is, however, not yet clear whether inflammation is the initiating factor or rather a consequence of the aortic dissection [57]. That the cause of dissection might originate within the wall, was put forward by Humphrey, Roccabianca et al. and Ahmadzadeh et al. as well [6, 58, 59]. They hypothesized that the dissection initiation is related to the formation of glycosaminoglycan/proteoglycan pools. The locally increased concentration of these substances, consequently, induces osmotic swelling in the medial layer, thus causing stress concentrations, which might form the origin of the dissection. Computational modeling of the glycosaminoglycan/proteoglycan pools and the related osmotic swelling, indeed, indicated that radial tensile stresses, instead of the expected compressive stress, in the range of the radial failure stress could be achieved [59]. While previous hypotheses focus on the local tissue microstructure, the aortic geometry was suggested to play a role too, as the presence of medial ruptures was linked to the location of minor and major aortic side branches [60, 61].

2.2.4 Aortic dissection propagation

Dissections have been found to propagate, in general, along the circumferential-axial plane in between elastic lamellae [62–64]. Nevertheless, some lamellae might be crossed during, in particular axial, propagation, which leads to damage in a region of up to 20% of the wall thickness [62, 63]. The specific propagation path, including the extent of retrograde propagation and which side branches are connected to the false lumen, was suggested to depend on the location of the initial tear along the aorta, the presence of material inhomogeneities and the collagen fiber direction [64–67]. Moreover, there is agreement that a dissection closer to the adventitial layer, and in particular in the outer third of the media, is associated with more dissection propagation, which means that the propagation occurs at a lower pressure, has a higher axial length and/or requires a smaller initial incision [48, 68–72]. Indeed, a larger area of initial damage was associated with propagation at a lower pressure [64, 65]. Recently, contradictory results were found for the axial stretch as Ban et al. linked a decreased axial stretch to a lower critical pressure, whereas Han et al. observed a lower critical pressure for an increasing axial stretch [64, 72]. Han et al. added that a lower critical pressure was also obtained for a lower residual stress [72].

The exact mechanism of dissection propagation has, however, not yet been elucidated. Some suggested that the propagation is triggered by the cyclic loading imposed by the blood flow [50], while others related the dissection propagation to the presence of shear within the aortic wall [73–75]. An important role has been attributed to the collagen fibers too [76]. In this respect, the limited resistance to shear in the circumferential-axial plane combined with the presence of shear as a consequence of material inhomogeneities has been thought to trigger rupture of the crosslinking fibers between the lamellae and, consequently, dissection propagation by connecting the local voids that are observed after the fiber rupture [73, 75]. On a larger scale, the aortic side branches were hypothesized to affect the dissection propagation, with minor side branches reinforcing and major side branches counteracting the propagation [61].

Moreover, no consensus has been reached on the degree of isotropy of the circumferential and axial dissection properties of the descending aorta. Indeed, anisotropy in the dissection propagation was suggested by Yu et al. and Horny et al., whereas Rios-Ruiz et al. found similar forces required to dissect the media [76–78]. Besides, the dissection properties were found to depend on the patient age and

the overall axial location along the aorta, while the variation within the descending thoracic aorta remained limited [77–79].

2.2.5 Treatment of aortic dissections

After diagnosis of an aortic dissection, for which computed tomography (CT) scanning as gold standard or magnetic resonance imaging (MRI) as alternative approach are used, three types of treatment can be applied, being optimal medical treatment, thoracic endovascular aortic repair (TEVAR) and open surgery [25, 29, 80–82]. Optimal medical treatment refers to providing the patient with drugs that are, in particular, aimed at controlling the blood pressure, heart rate and pain [25, 83]. TEVAR indicates a minimally invasive treatment that implies the deployment of a self-expanding stent-graft, comprising Nitinol struts, in the true lumen of the dissection. This treatment attempts to close off the proximal entry tear and, consequently, to trigger thrombus formation in and, thus, remodeling and healing of the false lumen [84]. The third treatment option is open surgery where the body is incised to externally replace the aortic wall at the location of the dissection [82, 85]. The optimal medical treatment to control the blood pressure and heart rate is part of the TEVAR and open surgery treatment too.

Depending on the dissection location, duration and the presence or absence of complications, different guidelines have been developed [25, 29, 81, 82]. Here, the focus is put on the treatment of type B dissections, as the less urgent nature of this type of dissections allows surgeons to define the treatment strategy *a priori*. Based on the guidelines, complicated acute type B dissections are commonly treated with TEVAR. Indeed, TEVAR was found to result in a decreased 1-year, but similar 5-year mortality rate compared to open surgery [86]. For uncomplicated acute dissections, the preferred treatment is still debatable. Previous guidelines recommended an optimal medical treatment in those cases [25, 29, 82]. However, recent studies indicate an improved long-term outcome for acute uncomplicated dissections, despite a similar outcome compared to the optimal medical treatment on the short-term [87]. Therefore, a tendency towards TEVAR as potential treatment for uncomplicated acute aortic dissections has been observed [81]. For chronic dissections, a different treatment of complicated and uncomplicated dissections is suggested as well [29, 82]. TEVAR is preferred over open surgery for complicated chronic dissections as it results in a decreased mortality and morbidity rate within 1 year after the treatment compared to open

surgery [88]. An uncomplicated chronic dissection is treated medically. For the optimal medical treatment as well as TEVAR, regular clinical follow-up with CT scans is strongly advised [29, 89].

Note that open surgery is rarely used for patients with a type B dissection, as this strongly invasive procedure is related to a high risk of infection and mortality rate [86–88]. It is, therefore, only applied if the dissection is considered unsuitable for TEVAR [29].

Despite the fact that TEVAR is often the treatment of choice, 20% to 30% of the patients needs a reintervention or shows an expanded aortic diameter within 1 year after the treatment [2, 4]. Moreover, in 9–78% of the patients, only partial thrombosis or no thrombosis at all has been obtained [47, 90, 91]. In this respect, partial thrombosis, which is observed in about 10% of the patients, was found to be a higher risk factor than a fully patent false lumen [47, 91–93]. Moreover, the long-term evolution of the true lumen expansion, the false lumen size and the total aortic diameter were found to depend on the timing of the treatment [94]. This indicates that, despite major improvements in the previous decades, the current treatment strategy is yet to be optimized.

Biomechanical modeling of the dissected aortic wall

In an attempt to elucidate doubts regarding the optimal patient-specific treatment of aortic dissections (chapter 2), computational models might provide additional insight into the *in vivo* situation or the anticipated progression of the disease and potential impact of an intervention. As a type B aortic dissection is the result of an interplay between the dissected aortic wall and the blood flow, accurate models of both aspects are required to capture the full treatment impact. Moreover, when being interested in the effect of the thoracic endovascular repair (TEVAR) treatment, the stent-graft deployment has to be accounted for. Although an understanding of the stent-graft deployment and the hemodynamics in an aortic dissection as well as its interplay with the dissected wall is important, this dissertation focuses on models of the dissected aortic wall.

Before going into the mechanical models of aortic dissections in particular, the biomechanical framework of aortic wall tissue is discussed, which shows a complex anisotropic hyperelastic material behavior and has the capability to grow and remodel. Some important aspects of the general framework of nonlinear continuum mechanics are considered in section 3.1. Section 3.2 covers the most important aspects to model the short-term, i.e. acute, behavior of the aortic wall. In section 3.3, the presence of stresses in the *in vivo* aortic wall is discussed. Some theoretical background on commonly applied

growth and remodeling algorithms is provided in section 3.4. Thereafter, section 3.5 summarizes the dissected aortic wall models that represent the acute situation and discusses the presence of growth and remodeling in dissection models.

3.1 NONLINEAR CONTINUUM MECHANICS

As the aortic wall exhibits large deformations during each cardiac cycle, it is described using a nonlinear continuum mechanics framework. Each line element $d\mathbf{X}$ of the initial or reference configuration Ω_0 is mapped to a line element $d\mathbf{x}$ on the current configuration Ω using a deformation gradient tensor \mathbf{F} , according to

$$d\mathbf{x} = \mathbf{F}d\mathbf{X} \text{ with } \mathbf{F} = \frac{\partial \mathbf{x}}{\partial \mathbf{X}}. \quad (3.1)$$

In cardiovascular applications, the large deformations are generally caused by the pressure load of the blood. The resulting deformation is quantified by the balance of linear momentum, which corresponds to

$$\nabla \cdot \boldsymbol{\sigma} + \mathbf{f}_b = \rho \mathbf{a}, \quad (3.2)$$

where $\boldsymbol{\sigma}$ refers to the Cauchy stress, \mathbf{f}_b to the body forces per unit mass, ρ to the mass density and \mathbf{a} to the acceleration, all expressed in the current configuration Ω . In the quasi-static cases, equation (3.2) simplifies to

$$\nabla \cdot \boldsymbol{\sigma} + \mathbf{f}_b = \mathbf{0}. \quad (3.3)$$

It is noteworthy that multiple definitions of stresses and strains exist in nonlinear continuum mechanics, depending on whether they refer to dimensions of the reference or current configuration. The three most commonly used combinations of stress and strain definitions are

- (1) Cauchy stress $\boldsymbol{\sigma}$ and true or logarithmic strain $\boldsymbol{\varepsilon}$

$$\boldsymbol{\sigma} = \frac{d\mathbf{f}}{nda} \text{ and } \boldsymbol{\varepsilon} = \ln(\mathbf{U}) \quad (3.4)$$

- (2) 1st Piola-Kirchhoff stress \mathbf{P} and nominal strain \mathbf{e}

$$\mathbf{P} = \frac{d\mathbf{f}}{NdA} \text{ and } \mathbf{e} = \mathbf{U} - \mathbf{I} \quad (3.5)$$

- (3) 2nd Piola-Kirchhoff stress \mathbf{S} and Green-Lagrange strain \mathbf{E}

$$\mathbf{S} = \frac{\mathbf{F}^{-T}d\mathbf{f}}{NdA} \text{ and } \mathbf{E} = \frac{1}{2}(\mathbf{U}^2 - \mathbf{I}). \quad (3.6)$$

In these definitions, \mathbf{U} indicates the stretch tensor, \mathbf{I} the identity matrix and dA and da represent an infinitesimal area in the reference and current configuration with respective normal vectors \mathbf{N} and \mathbf{n} . The normal force on area a in the current configuration is indicated as \mathbf{f} .

The different types of stresses can be transformed into each other. The expressions of $\boldsymbol{\sigma}$ as function of \mathbf{P} and \mathbf{S} are given by

$$\boldsymbol{\sigma} = J^{-1}\mathbf{P}\mathbf{F}^T \text{ and} \quad (3.7)$$

$$\boldsymbol{\sigma} = J^{-1}\mathbf{F}\mathbf{S}\mathbf{F}^T, \quad (3.8)$$

where J indicates the determinant of \mathbf{F} . In this dissertation, the reported stresses and strains correspond to the Cauchy stress, $\boldsymbol{\sigma}$, and true strain, $\boldsymbol{\varepsilon}$, respectively.

3.2 ACUTE MECHANICAL AORTIC WALL BEHAVIOR

The material of the aortic wall is commonly described as (quasi-) incompressible and hyperelastic, which implies that the Cauchy stress $\boldsymbol{\sigma}$ can be expressed as

$$\boldsymbol{\sigma} = \frac{\partial \Psi}{\partial \mathbf{F}}\mathbf{F}^T - p\mathbf{I}, \quad (3.9)$$

where Ψ is a strain energy density function, \mathbf{I} the identity tensor and p a Lagrange multiplier, which is included to account for the contribution of hydrostatic pressure stress.

Depending on the modeled material behavior and the required accuracy, different forms of Ψ can be applied. One of the most common formulations in arterial biomechanics is the Gasser-Ogden-Holzapfel (GOH) model. This model describes the aortic material as an additive decomposition of strain energy fractions coupled to the isotropic matrix material, which represents the extracellular matrix that mainly contains elastin, and two anisotropic dispersed collagen fiber families [15]. The corresponding strain energy density function is defined as

$$\Psi = c_{10}(I_1 - 3) + \frac{k_1}{2k_2} \left(\sum_{j=4,6} e^{k_2(\kappa I_1 + (1-3\kappa)I_j - 1)^2} - 1 \right), \quad (3.10)$$

with c_{10} being the elastin shear modulus, k_1 the collagen fiber stiffness, k_2 the fiber stiffening and κ the fiber dispersion (figure 3.1).

The invariants of the right Cauchy-Green tensor \mathbf{C} , with $\mathbf{C} = \mathbf{F}^T \mathbf{F}$, are indicated by I , meaning that I_1 and I_j with $j = 4, 6$, respectively, correspond to the first, fourth and sixth invariant. They are determined according to

$$I_1 = \text{Tr}(\mathbf{C}) \quad (3.11)$$

$$I_j = \mathbf{M}^j \cdot \mathbf{C} \mathbf{M}^j, \quad (3.12)$$

with Tr referring to the trace of the considered tensor and \mathbf{M}^j to the mean fiber direction of the considered fiber family. Note that I_j depend via \mathbf{M}^j on the mean collagen fiber angle α , which is defined with respect to the circumferential direction.

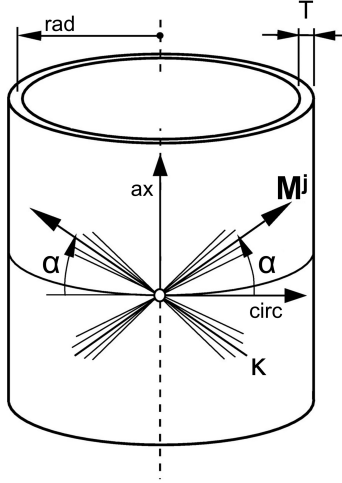


Figure 3.1: Schematic representation of a pressurized artery with a wall thickness T and a Gasser-Ogden-Holzapfel material that contains two dispersed collagen fiber families, with dispersion κ , mean fiber direction \mathbf{M}^j and mean fiber angle α , embedded in an isotropic elastin matrix. The radial, circumferential and axial direction are, respectively, indicated as ‘rad’, ‘circ’ and ‘ax’. This figure was adapted from Gasser et al. [15].

Variations on this framework have been presented by excluding the collagen fiber dispersion [95], indicated as the Holzapfel-Gasser-Ogden (HGO) material model, or including two additional collagen fiber families [96], asymmetric out-of-plane dispersion [16] or the effect of smooth muscle cells, which is integrated in Ψ in a similar manner as the contribution of collagen [97]. In this dissertation, the GOH and the HGO model were, respectively, applied in chapters 6-7 and chapter 8.

3.3 AXIAL LOAD AND RESIDUAL STRESS

The aortic wall is in its *in vivo* pressurized state during the cardiac cycle, thus, containing stresses. Moreover, even if the pressure load caused by the blood flow is removed, some stresses remain in the tissue. Indeed, when excising a portion of the arterial tissue during surgery, the tissue shrinks axially and opens circumferentially, as schematically represented in figure 3.2 [98, 99]. This indicates that the aortic tissue is, even in its zero-pressure state, not completely stress-free. While the axial shrinking indicates the presence of an axial *in vivo* load, the remaining circumferential stresses are referred to as the residual stresses.

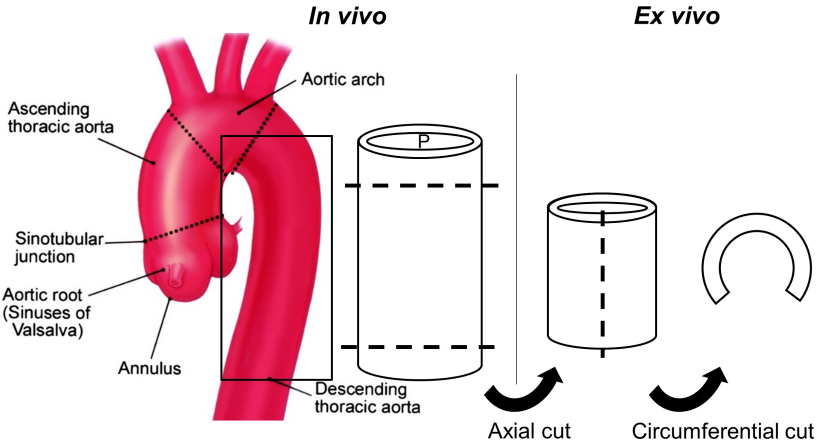


Figure 3.2: Schematic representation of the *in vivo* and *ex vivo* descending aorta, where the presence of *in vivo* stresses is visualized through the effect of an axial and circumferential cut. This figure was adapted from Isselbacher et al. [5].

The importance of including these residual stresses and axial loads in models of the arterial wall was emphasized as it affects the predicted stresses and strains [100–102]. The axial load, and its corresponding shrinking, is experimentally determined by measuring the length difference between a tissue portion before and after excising it from the body [98, 103]. The *in vivo* axial stretch was found to vary between 1.05 and 1.43 and to depend on the considered wall layer, axial location and patient’s age [103–106]. The circumferential residual stresses and strains were commonly quantified by measuring the opening angle obtained by axially cutting a cylindrical portion of the aortic wall, resulting in aortic opening angles between 57° and 257°

[105, 107, 108]. However, this opening angle is a measure for a homogenized aortic wall, while variable circumferential residual strains throughout the radial, circumferential and axial direction have been observed [99, 104, 105, 109, 110]. Moreover, this method does not account for the difference in contribution of the wall constituents to the overall residual stress and axial load [98, 111–113].

In the framework of modeling, multiple approaches have been suggested to estimate the *in vivo* stress in arteries, for example by closing the initially cut *ex vivo* geometry [114–117] or by determining the load-free geometry, based on knowledge of the geometry in the *in vivo* configuration, using inverse methods [118–124]. The number of proposed algorithms that account for the residual stresses and its variation throughout the thickness as well as the constituent-specific properties are much more limited.

Cardamone et al. presented an analytical pre-stretch algorithm based on the constrained mixture theory (section 3.4) and accounted for the differences between the pre-stretch of elastin, collagen fibers and smooth muscle cells [125]. Multiple radial distribution patterns were considered for the circumferential elastin pre-stretch.

A similar algorithm, referred to as the deposition stretch algorithm, was proposed by Famaey et al. [126]. The algorithm was, however, implemented in a finite element analysis and is, thus, applicable to non-idealized geometries. The algorithm is schematically illustrated in figure 3.3. In brief, the algorithm considers the *in vivo* situation as the reference configuration and defines a deformation gradient tensor \mathbf{G}^i , referred to as the deposition stretch tensor of constituent i , that captures the deformation between the unknown stress-free configuration and the *in vivo* reference configuration of that constituent. Note that the deposition stretch tensor accounts for the presence of the *in vivo* load, axial stretch and residual stresses. The collagen deposition stretch tensor \mathbf{G}^c is determined by assuming a constant stretch g^c for collagen in the fiber direction. The algorithm comes, in general, down to calculating the elastin deposition stretch tensor \mathbf{G}^e for each point of the aortic wall. This calculation is initialized by assuming that the *in vivo* geometry is stress-free ($\mathbf{G}^e = \mathbf{I}$) and by pressurizing it to the *in vivo* pressure, e.g. a diastolic pressure of 80 mmHg, which results in a deformation \mathbf{F}_1 . As no deformation is expected in the *in vivo* situation, this virtual deformation is attributed to the absence of deposition stretches in the model, which results in $\mathbf{G}^e = \mathbf{F}_1$ after the first iteration. The procedure is repeated for the updated

deposition stretch tensor \mathbf{G}^e . The remaining deformation after pressurizing the geometry \mathbf{F}_2 is again attributed to the absence of proper deposition stretches, leading to $\mathbf{G}^e = \mathbf{F}_2\mathbf{F}_1$. This procedure is repeated until the remaining deformation \mathbf{F}_n is negligible. The resulting elastin deposition stretch tensor is then determined by $\mathbf{G}^e = \mathbf{F}_n \dots \mathbf{F}_2\mathbf{F}_1$. Under the assumption of incompressibility and a known constant axial elastin deposition stretch g_{ax}^e , the radial component is computed as

$$g_{rad}^e = \frac{1}{g_{circ}^e g_{ax}^e}, \quad (3.13)$$

if the circumferential component g_{circ}^e is known. The algorithm, thus, simplifies to finding the value of g_{circ}^e . Vander Linden et al., further, adjusted this algorithm by predefining the radial distribution pattern of g_{circ}^e [127].

In this dissertation, the simplified deposition stretch algorithm of Famaey et al. is applied to an incompressible thick-walled cylinder without predefined radial distribution of g_{circ}^e [126]. Because of the idealized geometries, a Matlab implementation, instead of the proposed finite element analysis, is adopted.

Note that the inclusion of a different deposition stretch tensor for collagen and elastin implies that the total deformation, which is a combination of the deposition stretch tensor and the tissue deformation, differs for both constituents. Accordingly, constituent-specific Cauchy-Green tensors and invariants are obtained.

3.4 GROWTH AND REMODELING

The concept of a preferred homeostatic stress or stretch state has been well accepted in arterial biomechanics [128]. Indeed, in case of changing loading conditions, e.g. due to hypertension, or external triggers, e.g. due to the placement of a stent-graft, the tissue adapts with the aim to regain its homeostatic stress or stretch state. Therefore, the mechanical behavior of the aortic wall is a dynamic, though slow, process. The aortic tissue can grow, i.e. change in mass, and/or remodel, i.e. change in microstructure, over time. How the tissue evolves over time depends on the considered constituent. Indeed, it was found that elastin has a half-life of ca. 40 years [129, 130]. Moreover, it is deposited during human development and, thus, evolves during human growth, while no new structured or cross-linked elastin is deposited [111, 112]. Conversely, collagen is frequently renewed as its half-life is in the order of 70 days [131]. The capability

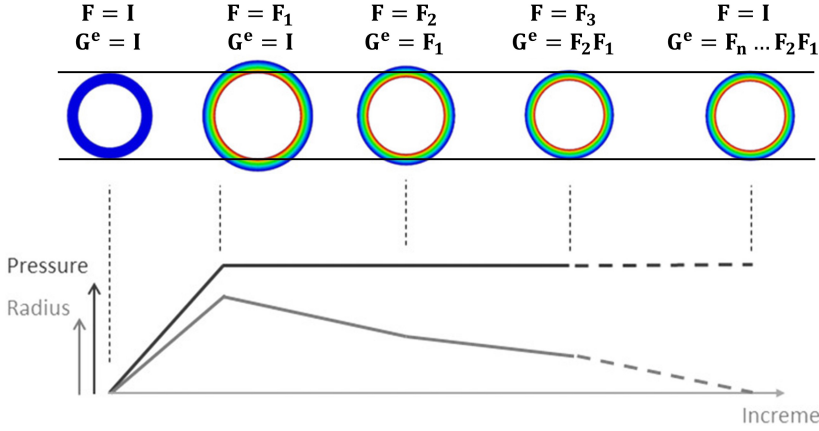


Figure 3.3: Schematic overview of the deposition stretch algorithm, based on the cross-sectional view of a three-dimensional thick-walled cylinder. The deposition stretch tensor of elastin \mathbf{G}^e is iteratively determined by attributing the resulting deformation gradient tensor \mathbf{F} , when loading the *in vivo* aortic geometry to the *in vivo* pressure, to \mathbf{G}^e , as the *in vivo* aortic wall geometry should be retained under *in vivo* pressure. This figure was adapted from Famaey et al. [126].

of the aortic wall to adapt is visible in aortic dissections as well. Indeed, untreated dissections often lead to an expansion in diameter and thickening and a reduced motion of the dissected membrane is observed during the transition from an acute to a chronic dissection [44, 92, 132].

Multiple growth and remodeling frameworks have been proposed of which the most common ones are the kinematic growth theory [133], the constrained mixture theory [134] and the homogenized constrained mixture theory [135]. As the explicit inclusion of the constituents is of interest in the framework of aortic dissections, the discussion below is limited to the constrained and homogenized constrained mixture theory. Note that only the most important aspects are discussed. For a detailed overview of the theoretical frameworks the reader is referred to the original papers of Humphrey and Rajagopal and Cyron et al. [134, 135].

3.4.1 Constrained mixture theory

The constrained mixture theory assumes that the soft tissue is a mixture of multiple constituents i that each have an individual mass production rate, mass removal rate and deposition stretch [134]. Thus,

for each constituent, mass fractions are deposited with a particular deposition stretch at different time points and degrade over time according to their corresponding mass removal rate. Consequently, the density of constituent i at time s , $\rho^i(s)$, is expressed as

$$\rho^i(s) = \rho^i(0)Q^i(s) + \int_0^s m^i(\tau)q^i(s, \tau)d\tau, \quad (3.14)$$

where m^i represents the constituent production rate. The part of the mass fractions, deposited at time 0 and τ , that survives at time s is, respectively, indicated as $Q^i(s)$ and $q^i(s, \tau)$ for constituent i (with $0 < \tau < s$).

As the soft tissue is considered as a mixture of the different constituents, the total strain energy density function Ψ^{tot} , expressed per unit reference volume, is defined as a combination of the constituent-specific strain energy density functions Ψ^i , expressed per unit reference volume of constituent i , weighted by the mass density of the corresponding mass fraction, and is determined as

$$\Psi^{tot}(s) = \sum_i \hat{\Psi}^i(\mathbf{F}_{elas}^i(s, \tau)) \text{ with} \quad (3.15)$$

$$\begin{aligned} \hat{\Psi}^i(\mathbf{F}_{elas}^i(s, \tau)) = & \rho^i(0)Q^i(s)\Psi^i(\mathbf{F}_{elas}^i(s, 0)) \\ & + \int_0^s m^i(\tau)q^i(s, \tau)\Psi^i(\mathbf{F}_{elas}^i(s, \tau))d\tau. \end{aligned} \quad (3.16)$$

The strain energy density, thus, depends on the elastic deformation gradient \mathbf{F}_{elas}^i of the considered constituents. Indeed, the constituents, and their corresponding mass fractions, are constrained to move together with the soft tissue. This implies that each mass fraction of a constituent i , deposited at time τ , has a different reference configuration and, consequently, a different elastic deformation gradient $\mathbf{F}_{elas}^i(s, \tau)$ at time s , which is defined as

$$\mathbf{F}_{elas}^i(s, \tau) = \mathbf{F}(s)\mathbf{F}^{-1}(\tau)\mathbf{G}^i(\tau), \quad (3.17)$$

where $\mathbf{F}(s)$ and $\mathbf{F}(\tau)$, respectively, indicate the total deformation at time s and time τ . Both are often obtained using finite element models. \mathbf{G}^i refers to the deposition stretch tensor of constituent i . As indicated, \mathbf{G}^i could depend on the time of deposition, but is often assumed to be time-independent.

Although no growth deformation is explicitly included in this formulation, it can be integrated in equation (3.17) as [136]

$$\mathbf{F}_{elas}^i(s, \tau) = \mathbf{F}(s)\mathbf{F}_g^{-1}(s) \left(\mathbf{F}(\tau)\mathbf{F}_g^{-1}(\tau) \right)^{-1} \mathbf{G}^i(\tau). \quad (3.18)$$

Here, \mathbf{F}_g indicates the growth deformation gradient tensor for which multiple suggestions have been proposed. The most simple case assumes equal isotropic growth for all constituents and was defined as [137]

$$\mathbf{F}_g(s) = \left(\frac{\rho^{tot}(s)}{\rho^{tot}(0)} \right)^{1/3} \mathbf{I}, \quad (3.19)$$

where $\rho^{tot}(s)$ represents the total density of the constituents at time s . Anisotropy in the expression for \mathbf{F}_g was proposed as well, by assuming transversely isotropic growth, according to [137]

$$\mathbf{F}_g(s) = \frac{\rho^{tot}(s)}{\rho^{tot}(0)} \mathbf{a}_g \otimes \mathbf{a}_g + (\mathbf{I} - \mathbf{a}_g \otimes \mathbf{a}_g). \quad (3.20)$$

Here, \mathbf{a}_g is a unit vector that indicates the main direction of the soft tissue growth. Note that this growth was still assumed to equally affect the considered constituents.

3.4.2 Homogenized constrained mixture theory

Similar to the constrained mixture theory, the homogenized constrained mixture theory considers the soft tissue as a mixture of multiple constituents i , which are constrained to move together with the tissue [135]. However, it is no longer assumed that different mass fractions of constituent i are deposited and removed at different time points over the duration of interest, which results in a different current stress level for each mass fraction. Instead, one temporally homogenized fraction with an average stress level is assumed for each constituent, which avoids the need to track the reference configuration of multiple mass fractions per constituent. It has been shown that the final result of this homogenized constrained mixture theory closely matches the result of the constrained mixture theory at a lower computational cost [135].

As only one mass fraction per constituent is defined, the rate of change in density of constituent i at time s , $\dot{\rho}^i(s)$, is determined as

$$\dot{\rho}^i(s) = \dot{\rho}_+^i(s) + \dot{\rho}_-^i(s). \quad (3.21)$$

The rates of constituent production and degradation at time point s are indicated as $\dot{\rho}_+^i(s)$ and $\dot{\rho}_-^i(s)$, respectively.

The total strain energy density function of the constrained mixture Ψ^{tot} is calculated according to

$$\Psi^{tot}(s) = \sum_i \hat{\Psi}^i(\mathbf{F}_{elas}^i(s)) \quad \text{with} \quad (3.22)$$

$$\hat{\Psi}^i(s) = \rho^i(s)\Psi^i(\mathbf{F}_{elas}^i(s)). \quad (3.23)$$

Consequently, Ψ^{tot} is the sum of the constituent-specific strain energy density functions Ψ^i , weighted by the corresponding current density ρ^i . Note that Ψ^i , and thus Ψ^{tot} , is assumed to depend on the elastic part of the deformation, \mathbf{F}_{elas}^i , only, similar to equation (3.16).

The total deformation gradient tensor at time s , $\mathbf{F}(s)$, is in the homogenized constrained mixture theory defined according to

$$\mathbf{F}(s) = \mathbf{F}_{elas}^i(s)\mathbf{F}_r^i(s)\mathbf{F}_g(s). \quad (3.24)$$

\mathbf{F}_r^i and \mathbf{F}_g represent the deformation gradient tensor as a consequence of the respective soft tissue remodeling and growth. As Ψ^{tot} depends on \mathbf{F}_{elas}^i , it is of interest to rewrite equation (3.24) as

$$\mathbf{F}_{elas}^i(s) = \mathbf{F}(s) \left(\mathbf{F}_r^i(s)\mathbf{F}_g(s) \right)^{-1} \quad (3.25)$$

Similar to the constrained mixture theory, \mathbf{F} is often retrieved as the result of a finite element model. To allow the calculation of \mathbf{F}_{elas}^i , expressions for \mathbf{F}_r^i and \mathbf{F}_g have to be defined. For growth tensor \mathbf{F}_g , the same expressions as for the constrained mixture theory (equations (3.19-3.20)) can be applied.

In order to derive an expression for \mathbf{F}_r^i , which represents the temporally homogenized deformation due to the remodeling of constituent i , it is assumed that the change in Cauchy stress due to remodeling, $\dot{\boldsymbol{\sigma}}_r^i$, can be defined in terms of the rate of change of the corresponding \mathbf{F}_{elas}^i , according to

$$\dot{\boldsymbol{\sigma}}_r^i(s) = \left(\frac{\partial \boldsymbol{\sigma}^i(s)}{\partial \mathbf{F}_{elas}^i(s)} : \dot{\mathbf{F}}_{elas}^i(s) \right)_{\mathbf{F}, \mathbf{F}_g = cte}. \quad (3.26)$$

Moreover, by assuming that \mathbf{F} and \mathbf{F}_g are time independent, from equation (3.24) follows that $\mathbf{F}_{elas}^i(s)\mathbf{F}_r^i(s)$ is constant as well and, by applying the chain rule for derivatives, $\dot{\mathbf{F}}_{elas}^i(s)$ can be written as

$$\dot{\mathbf{F}}_{elas}^i(s) = -\mathbf{F}_{elas}^i(s)\dot{\mathbf{F}}_r^i(s) \left(\mathbf{F}_r^i(s) \right)^{-1}. \quad (3.27)$$

Including equation (3.27) in equation (3.26) and defining that $\mathbf{L}_r^i(s) = \dot{\mathbf{F}}_r^i(s) \left(\mathbf{F}_r^i(s) \right)^{-1}$, consequently, results in

$$\dot{\boldsymbol{\sigma}}_r^i(s) = - \left(\frac{\partial \boldsymbol{\sigma}^i(s)}{\partial \mathbf{F}_{elas}^i(s)} \right)_{\mathbf{F}, \mathbf{F}_g = cte} : \mathbf{F}_{elas}^i(s)\mathbf{L}_r^i(s). \quad (3.28)$$

Besides, the change in Cauchy stress over a time fraction ds can be expressed as the difference in Cauchy stress at time $s + ds$ and s , averaged over the respective constituent masses [135]. This results in

$$\dot{\boldsymbol{\sigma}}_r^i(s)ds = \frac{\boldsymbol{\sigma}_{pre}^i(s)\dot{\rho}_+^i(s)ds + \boldsymbol{\sigma}^i(s)\left(\rho^i(s) + \dot{\rho}_-^i(s)ds\right)}{\rho^i(s) + \dot{\rho}^i(s)ds} - \boldsymbol{\sigma}^i(s), \quad (3.29)$$

where $\boldsymbol{\sigma}_{pre}^i$ indicates the pre-stress of the deposited mass fraction of constituent i . By neglecting the higher order term in the denominator, this leads to

$$\dot{\boldsymbol{\sigma}}_r^i(s) = -\frac{\dot{\rho}_+^i(s)}{\rho^i(s)}\left(\boldsymbol{\sigma}^i(s) - \boldsymbol{\sigma}_{pre}^i(s)\right). \quad (3.30)$$

By combining equation (3.28) and (3.30), $\mathbf{F}_r^i(s)$ can be retrieved from

$$\frac{\dot{\rho}_+^i(s)}{\rho^i(s)}\left(\boldsymbol{\sigma}^i(s) - \boldsymbol{\sigma}_{pre}^i(s)\right) = \left(\frac{\partial \boldsymbol{\sigma}^i(s)}{\partial \mathbf{F}_{elas}^i(s)}\right)_{\mathbf{F}, \mathbf{F}_g = cte} : \mathbf{F}_{elas}^i(s) \mathbf{L}_r^i(s). \quad (3.31)$$

3.5 COMPUTATIONAL MODELS OF THE DISSECTED AORTIC WALL

Multiple dissected wall models have been developed. While some focused on the geometrical complexity, others integrated complex material models. An overview of the most important models is given below. These dissection models often use the technique of finite element analysis, where the equation of linear momentum is solved. This implies that the internal stresses of the tissue need to balance the externally applied forces, when assuming a static or quasi-static configuration, as indicated in section 3.1. To implement the theory of nonlinear continuum mechanics in such a computational model, the considered geometry has to be discretized as no infinite number of calculations can be resolved. Therefore, the geometry is divided in discrete parts, called elements, of which each corner is referred to as a node. The combination of all nodes and elements yields the resulting mesh. An extended overview of the finite element method is, however, beyond the scope of this dissertation.

3.5.1 Acute dissected aortic wall models

3.5.1.1 Geometrically advanced models

Patient-inspired and -specific models of the dissected aortic wall have been developed as part of models that considered the interaction

between the dissected wall and the blood or stent-graft [21, 138–142]. An example geometry of such a model is shown in figure 3.4. Despite their geometrical complexity and accuracy, the models are simplified in terms of material behavior. Indeed, the aortic wall is often represented as a single layer with an isotropic linear elastic or hyperelastic material [21, 138–142]. Wang et al. integrated anisotropy in the wall model, but did not consider the presence of pre-stress, while this was shown to strongly affect the stresses and strains predicted by the model [100–102, 124, 143]. In fact, pre-stress is only rarely included in the patient-specific dissected wall models [21, 142].

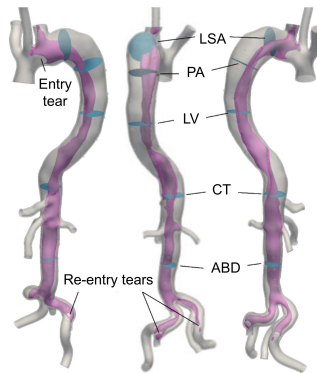


Figure 3.4: Geometry of the patient-specific dissection model considered by Bäumlner et al. [21]. The dissected membrane is indicated in pink, whereas the blue cross-sections indicate the locations of interest, which are situated at the height of the left subclavian artery (LSA), pulmonary arteries (PA), left ventricle (LV), celiac trunc (CT) and bifurcation of the abdominal aorta (ABD). This figure was adapted from Bäumlner et al. [21].

3.5.1.2 Models with advanced material behavior

Buckling of the dissected membrane as well as dissection propagation has been considered in models that integrated the advanced anisotropic hyperelastic material behavior of elastin and collagen in a medial and adventitial layer [65, 71, 72, 144–147]. Indeed, Zhang et al. developed a model of membrane buckling, as a consequence of the release of the residual stresses, in an unloaded cylindrical portion of the aorta after inducing an artificial dissection [144]. Similarly, membrane buckling in a plane-strain model has been considered [145]. The plane-strain model was also applied to model the dissection propagation in the radial direction [145, 146]. Others studied the propagation in a three-dimensional (3D) geometry, but did either not consider the deformed configuration or used it to calibrate model

parameters [65, 71, 72]. Recently, Rolf-Pissarczyk et al. presented a constitutive law that includes the degradation of the elastic fibers that interconnect the medial elastic lamellae, in order to model the dissection propagation [147]. This constitutive law was implemented in an axially stretched and pressurized portion of an idealized dissected aorta wall. The resulting stresses of the deformed model are illustrated in figure 3.5.

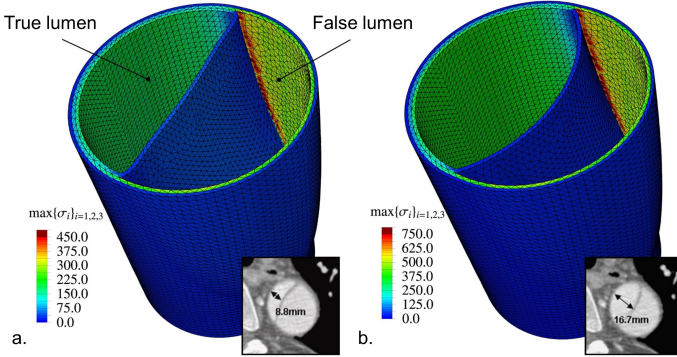


Figure 3.5: Deformation and maximal principal stress, $\max\{\sigma_i\}_{i=1,2,3}$, expressed in terms of Cauchy stress and indicated in kPa, as result of a geometrically idealized model of a dissected aortic wall with a constitutive law that included the degradation of radial elastic fibers, at (a) diastolic and (b) systolic pressure. This figure was adapted from Rolf-Pissaryck et al. [147].

3.5.2 Growth and remodeling in dissected aortic wall models

Multiple theoretical frameworks of arterial growth and remodeling have been developed, as indicated in section 3.4. The main applications of these theories include the Ross procedure, the formation of aortic aneurysms and the effect of hypertension and angioplasty [137, 148–157]. In these applications, the difference in stress between the current and the homeostatic configuration, deviations in wall shear stress and the presence of inflammation have been considered as driving factors.

In the dissected wall, changes in the soft tissue stress, compared to the homeostatic stress state, are hypothesized to be the consequence of the delamination of the dissected membrane and the presence of inflammation (section 2.2.3). Thus, growth and remodeling is expected to take place in a dissected aortic wall, which is confirmed by the

observations of expanded aortic diameters as well as dissected membrane thickening as indicated in sections 2.2.1 and 2.2.2. Gacek et al. investigated the growth and remodeling of an idealized dissected aortic wall, but in the chronic phase only [158]. To date, no further models of the growth and remodeling of the soft tissue in the context of aortic dissections have, to the author's knowledge, been developed.

Uncertainty quantification

As indicated in chapter 3, a lot of progress has been made in the past decades in the development of computational models of aortic dissections. Even though this progress is very valuable, in particular when aiming towards a computationally-supported personalized treatment, *in vivo* data is, up to now, often limited or even unavailable in clinical practice. The *in vivo* wall thickness can currently not be retrieved from clinical computed tomography (CT) or magnetic resonance imaging (MRI) scans, due to the limited spatial resolution. Similarly, the *in vivo* wall behavior often remains unknown, due to missing temporal information in clinical imaging practice. Therefore, many models include assumptions regarding one or more of these unknowns. To assess the impact of such assumptions systematically, the resulting output uncertainty, as a consequence of variations in the input parameter space, can be quantified. The uncertainty quantification, including two techniques for a global sensitivity analysis, and the use of surrogate modeling in sensitivity analyses is discussed in section 4.1 and 4.2, respectively. For uncertainty quantification as well as surrogate modeling, a collection of points that covers the parameter space of interest has to be assessed, which requires proper sampling methods. Therefore, section 4.3 discusses different sampling strategies for the input parameter space. Some applications of uncertainty analysis in the domain of cardiovascular biomechanics are illustrated in section 4.4.

4.1 UNCERTAINTY QUANTIFICATION AND SENSITIVITY ANALYSIS

Uncertainty quantification attempts to determine the impact of uncertain input parameters on the output of interest. In this respect, often the sensitivity of the model output to each of the input parameters is analyzed, which can be performed on a local or global level.

In the case of a local sensitivity analysis, the impact of small parameter variations around a point of interest on the output parameter is considered and corresponds to taking the partial derivative of a function f , which represents the relation between the output $f(\mathbf{x})$ and the n -dimensional input $\mathbf{x} = (x_1, \dots, x_i, \dots, x_n)$, to input parameter x_i as

$$u_i = \frac{\partial f(\mathbf{x})}{\partial x_i}. \quad (4.1)$$

When considering a global sensitivity analysis, the impact of variations over the full input parameter space, and thus multiple input parameters simultaneously, on the output parameter is determined and the contribution of the individual input parameters to the total output uncertainty is assessed. Multiple techniques to perform such an analysis exist and two of the most common ones, the Sobol analysis and the δ moment-independent analysis, are discussed below.

4.1.1 Sobol analysis

The Sobol indices consider the parameter-specific impact on the variance of the output probability distribution as a consequence of the uncertain input parameters [159]. Multiple types of Sobol indices can be determined, depending on the included degree of interaction. Indeed, the first order Sobol indices, S_{1i} , define the individual effect of each input parameter X_i , i.e. the variance of the expected value of output Y if input parameter X_i is known relative to the variance of output Y if all input parameters are unknown. The total order indices S_{T_i} consider all interaction effects related to a specific input parameter, next to the main effect which is also quantified by S_{1i} . The corresponding definitions are given by [159, 160]

$$S_{1i} = \frac{V_{X_i}(E_{X_{\sim i}}(Y|X_i))}{V(Y)} \quad (4.2)$$

$$S_{T_i} = 1 - \frac{V_{X_{\sim i}}(E_{X_i}(Y|X_{\sim i}))}{V(Y)}, \quad (4.3)$$

with $E_{X_{\sim i}}(Y|X_i)$ and $E_{X_i}(Y|X_{\sim i})$ being, respectively, the expected value of output Y when X_i is known and when all input parameters except for X_i are known. The subscripts $X_{\sim i}$ and X_i indicate

that the corresponding expected values are calculated over all input parameters except for X_i and over input parameter X_i , respectively. Similarly, V , $V_{X_{\sim i}}$ and V_{X_i} refer to the variance calculated over all input parameters, all input parameters except for X_i and input parameter X_i .

Although both Sobol indices contain valuable information, specific sampling algorithms have been suggested to facilitate the calculation of these indices at a reasonable computational cost [160]. Moreover, the Sobol analysis requires the input parameters to be independent.

4.1.2 Delta moment-independent analysis

The δ moment-independent analysis describes the difference in output probability distribution for the unconditional case and the conditional case in which input parameter X_i is known, as illustrated in figure 4.1 [161]. The δ indices, therefore, consider the complete output distribution and are, consequently, not limited to a specific moment of the probability distribution, such as e.g. the variance or skewness. Moreover, the definition does not require independence of the input parameters. The δ index of X_i , δ_i , is defined as

$$\delta_i = \frac{1}{2} E_{X_i}[s(X_i)] \text{ with} \quad (4.4)$$

$$s(X_i) = \int \left| f_Y(y) - f_{Y|X_i}(y) \right| dy \text{ and} \quad (4.5)$$

$$E_{X_i}[s(X_i)] = \int f_{X_i}(x_i)[s(X_i)] dx_i. \quad (4.6)$$

Herein, E_{X_i} refers to the expected value of $s(X_i)$, which indicates the shift of input parameter X_i . This shift is determined by the difference between the unconditional probability distribution of output Y , $f_Y(y)$, and the distribution of output Y when input parameter X_i is known, $f_{Y|X_i}(y)$. In this dissertation, the global sensitivity analysis is performed with a δ moment-independent analysis (chapter 7).

4.2 SURROGATE MODELING

To perform a global sensitivity analysis, large numbers of model evaluations need to be performed, with examples indicating numbers in the order of 10^4 [162]. In this context, standard computational modeling techniques, such as the finite element analysis, are often computationally intractable for full-dimensional sensitivity analyses. Therefore, the model simulations can be replaced by a surrogate model that

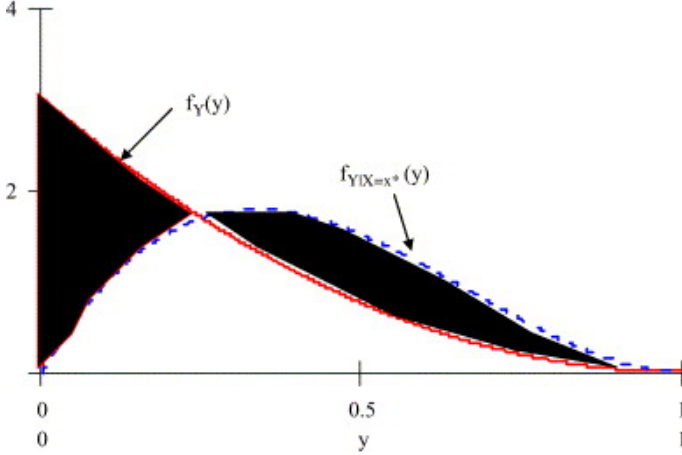


Figure 4.1: Illustration of the interpretation of the δ moment-independent indices. The indices represent the shift in output distribution, which is marked in black, between the unconditional output, $f_Y(y)$, and the conditional output distribution with a known value for input parameter X , $f_{Y|X=x^*}(y)$. This figure was taken from Borgonovo [161].

captures the link between the input and output parameters. Many types of surrogate models exist, with neural networks, polynomial chaos expansion and Gaussian process regression being some of the most well-known ones [163]. In contrast to more deterministic surrogate modeling approaches, e.g. neural networks and polynomial chaos expansion, Gaussian process regression accounts for the intrinsic uncertainty of the model.

Indeed, a Gaussian process describes a set of random variables, of which each finite subset has a joint Gaussian distribution [164]. As the number of random variables in a Gaussian process can be infinite, Gaussian processes are often interpreted as a distribution of functions, where each point of the function corresponds to a random variable. The Gaussian process GP is, then, defined as

$$f(\mathbf{x}) \sim GP(m_{GP}(\mathbf{x}), K_{GP}(\mathbf{x}, \mathbf{x}')), \quad (4.7)$$

where $m_{GP}(\mathbf{x})$ and $K_{GP}(\mathbf{x}, \mathbf{x}')$ indicate, respectively, the mean function and covariance function or kernel.

Multiple kernel functions can be imposed to train the Gaussian process [164]. One of the commonly applied kernel functions is the radial basis function, which is described as

$$K_{GP}(\mathbf{x}, \mathbf{x}') = \sigma^2 e^{-\frac{1}{2} \frac{\|\mathbf{x} - \mathbf{x}'\|^2}{L^2}}, \quad (4.8)$$

where \mathbf{x} and \mathbf{x}' are two points in a multi-dimensional input parameter space. The hyperparameters σ and L , respectively, represent the variance and the length scale of the kernel. In case an anisotropic kernel is applied, each input parameter has its own corresponding length scale. During the training process, the hyperparameters are optimized for a set of training samples. The performance of the trained model is afterwards tested with respect to a set of test samples.

At locations where the training set provides little information, the output prediction, given by the trained Gaussian process, is often uncertain, which means that locally the output variance is large, as illustrated in figure 4.2. Therefore, if the resulting Gaussian process is applied to determine the solution at a point outside of the training set, e.g. $x = 4$ in this example, the solution is sampled from the local distribution provided by the trained Gaussian process at that particular point and is thus not necessarily equal to the corresponding value of the mean function.

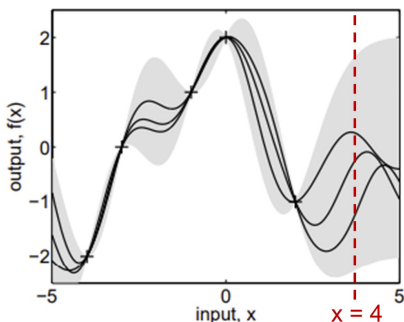


Figure 4.2: Illustration of the result after Gaussian process regression, with some example functions, indicated in black, and the remaining variance, marked in gray. The larger the distance with respect to a data point (+), the larger the remaining variance, as illustrated with $x = 4$. This figure is adapted from Rasmussen and Williams [164].

4.3 SAMPLING STRATEGIES

In both uncertainty quantification and surrogate modeling, a set of points needs to be selected that optimally covers the considered input parameter space. Many strategies to do so have been proposed. Rather than giving an exhaustive overview, some of the most common techniques are summarized below.

4.3.1 Full factorial design

A full factorial design refers to a sampling where all combinations of the input parameters of interest are considered (figure 4.3(a)). This requires the discretization of the individual input parameter ranges into a finite number of values, in order to achieve a finite number of combinations. As all parameter combinations are considered, the number of samples is often high for multi-dimensional problems. However, it allows the determination of all individual and interaction effects of the input parameters on the considered output.

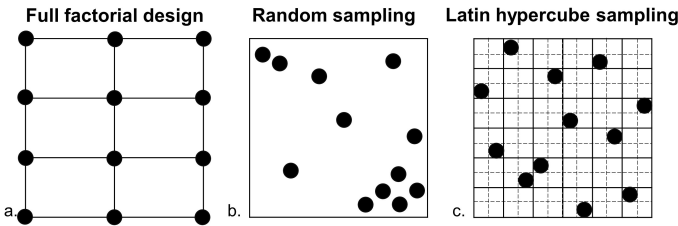


Figure 4.3: Illustration of (a) full factorial design, (b) random sampling and (c) Latin hypercube sampling, each with 12 samples, for two input parameters.

4.3.2 Random sampling

In a random sampling, the samples are generated by randomly choosing input parameter combinations from given continuous intervals, while accounting for their probability density distribution [165]. As the parameter combinations are randomly generated, spreading of the samples over the input parameter space is not guaranteed (figure 4.3(b)). Consequently, many samples might be required to reasonably cover the considered input parameter space.

4.3.3 Latin hypercube sampling

In a Latin hypercube sampling with n samples, the continuous input ranges are each separated in n intervals of equal probability and combined in such a way that each of the n intervals is represented by only one sample for a particular input parameter (figure 4.3(c)) [166]. Within each interval, a random sampling is applied. This technique ensures that the samples are well spread over the input parameter space. This spreading often leads to a reduction in the number of required samples and, thus, enhances the efficiency compared to a random sampling [165].

4.3.4 Saltelli sampling

The Saltelli sampling procedure, indicating an extension of the Sobol sampling, provides a systematic and reproducible technique to sample the continuous ranges of the input parameters, while ensuring a good spread over the parameter space [160]. This sampling technique is, in particular, appropriate to allow the calculation of the total Sobol indices (section 4.1.1), next to the first order Sobol indices, in an efficient manner.

4.4 UNCERTAINTY ANALYSIS IN CARDIOVASCULAR BIOMECHANICS

To the author's knowledge, no formal global sensitivity analysis has been applied to the aortic wall in the framework of dissections. Nevertheless, some aspects of uncertainty in aortic dissection models have been quantified and some examples of formal global sensitivity analyses in cardiovascular mechanics have been performed before. Rather than emphasizing the results of these studies, a brief summary of the considered topics is provided.

The impact of uncertainty in, for example, heart rate, tear size and geometry on the hemodynamics in aortic dissections has been considered [167–169] as well as the effect of uncertain stent-graft parameters on the dissected wall [141, 142]. Regarding the sensitivity of the resulting dissected aortic wall stress and deformation to its unknown parameters, some studies have been performed. In this respect, mainly the imposed tear size was the subject of interest [71, 72, 140, 144–146]. Baumler et al. and Brunet et al. included the impact of the unknown material behavior on, respectively, the dissected membrane movement during the cardiac cycle and the dissection propagation [21, 71]. While most of these studies varied individual parameters and, thus, considered the local uncertainty, Brunet et al. investigated the impact of multiple simultaneous parameter variations, consequently investigating the global uncertainty and determined the most influential factors for dissection propagation [71].

In other cardiovascular applications, two recent examples of a Sobol analysis have been published. Brandstaeter et al. studied the uncertainty in the growth and remodeling of a hypertensive aorta and an idealized abdominal aortic aneurysm, while Campos et al. considered the impact of uncertain material parameters on the passive mechanical behavior of the heart [150, 170].

Problem statement

5.1 PROBLEM STATEMENT

While the exact mechanisms of the initiation and progression of aortic dissection are not yet fully elucidated and the treatment of patients with type B aortic dissections is currently only suboptimal, computational biomechanical models of the dissected aortic wall might increase the insight into the *in vivo* state. Being able to predict the patient outcome *a priori* has the potential to optimize the patient-specific treatment strategy, in particular for patients not requiring an emergency treatment. However, existing dissected aortic wall models of the acute situation include strong assumptions regarding the wall thickness and/or its behavior as no such patient-specific non-invasive information can be retrieved from clinical imaging techniques. The evolution of the dissected aortic wall and, in particular the dissected membrane, over time was represented by one model, which considered the chronic state only.

The uncertainty on the predicted wall stress and deformation introduced by the lack of clinical data on the wall thickness and behavior, both on the short- and long-term, is yet to be quantified in the framework of type B aortic dissections, which is the overall goal of this dissertation.

5.2 OBJECTIVES

This general goal was subdivided into three objectives, each corresponding to a different type of uncertainty.

Objective 1

To investigate the potential of clinical pulse wave velocity measurements to reduce the extent of the material parameter space, and, hence, the uncertainty in global material behavior of the aortic wall, introduced by unknown material parameters.

In this respect, chapter 6 discusses the impact of uncertainty in the determination of material parameters, required for computational biomechanical modeling, based on non-invasive clinical pulse wave velocity measurements for an idealized healthy descending thoracic aortic wall.

Objective 2

To quantify the effect of clinically uncertain material and geometrical parameters on the predicted stress and deformation of a dissected aortic wall model.

Chapter 7 considers how the uncertain wall thickness and stiffness affects the predicted acute wall stress and deformation in an idealized wall model of a type B aortic dissection.

Objective 3

To assess the feasibility to reproduce the clinically observed growth and remodeling of the dissected aortic wall, and the dissected membrane in particular, during its transition from the acute to chronic phase, based on the limited quantitative knowledge on growth and remodeling parameters.

In chapter 8, a slice model of an idealized dissected wall, as part of a type B aortic dissection, was utilized to determine whether the state-of-the-art knowledge regarding growth and remodeling, with all its uncertainty, allows the reproduction of the dissected membrane thickening and total diameter expansion rate, observed during the transition from an acute to chronic dissection.

II

Uncertainty in biomechanical dissected aortic wall models

CHAPTERS

- | | | |
|----------|--|------------|
| 6 | Pulse wave velocity as measure to aid material parameter estimation | 43 |
| 7 | Uncertainty quantification in an idealized dissected aortic wall | 67 |
| 8 | Growth and remodeling of the dissected membrane in an idealized dissected aorta | 101 |

Pulse wave velocity as measure to aid material parameter estimation

One of the major challenges in computational arterial biomechanics is to properly represent the patient-specific material behavior. In the framework of aortic dissections, the standard clinical imaging techniques do not provide sufficient information to retrieve proper material parameters non-invasively. Therefore, this chapter presents an innovative approach and assesses whether a non-invasive stiffness metric, i.e. pulse wave velocity, has the potential to constrain the material parameter space and the corresponding global behavior of biomechanical aortic wall models.

This chapter is based on the paper "*Pulse wave velocity: A clinical measure to aid material parameter estimation in computational arterial biomechanics*", published in Journal of Biomechanics [171].

6.1 INTRODUCTION

Computational arterial biomechanical models often rely on an extensive material parameter set to describe the constitutive behavior of the arterial wall using, e.g. a Gasser-Ogden-Holzapfel (GOH) formulation [15]. These parameters are typically derived from *in vitro* experiments on tissue samples, fitting the model to mechanical test

data [172]. However, when developing patient-specific models from clinical data, it is not trivial to choose parameters that lead to the desired mechanical behavior of the arterial wall over the *in vivo* pressure range because of the difficulty to reconcile *in vivo* measurable arterial mechanical data and an extensive parameter set, needed to develop realistic computational biomechanical models. Multiple attempts have been made to link non-invasive *in vivo* pressure-area data (of e.g. the carotid artery) to constitutive material parameters to facilitate patient-specific modeling, yielding a single, best-fit parameter set [173–176]. However, this technique cannot be extended to central arteries and material parameters obtained using *in vivo* data can still differ from those based on *in vitro* experiments, which suggests that the uncertainty on the fitted material parameters remains large [177, 178].

In clinical practice, arterial stiffness is often quantified using pulse wave velocity (PWV), i.e. the speed at which the arterial pulse propagates along an artery [179]. PWV functionally links the intra-arterial pressure (P) to the lumen cross-sectional area (A) of an arterial segment through the Bramwell-Hill relation, i.e.

$$\text{PWV} = \sqrt{\frac{A}{\rho} \frac{dP}{dA}} = \sqrt{\frac{1}{\rho D_A}} \quad (6.1)$$

with dA the change in lumen cross-sectional area in response to a pressure change dP , D_A the distensibility of the artery and ρ the density of blood. The measure is functional as it captures the *in vivo* area-pressure relation, without requiring knowledge on the material parameters, wall thickness, axial loading or pre-stretch of the considered arterial segment. Moreover, aortic PWV was shown to be a potent biomarker of cardiovascular health [180] and reference values in humans have been published, indicating physiological values of 4–12 m/s [181]. Furthermore, novel ultrasound-based methods allow the assessment of PWV at different pressure levels from tracking the pulse wave generated upon systolic ejection, i.e. at diastolic pressure, and from aortic valve closure, i.e. at dicrotic notch pressure [182, 183].

Despite its clinical value, the added value of PWV in computational arterial wall modeling has, to the authors’ knowledge, not yet been considered. Therefore, this study aims to investigate whether PWV, a clinically measurable parameter reflecting stiffness within the *in vivo* pressure range, is applicable as a guide to reduce the material parameter space in computational arterial biomechanics and to

quantify the remaining uncertainty in material behavior after parameter space reduction.

6.2 METHODS

6.2.1 Arterial reference model

6.2.1.1 Geometry, material and boundary conditions

Although the computational framework, developed in Matlab (The MathWorks Inc., USA), is applicable to any (idealized) artery, this study considered the human descending thoracic aorta, represented as a thick-walled cylinder with a physiological diameter and wall thickness of 27.30 mm and 1.90 mm, respectively [7, 8, 184]. The aortic wall contains a medial and adventitial layer, with a respective wall thickness fraction of 75% and 25%, both behaving as an anisotropic hyperelastic GOH material [6]. For each layer, the strain energy density function Ψ_{layer} is written as

$$\Psi_{layer} = c_{10} (I_1^e - 3) + \frac{k_1}{2k_2} \left(\sum_{j=4,6} e^{k_2 (\kappa I_1^c + (1-3\kappa) I_j^c - 1)^2} - 1 \right), \quad (6.2)$$

with c_{10} the elastin shear modulus, k_1 the collagen fiber stiffness, k_2 the intrinsic collagen fiber stiffening, κ the collagen fiber dispersion, I_1^i and I_j^i respectively the first and j^{th} (with $j = 4, 6$) invariant of the right Cauchy-Green tensor $\mathbf{C}^i = \mathbf{F}^{iT} \mathbf{F}^i$ of constituent deformation gradient tensor \mathbf{F}^i [15]. Invariant I_j^c depends on the mean fiber angle, indicated as α . The superscripts e and c refer to elastin and collagen, respectively.

The formulation for a thick-walled cylinder, i.e.

$$P = \int_{r_i}^{r_o} \lambda_{circ} \frac{\partial \Psi}{\partial \lambda_{circ}} \frac{dr}{r}, \quad (6.3)$$

allowed the iterative calculation of the circumferential stretch λ_{circ} , and the radial displacement, for a known inner radius r_i , outer radius r_o , strain energy density function Ψ and intra-arterial pressure P [185]. Using this formulation combined with the GOH model, the *in vivo* pre-stretched configuration was determined at diastolic pressure (80 mmHg) by calculating the deposition stretches according to the pre-stretching algorithm of Famaey et al. with a default collagen and axial elastin pre-stretch of 1.10 [103, 126]. Starting from this pre-stretched configuration, the aortic deformation at any other intra-arterial pressure level was determined using equation (6.3).

6.2.1.2 GOH parameter selection

For each GOH parameter, a physiological range was determined from reported uniaxial and biaxial experimental and histological data of human (descending) thoracic aortas (table 6.1) [7, 8, 186]. Adventitial parameters c_{10A} and k_{1A} were assumed to depend on their medial counterpart, by considering the relative elastin and collagen area fractions between both layers, reported for the human ascending aorta [12]. Besides, the collagen fibers in both layers were assumed to have the same k_2 value. Combining this with equation (6.2) results in

$$\Psi_M = c_{10M} (I_1^e - 3) + \frac{k_{1M}}{2k_2} \left(\sum_{j=4,6} e^{k_2(\kappa I_1^c + (1-3\kappa)I_j^c - 1)^2} - 1 \right) \quad (6.4)$$

$$\Psi_A = 0.34c_{10M} (I_1^e - 3) + \frac{1.17k_{1M}}{2k_2} \left(\sum_{j=4,6} e^{k_2(\kappa I_1^c + (1-3\kappa)I_j^c - 1)^2} - 1 \right), \quad (6.5)$$

as strain energy density function where index M refers to the medial and index A to the adventitial layer. The seven independent parameter ranges were discretized into five equally spaced values, except for k_1 and k_2 where a logarithmic scale was applied to represent all orders of magnitude. A full factorial design was performed and only parameter sets resulting in a tensile circumferential elastin deposition stretch, g_{circ}^e , throughout the wall were retained, as elastin is hypothesized to be deposited during development and has, therefore, been stretched during human growth [111, 112].

Table 6.1: Input ranges of the GOH parameters for the media and adventitia for the full factorial design in order to obtain potentially physiological parameter sets, based on the data of Jadidi et al., Schriefel et al. and Weisbecker et al. [7, 8, 186]. Each range was discretized into five values, using a linear scale for c_{10} , α and κ and a logarithmic scale for k_1 and k_2 . LB and UB, respectively, indicate the lower and upper bound of the range.

Media			Adventitia			Scale
Parameter	LB	UB	Parameter	LB	UB	
c_{10M} (MPa)	0.005	0.025	c_{10A} (MPa)	$0.34c_{10M}$		Linear
k_{1M} (MPa)	0.0002	1.000	k_{1A} (MPa)	$1.17k_{1M}$		Logarithmic
k_{2M} (-)	4.0	35.0	k_{2A} (-)	k_{2M}		Logarithmic
α_M (°)	0.0	45.0	α_A (°)	45.0	90.0	Linear
κ_M (-)	0	1/3	κ_A (-)	0	1/3	Linear

6.2.1.3 Metric for arterial stiffness

For each GOH parameter set, the PWV was assessed at diastolic (PWV_{80}) and dicrotic notch (110 mmHg; PWV_{110}) pressure, measurable in clinical practice, using the Bramwell-Hill equation (6.1) with a blood density of 1060 kg/m^3 and a forward finite pressure difference of 1 mmHg [182, 187]. To facilitate the parameter space reduction analysis as function of PWV_{80} , the physiological PWV_{80} range was discretized in intervals of 1.00 m/s, centered around a target value. $PWV_{80,t}$, therefore, refers to a PWV_{80} value within the interval centered around the target (e.g. a $PWV_{80,t}$ of 6 m/s indicates a PWV_{80} within 5.50-6.50 m/s). For the parameter sets leading to a $PWV_{80,t}$ within the physiological range (4-12 m/s), the added value of PWV_{110} was considered. Analogous to $PWV_{80,t}$, the resulting PWV_{110} range was discretized into intervals of 1.00 m/s and $PWV_{110,t}$ was defined. To quantify the additional reduction from knowledge of $PWV_{110,t}$ for a given $PWV_{80,t}$, the weighted average over the $PWV_{110,t}$ intervals was computed, using the number of parameter sets per interval as weighting factor.

6.2.2 Reduction in GOH parameter space

6.2.2.1 Global reduction

The extent to which knowledge of $PWV_{80,t}$ provides a global seven-dimensional (7D) parameter space reduction, R_{7D} , was quantified as

$$R_{7D} = 1 - \frac{c_{7D|80t}}{c_{7D}}, \quad (6.6)$$

with c_{7D} the number of parameter sets with $g_{circ}^e \geq 1.00$ throughout the wall and $c_{7D|80t}$ the number of those sets yielding a particular $PWV_{80,t}$ (figure 6.1). When additionally considering $PWV_{110,t}$, the total global reduction, $R_{7D,tot}$, averaged over the $PWV_{110,t}$ intervals, was defined as

$$R_{7D,tot} = \frac{1}{c_{7D|80t}} \sum_{110t} c_{7D|80t,110t} \left(1 - \frac{c_{7D|80t,110t}}{c_{7D}} \right), \quad (6.7)$$

with $c_{7D|80t,110t}$ the number of sets corresponding to both the considered $PWV_{80,t}$ and $PWV_{110,t}$ (figure 6.1). $R_{7D,(tot)} = 0.00$ means that $PWV_{80,t}$ (combined with $PWV_{110,t}$) provides no reduction; $R_{7D,(tot)} = 1.00$ indicates that no parameter sets were found yielding that $PWV_{80,t}$ (and $PWV_{110,t}$).

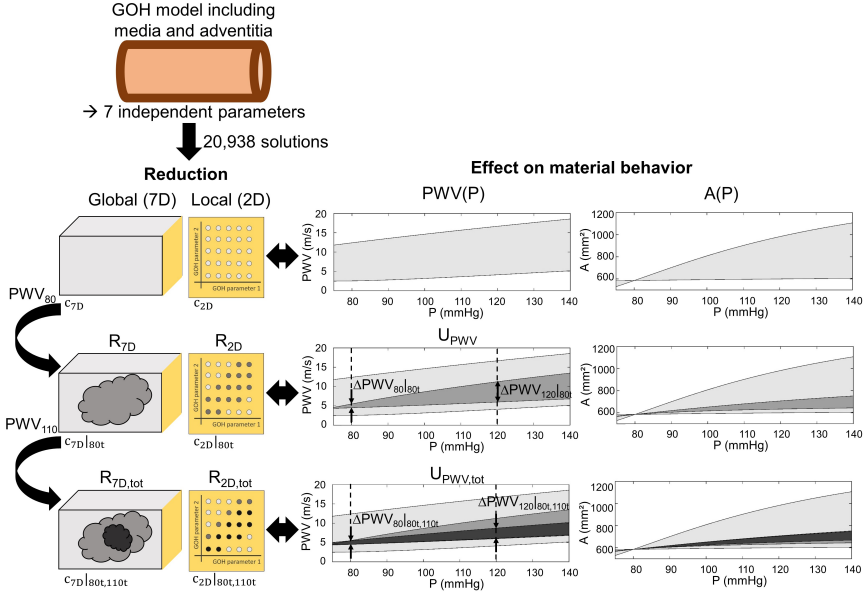


Figure 6.1: Graphical abstract of the study, where the global and local reduction of the GOH parameter space is assessed based on PWV measurements at 80 and 110 mmHg. The effect of the reduction on the global material behavior was considered too, using uncertainty (U) metrics based on the PWV-pressure relations. $\Delta PWV_{120|80t}$ and $\Delta PWV_{120|80t,110t}$ represent the maximal PWV range at 120 mmHg for the selection of parameter sets fulfilling the $PWV_{80,t}$ requirement and for the selection of sets fulfilling the $PWV_{80,t}$ and $PWV_{110,t}$ requirements, respectively. Similarly, $\Delta PWV_{80|80t}$ and $\Delta PWV_{80|80t,110t}$ refer to the maximal PWV range at 80 mmHg, in case only $PWV_{80,t}$ and both $PWV_{80,t}$ and $PWV_{110,t}$ are known.

6.2.2.2 Local reduction

The local two-dimensional (2D) subspace reduction, R_{2D} , quantifies the reduction in number of parameter value combinations per $PWV_{80,t}$ and subspace (i.e. the projection of the 7D parameter set on a plane defined by two GOH parameters) and, consequently, the link between the parameter values and PWV measurements. It was defined as

$$R_{2D} = 1 - \frac{c_{2D|80t}}{c_{2D}}, \quad (6.8)$$

with c_{2D} the maximal number of parameter value combinations (i.e. 25 as each 2D subspace considers two GOH parameters with five levels) and $c_{2D|80t}$ the number of combinations at $PWV_{80,t}$ (figure 6.1). Similar to section 6.2.2.1, i.e. by including $PWV_{110,t}$ and taking

a weighted average, the total local reduction, $R_{2D,tot}$, was calculated as

$$R_{2D,tot} = \frac{1}{c_{7D|80t} \sum_{110t}} c_{7D|80t,110t} \left(1 - \frac{c_{2D|80t,110t}}{c_{2D}} \right), \quad (6.9)$$

with $c_{2D|80t,110t}$ the number of parameter sets for a specific $PWV_{80,t}$ and $PWV_{110,t}$ (figure 6.1). Again, $R_{2D,(tot)} = 0.00$ means that $PWV_{80,t}$ (and $PWV_{110,t}$) does not reduce the considered subspace; $R_{2D,(tot)} = 1.00$ indicates that no parameter set occurs at $PWV_{80,t}$ (and $PWV_{110,t}$). The location and frequency of occurrence of the parameter value combinations was plotted per 2D subspace in, so-called, combination plots.

6.2.3 Remaining uncertainty in material behavior

Even after the reduction guided by the PWV measurements, some uncertainty in the PWV-pressure behavior, U_{PWV} , remains, which was assessed using the systolic pressure (120 mmHg) as point of interest.

In case only $PWV_{80,t}$ is available, U_{PWV} was quantified as

$$U_{PWV} = \frac{\Delta PWV_{120|80t}}{\Delta PWV_{80|80t}}, \quad (6.10)$$

with $\Delta PWV_{80|80t}$ the corresponding maximal PWV range at 80 mmHg (which will approach the predefined interval), and $\Delta PWV_{120|80t}$ the maximal PWV range at 120 mmHg (figure 6.1).

Adding $PWV_{110,t}$ as prior knowledge led to a total uncertainty, $U_{PWV,tot}$, computed as

$$U_{PWV,tot} = \frac{1}{c_{7D|80t} \sum_{110t}} c_{7D|80t,110t} \frac{\Delta PWV_{120|80t,110t}}{\Delta PWV_{80|80t,110t}}, \quad (6.11)$$

with $\Delta PWV_{80|80t,110t}$ and $\Delta PWV_{120|80t,110t}$ the respective corresponding maximal PWV ranges at 80 mmHg and 120 mmHg (figure 6.1). As before, a weighted averaged over the $PWV_{110,t}$ intervals was taken.

6.2.4 Practical implementation: Patient-inspired thoracic aorta

A patient-inspired thoracic aorta model was developed, using the same diameter and total, medial and adventitial wall thickness as the reference model (section 6.2.1) [188]. A $PWV_{80} = 5.96$ m/s and $PWV_{110} = 8.41$ m/s with an uncertainty of 0.50 m/s was assumed

(corresponding to $PWV_{80} = 5.46\text{-}6.46$ m/s and $PWV_{110} = 7.91\text{-}8.91$ m/s) [189]. The GOH parameter sets yielding these target PWV values on the reference model were identified, and the two sets leading to the minimal and maximal PWV_{110} were selected.

A structured hexahedral mesh was created with pyFormex and a finite element analysis, using Abaqus/Standard (Dassault Systèmes, France), was performed. The deposition stretches were estimated for the reference model (section 6.2.1) and refined using a finite element implementation of the algorithm. Starting from this pre-stretched geometry, PWV_{80} and PWV_{110} were calculated based on the mean radial displacement and the Bramwell-Hill equation (6.1) with a finite forward difference of 1 mmHg and compared to the PWV requirements. The variation in systolic PWV (PWV_{120}) and mean maximal principal Cauchy stress ($mMPS_{120}$) was assessed too. A similar approach was applied to a cylindrical model with the same dimensions for verification purposes (appendix A, section 6.6).

6.3 RESULTS

6.3.1 Reduction in GOH parameter space

From the 78,125 parameter sets in the full factorial design, 20,938 fulfill the convergence criteria of the deposition stretch algorithm and result in $g_{circ}^e \geq 1.00$ throughout the wall. Of these, 12,032 sets lead to a $PWV_{80,t}$ within the physiological range (3.50-12.50 m/s) (supplementary material in the online version of the paper [171]). The number of sets is highest for $PWV_{80,t} = 4$ m/s (3,667 sets) and steadily decreases for values up to 8 m/s to suddenly drop between 8 and 9 m/s (figure 6.2(a)).

Figure 6.2(b) displays PWV_{110} , ranging between 3.50-16.50 m/s, per $PWV_{80,t}$ and shows the widest PWV_{110} range for $PWV_{80,t} \leq 9$ m/s, while less spreading is observed for vessels with a high $PWV_{80,t}$ (appendix B, section 6.7).

6.3.1.1 Global reduction

The global parameter space reduction, R_{7D} , varies from 82.5% ($PWV_{80,t} = 4$ m/s) to 99.4% ($PWV_{80,t} = 10\text{-}12$ m/s), relative to the 20,938 converging sets (figure 6.3(a)). Note that 42.5% of the reduction is obtained from excluding sets that lead to PWV_{80} beyond the physiological range. The remaining part of R_{7D} varies between 40.0% and 56.9% and increases with $PWV_{80,t}$ as less sets are attributed to higher $PWV_{80,t}$ (figure 6.2).

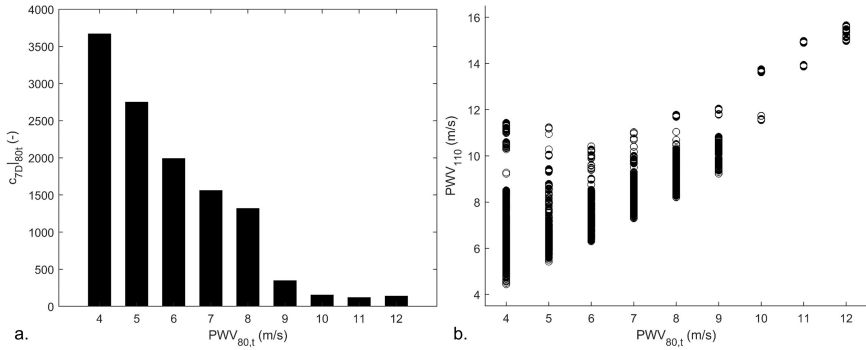


Figure 6.2: (a) Number of GOH parameter sets categorized per $PWV_{80,t}$, i.e. $c_{7D|80,t}$. (b) Overview of PWV_{110} grouped per $PWV_{80,t}$.

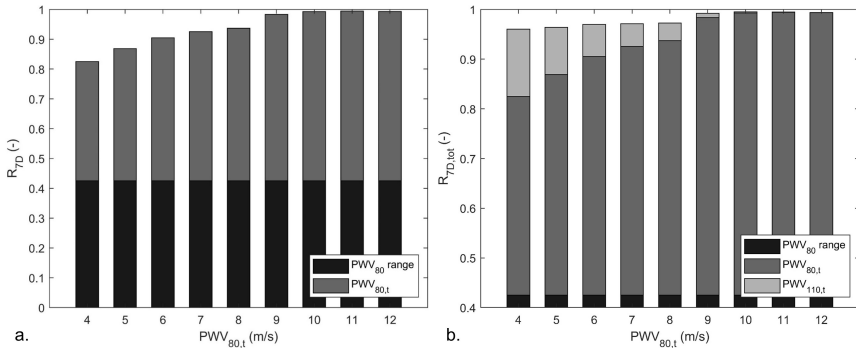


Figure 6.3: (a) Global reduction R_{7D} and (b) total global reduction $R_{7D,tot}$, expressed as function of $PWV_{80,t}$, with respect to the number of converging parameter sets. $R_{7D,tot}$ was calculated by taking the weighted average over the $PWV_{110,t}$ intervals. ‘ PWV_{80} range’ and ‘ $PWV_{80,t}$ ’ indicate the fractions of the reduction related to the exclusion from the physiological PWV_{80} range and not corresponding to the considered $PWV_{80,t}$. ‘ $PWV_{110,t}$ ’ relates to the average fraction of the reduction by knowing the PWV interval at 110 mmHg. All fractions are shown in different shades of gray, as indicated in the legend. Note that the vertical axis of (b) starts from $R_{7D,tot} = 0.40$ and that the fraction below is related to the exclusion from the physiological PWV range.

The 7D reduction further increases to 96.0-99.5% when including $PWV_{110,t}$ (figure 6.3(b)). While the highest $R_{7D,tot}$ are found at 9-12 m/s, the lower values of $PWV_{80,t}$ (4-8 m/s) benefit most from adding $PWV_{110,t}$, with an additional reduction of 3.6-13.6%.

6.3.1.2 Local reduction

The 2D subspace analysis elucidates the contribution of each GOH parameter to the reduction. For 18 of the 21 subspaces, R_{2D} increases for higher $PWV_{80,t}$, i.e. fewer parameter value combinations yield a higher $PWV_{80,t}$ (figure 6.4(a)). Subspaces $c_{10}-\alpha_A$, $c_{10}-\kappa_A$ and $\alpha_A-\kappa_A$ do not contribute to the reduction as $R_{2D} = 0.00$. In contrast, an increasing trend in R_{2D} starting at $PWV_{80,t}$ of 4-6 m/s is observed for the six subspaces including k_1 and for $k_2-\kappa_M$, $\kappa_A-\kappa_M$ and $\alpha_A-\kappa_M$. In other subspaces, the increase in R_{2D} is restricted to $PWV_{80,t}$ from 7-9 m/s on.

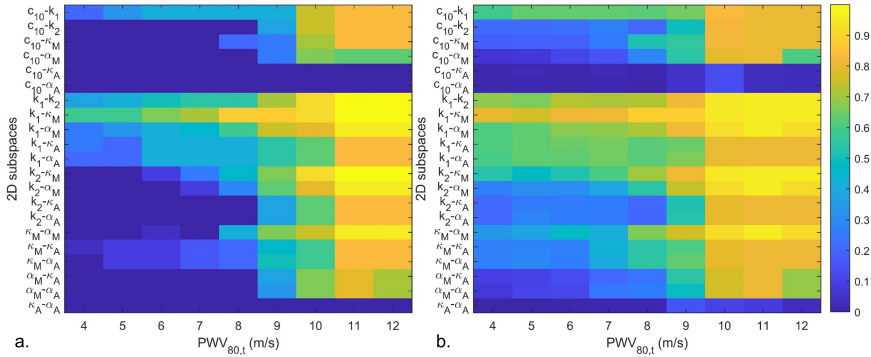


Figure 6.4: (a) Local reduction R_{2D} and (b) total local reduction $R_{2D,tot}$, categorized per 2D subspace of the GOH parameters (vertical axis) and per $PWV_{80,t}$ (horizontal axis). For $R_{2D,tot}$, a weighted average was taken over the $PWV_{110,t}$ intervals. Note that $R_{2D,(tot)}$ equal to 1.00 in itself is not occurring, as this would indicate that no parameter set corresponds to the $PWV_{80,t}$, which is neither the case for (a) nor for (b) as the weighted average over $PWV_{110,t}$ intervals is taken. For example, subspace $k_1-\kappa_M$ leads to a $R_{2D} = 0.60$ at a $PWV_{80,t}$ of 6 m/s, which points out that 15 of the 25 possible parameter value combinations (60.0%) cannot result in a PWV_{80} of 5.50-6.50 m/s. On average, adding $PWV_{110,t}$ information results in $R_{2D,tot} = 0.81$. This means that the number of parameter value combinations is, on average, reduced to 4 for the $k_1-\kappa_M$ subspace at $PWV_{80,t} = 6$ m/s when $PWV_{110,t}$ is known.

The major effect of including $PWV_{110,t}$ is found at 4-7 m/s, while very limited additional reduction occurs for 2D subspaces at 11-12 m/s (figure 6.4(b)). The highest increase in reduction is found for

subspaces composed of k_1 , k_2 , κ_M and α_M , resulting in $R_{2D,tot}$ of 27.2-80.9%, while $R_{2D,tot}$ minimally increases to 0.1-2.0% for subspaces comprised of c_{10} , α_A and κ_A for $PWV_{80,t}$ of 4-7 m/s. The complete overview of $R_{2D,tot}$, per subspace, $PWV_{80,t}$ and $PWV_{110,t}$ is provided in the online version of the paper [171].

Further insight into the relation between $PWV_{80,t}$ and the GOH parameter values is gained from the location and frequency of occurrence, as illustrated for subspaces κ_M-k_1 (high R_{2D}) and α_A-c_{10} ($R_{2D} = 0.00$) (figure 6.5). For κ_M-k_1 , $PWV_{80,t} \leq 10$ m/s can be reached for certain parameter value combinations, with higher values of k_1 requiring higher values of κ_M , while only one combination yields $PWV_{80,t} > 10$ m/s. In contrast, a homogeneous spread is found over the $PWV_{80,t}$ range for subspace α_A-c_{10} , meaning that any $PWV_{80,t}$ is achievable with any parameter value combination of this 2D subspace over the considered range.

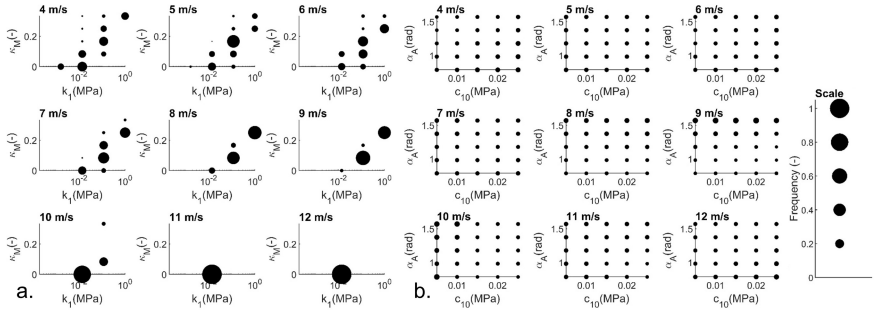


Figure 6.5: The GOH combination plots show the location and frequency of occurrence of the parameter value combinations per $PWV_{80,t}$, for subspaces (a) κ_M-k_1 and (b) α_A-c_{10} . The marker size is scaled proportional to the frequency of occurrence, relative to the total number of parameter sets per $PWV_{80,t}$. For instance, for a $PWV_{80,t}$ of 7 m/s and subspace (a) κ_M-k_1 , it can be seen that the parameter value combination $\kappa_M = 0.083$ and $k_1 = 0.119$ MPa was found in 30.8% of the parameter sets that lead to a PWV_{80} of 6.50-7.50 m/s.

6.3.2 Remaining uncertainty in material behavior

The uncertainty in global behavior, U_{PWV} , decreases monotonously with $PWV_{80,t}$, from 831% at 4 m/s to 72.9% at 12 m/s (figure 6.6). Additional knowledge of PWV_{110} reduced the uncertainty for all but the highest PWV level, with $U_{PWV,tot}$ varying from 25.7% to 137% (figure 6.6).

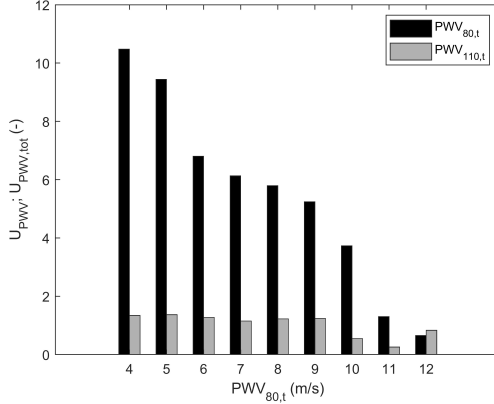


Figure 6.6: The uncertainty and the total uncertainty in PWV-pressure behavior based on knowing $PWV_{80,t}$ (U_{PWV}) and based on knowing $PWV_{80,t}$ and $PWV_{110,t}$ ($U_{PWV,tot}$) are indicated by ‘ $PWV_{80,t}$ ’ and ‘ $PWV_{110,t}$ ’, respectively.

6.3.3 Practical implementation: Patient-inspired thoracic aorta

Out of the 2,045 parameter sets within the $PWV_{80,t}$ range, 424 remain when accounting for the PWV_{110} range, of which those with the minimal and maximal PWV_{110} are selected (figure 6.7(a)). After inclusion of the deposition stretches, the finite element analysis of the patient-inspired aorta leads to deviations of 0.009-0.034 mm from the required diastolic radius (13.650 mm) and results in $PWV_{80} = 6.10$ - 6.72 m/s and $PWV_{110} = 7.27$ - 9.43 m/s (table 6.2). The variation in systolic material behavior for the patient-inspired aorta equals 2.52 m/s ($U_{PWV} = 405\%$) for the PWV_{120} and 0.019 MPa for the $mMPS_{120}$. The diastolic and systolic configurations, together with the maximal principal Cauchy stress at 120 mmHg, are shown in figure 6.7(b, c).

6.4 DISCUSSION

To the authors’ knowledge, this study is the first to address the added value of PWV, a clinical arterial stiffness parameter, for (i) identifying the material parameters of nonlinear hyperelastic constitutive models in arterial computational biomechanical models, and (ii) quantifying the uncertainty of the material behavior. Using the GOH model and a descending thoracic aorta as an example, it was demonstrated that measuring the PWV at a reference pressure (80 mmHg) is a straightforward tool to drastically reduce the parameter space. The addi-

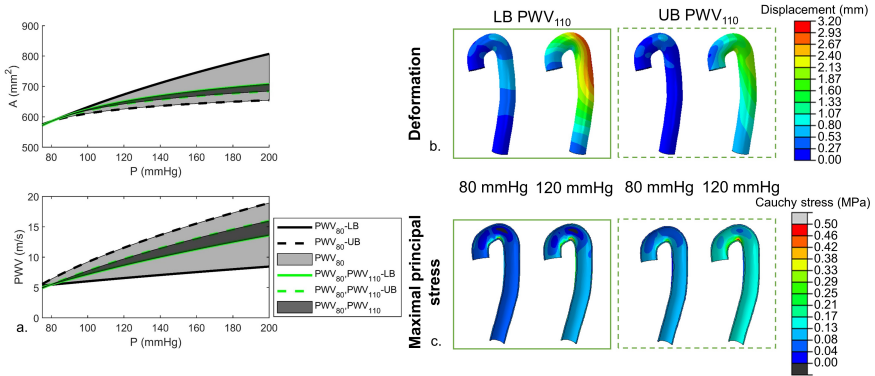


Figure 6.7: (a) Overview of the potential area-pressure and the PWV -pressure relations of the parameter sets resulting in the required PWV_{80} (indicated in light gray) and in the required PWV_{80} and PWV_{110} interval (indicated in dark gray) for the reference model. The curves of the parameter sets that fulfill both requirements and lead to the minimal (lower boundary, LB) and maximal (upper boundary, UB) PWV_{110} are indicated in green, while the curves of the parameter sets that only fulfill the PWV_{80} requirements and lead to the minimal and maximal PWV_{110} are indicated in black. The curves corresponding to the minimal and maximal PWV_{110} are illustrated with a full and dashed line, respectively. The corresponding (b) deformed configurations in diastolic (80 mmHg) and systolic (120 mmHg) pressure and (c) the maximal principal Cauchy stress of the cross-section at 80 mmHg and 120 mmHg are presented for the parameter sets with the minimal PWV_{110} (LB PWV_{110} , full line) and maximal PWV_{110} (UB PWV_{110} , dashed line).

tional knowledge of PWV at a higher pressure (110 mmHg) resulted in further reduction.

6.4.1 Extent of parameter space reduction

Using PWV_{80} is a potent way to reduce the GOH parameter space. Simply excluding GOH parameter sets leading to non-physiological PWV_{80} (beyond 3.50-12.50 m/s) reduced the parameter space with 42.5%. Further considering a PWV_{80} within a 1.00 m/s interval reduced the global parameter space by minimally 82.5%. The highest reduction (for the global and local analyses) was found for $PWV_{80,t} \geq 9$ m/s. Such values are mainly observed in older or diseased subjects [180, 190] and correspond to stiff materials as using the Moens-Korteweg equation for the current model leads to a Young's modulus of 1.52 MPa for a PWV of 10.00 m/s. Younger, healthy subjects exhibit a lower PWV_{80} , which can be obtained with more GOH parameter sets and, consequently, results in a larger variability in PWV

6. PULSE WAVE VELOCITY AS MEASURE TO AID MATERIAL
PARAMETER ESTIMATION

Table 6.2: Overview of the GOH parameter values of the parameter sets with the minimal and maximal PWV_{110} , selected from the 424 sets that fulfilled the requirements of the use case, together with their corresponding PWV measurements for the reference model, the cylindrical aortic verification case (for minimal PWV_{110} only (appendix A, section 6.6)) and the patient-inspired aorta at 80 mmHg and 110 mmHg, i.e. PWV_{80} and PWV_{110} . The diastolic mean radius, R_{80} , and the PWV, mean cross-sectional area and mean maximal principal Cauchy stress (MPS) at 120 mmHg, PWV_{120} , A_{120} and $mMPS_{120}$, were considered too.

	GOH parameters						
	c_{10} (MPa)	k_1 (MPa)	k_2 (-)	κ_M (-)	α_M (°)	κ_A (-)	α_A (°)
Min PWV_{110}	0.010	0.119	35.0	0.250	11.3	0.083	45.0
Max PWV_{110}	0.020	0.139	20.4	0.000	33.8	0.000	45.0
	R_{80} (mm)	PWV_{80} (m/s)	PWV_{110} (m/s)	PWV_{120} (m/s)	A_{120} (mm ²)	$mMPS_{120}$ (MPa)	
Min PWV_{110}							
Reference	13.650	5.49	7.91	8.64	650	/	
Verification	13.653	5.53	8.00	8.68	651	0.140	
Patient-inspired	13.616	6.10	7.27	8.05	655	0.141	
Max PWV_{110}							
Reference	13.650	5.52	8.76	9.71	642	/	
Patient-inspired	13.659	6.72	9.43	10.57	636	0.122	

at higher pressures (figure 6.2). For these subjects, it becomes relevant to include a PWV measurement at a higher (e.g. dirotic notch) pressure, as adding $PWV_{110,t}$ significantly increases the reduction (figure 6.3-6.4). Thus, the PWV measurements at diastolic and dirotic notch pressure provided reduction in the 7D parameter space and, consequently, the 2D subspaces, at higher and lower $PWV_{80,t}$.

While the achieved reduction depends on the $PWV_{80,t}$, fewer parameter sets lead to high $PWV_{80,t}$ (figure 6.2). It should, consequently, be elucidated whether the higher reduction at higher $PWV_{80,t}$ relates to the parameter space and its sampling or whether it reveals that few physiological GOH parameter sets reach these high $PWV_{80,t}$. The parameter space was, therefore, resampled with a linear scale for k_1 and k_2 to include more higher collagen stiffness values compared to the logarithmic scale. While anticipating more sets with a high $PWV_{80,t}$ using the linear scale, no sets corresponding to a $PWV_{80,t}$ of 11-12 m/s were found. Therefore, it is hypothesized that the limited number of parameter sets at high $PWV_{80,t}$ is not

caused by insufficient “stiff” input values, but indicates that few sets lead to high $PWV_{80,t}$.

6.4.2 Relation of local reduction to the GOH parameters

PWV measurements contributed notably to the local reduction for parameters related to the medial collagen fibers, with subspaces consisting of k_1 , k_2 , κ_M or α_M leading to the highest reduction ($R_{2D,tot} \geq 27.2\%$). This aligns with the fact that these parameters represent the (medial) anisotropic nonlinear behavior in the GOH model. Moreover, 75% of the wall consists of medial tissue, which contains more circumferentially directed collagen fibers [16]. It is, consequently, expected that the related parameters strongly affect the radial deformation and correlate to PWV. Remarkably, no parameter set in the physiological PWV_{80} range contained $k_1 = 0.0002$ MPa, which indicates that this order of magnitude rarely occurs in physiological materials [186].

In contrast to the medial collagen parameters, subspaces containing parameters c_{10} , κ_A and α_A hardly provided any subspace reduction ($R_{2D,tot} \leq 14.9\%$) through the use of PWV measurements. For κ_A and α_A , this likely relates to the more axially oriented collagen fibers in the adventitia, while PWV is defined by a radial deformation [16]. Moreover, it was suggested that the adventitia protects the aortic wall against extreme loadings and, thus, mainly affects the wall mechanics at supra-physiological pressures [14], while pressures within the physiological range were considered. The limited reduction for the adventitial fiber-related parameters does, however, not imply that they are irrelevant, but that the PWV measurements are insufficient to draw conclusions on them. The absence of a strong reduction in the parameter space for c_{10} is expected to be related to the deposition stretch algorithm, where a stiffer elastin behavior (higher c_{10}) commonly results in a lower g_{circ}^e , which, partially, compensates the stiffer behavior.

While the 2D reduction relates to the number of parameter value combinations, the combination plots provide insight into their location and frequency of occurrence (figure 6.5), thus delivering 2D regions of interest. However, these regions do not guarantee that each set results in the requested $PWV_{80,t}$ and $PWV_{110,t}$, as the plots limit the interpretation to 2D while considering a 7D parameter space. This is also reflected by the difference between R_{7D} and R_{2D} . An example algorithm to select a parameter set that fulfills the required PWV_{80} and PWV_{110} intervals is provided in appendix C (section 6.8).

6.4.3 Remaining uncertainty with knowledge of PWV

Even within the collection of parameter sets that fulfill the convergence, $PWV_{80,t}$ and $PWV_{110,t}$ requirements, differences in material behavior remain, which were quantified by the uncertainty on the PWV at systolic pressure (U_{PWV}). In line with the reduction analysis, a lower $PWV_{80,t}$ was associated with a higher U_{PWV} , which reduced when including $PWV_{110,t}$. The proposed analysis and approach, thus, yields a collection of parameter sets with a similar global behavior, rather than a single set, as typically obtained with a curve fitting approach [173–178]. While a single set provides a ready-to-use solution and allows the uncertainty estimation of individual parameters, it is an advantage of the proposed approach to naturally reveal and acknowledge the uncertainty in the global material behavior, e.g. introduced by measurement inaccuracies or partial knowledge of the behavior due to limited tested loading conditions, and to estimate its effect, which is important when interpreting the modeled results.

6.4.4 Practical implementation: Patient-inspired thoracic aorta

To demonstrate the use of the framework, the GOH parameter sets matching the predefined intervals of PWV at 80 and 110 mmHg were determined and a finite element analysis for a cylindrical verification case, with the same specifications as the reference model (appendix A, section 6.6), and a patient-inspired thoracic aorta were performed for the parameter sets with the minimal and maximal PWV_{110} . The verification case demonstrates that the results closely match those of the reference model. Applying the methodology to the patient-inspired aorta yielded PWV values close to, though not within, the desired intervals, with a maximal deviation of 0.64 m/s. The difference between the predefined intervals and the achieved PWV values is ascribed to the complex anatomical arch geometry, which differs from the cylinder used to calculate the PWV. The complex geometry also led to a higher uncertainty of PWV at 120 mmHg ($U_{PWV,tot} = 405\%$), compared to the reference model ($U_{PWV,tot} = 154\%$). Despite some deviations in PWV and uncertainty with respect to the reference model, results within the same range were obtained for the patient-inspired aorta, which suggests that the link between the GOH parameters and the PWV of the reference model can provide guidance in the parameter space reduction, even for complex geometries.

The uncertainty in material behavior translates into uncertainty in the modeled output. Indeed, applying the parameter sets, yielding

the lowest and highest PWV_{110} , to the patient-inspired aorta leads to limited differences in $mMPS_{120}$ of 0.019 MPa between both sets (table 6.2).

This particular example illustrates the added value of the current study for arterial computational modeling practice in general, by (i) using readily available clinical data to guide model parameterization and (ii) stepping away from the deterministic view of simulations relying on a single parameter set to represent the *in vivo* situation. Indeed, rather than intending to provide a ground-truth GOH parameter set for the considered arterial model, for which the current clinically available data is too limited, the approach provides a selection of potential sets with a similar global material behavior as measured *in vivo*. The practical application of this information might differ from study to study. Indeed, one could select one (e.g. the set with the highest frequency of occurrence (appendix C, section 6.8)) or multiple (e.g. the two sets that represent the extreme behavior within the selection) parameter sets to apply to the model. The deviation between the unknown ground-truth parameter set and the applied one(s) is accounted for by quantifying the uncertainty, which can be either determined for the specific model, or estimated based on the idealized one.

6.4.5 Limitations

The presented methodology links non-invasive clinical stiffness measurements to the parameters of the constitutive GOH model. It is, however, important to note that the reference model assumes no tethering to external tissues, a homogeneous material in the media and adventitia and a cylindrical geometry with a constant diameter, wall thickness and media and adventitia fraction. This is no longer valid in patient-specific geometries, and might, therefore, affect the deformation and the link between the parameter sets and the measured PWV [106, 191–194]. However, the patient-inspired aorta, where the obtained PWV_{80} and PWV_{110} approached the required behavior quite well, suggests that the PWV measurements can still provide guidance regarding the GOH parameter space when considering complex geometries. Nonetheless, this work is best approached as a modeling concept that was illustrated on an idealized thoracic aorta model of chosen dimensions. When implementing the framework for a specific application with dimensions that significantly differ from the presented case, it is advisable to have a reference model that closely approaches the application.

Moreover, the impact of wall geometry variations was analyzed on a pooled data set that covered the physiological range for the wall thickness and the medial and adventitial thickness fractions (appendix D, section 6.9). The reduction was slightly decreased, but similar trends as for the reference model were observed for both thickness parameters. Therefore, the relation between the GOH parameter sets and PWV measurements was only compromised to a limited extent, which suggests that measuring PWV is a robust manner to guide the parameter selection process, even for an unknown wall geometry.

A fixed axial elastin pre-stretch of 1.10 was applied, whereas this is strongly patient-specific [103]. Therefore, additional calculations were performed for five parameter sets with a $PWV_{80,t}$ of 5 and 10 m/s and axial pre-stretch levels ranging from 1.00 to 1.60. Overall, no differences in PWV-pressure behavior were observed for physiological pressures, which suggests that axial elastin pre-stretch plays a minor role in the current application.

While this study focused on PWV measurements at 80 mmHg and 110 mmHg, corresponding to the current clinical practice, an extension to more PWV-pressure data points, if available, is possible. This is expected to further refine the parameter space.

6.5 CONCLUSION

In conclusion, this study showed the potential of using PWV at diastolic and dicrotic notch pressure to reduce the GOH parameter space, in particular for parameters related to the medial collagen fibers. The results, therefore, demonstrate that PWV measurements present a novel method to provide guidance during arterial computational modeling, while acknowledging the remaining uncertainty in global material behavior.

6.6 APPENDIX A: VERIFICATION CASE

Methods

The presented methodology was verified by considering an ideal cylinder that matches the dimensions of the reference model, i.e. a diameter of 27.30 mm and a wall thickness of 1.90 mm, consisting out of 75% medial and 25% adventitial tissue. Using this geometry with a length of 60.00 mm and a structured hexahedral mesh, a finite element analysis was performed using Abaqus/Standard (Dassault Systèmes, France) to determine the mean radial displacement of the inner wall nodes at 80, 81, 110 and 111 mmHg. The deposition stretches were integrated as described in section 6.2.1. Next, the resulting radial displacements were used to calculate PWV_{80} and PWV_{110} , using the Bramwell-Hill equation (6.1). The material properties corresponding to those with the minimal PWV_{110} of table 6.2 were applied.

Results

After applying the deposition stretches, a radius of 13.653 mm was obtained at 80 mmHg, which is in close correspondence to the required initial inner radius of 13.650 mm. Based on the mean radii obtained at 81, 110, 111, 120 and 121 mmHg, a $PWV_{80} = 5.53$ m/s, $PWV_{110} = 8.00$ m/s and $PWV_{120} = 8.68$ m/s were found. This closely corresponds to the PWV measurements of the reference (Matlab) model ($PWV_{80} = 5.49$ m/s, $PWV_{110} = 7.91$ m/s). The geometry with the corresponding displacement magnitude at 80 mmHg, 110 mmHg and 120 mmHg is represented in figure 6.8. The maximal principal Cauchy stress at 120 mmHg is illustrated in figure 6.9.

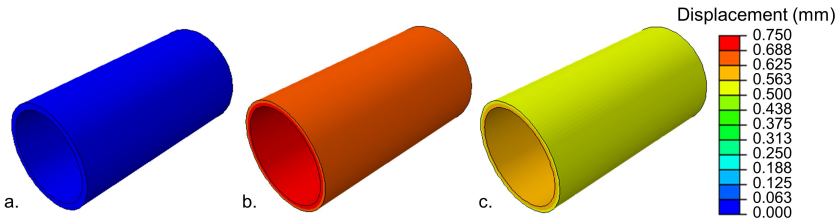


Figure 6.8: Geometry of the cylindrical verification case after application of the pre-stretch at (a) diastolic pressure (80 mmHg), (b) diastolic notch pressure (110 mmHg) and (c) systolic pressure (120 mmHg). A diameter of 27.30 mm, a wall thickness of 1.90 mm and a medial and collagen thickness fraction of 75% and 25% were applied, equal to the dimensions of the reference model.

6. PULSE WAVE VELOCITY AS MEASURE TO AID MATERIAL
PARAMETER ESTIMATION

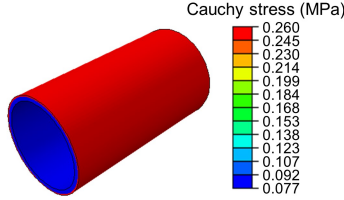


Figure 6.9: Maximal principal Cauchy stress of the cylindrical verification case at systolic pressure (120 mmHg).

6.7 APPENDIX B: OVERVIEW OF NUMBER OF PARAMETER SETS
PER $PWV_{110,t}$ INTERVAL

Table 6.3: Overview of the number of parameter sets, $c_{7D|80t,110t}$, categorized per $PWV_{80,t}$ and $PWV_{110,t}$.

$PWV_{110,t}$	$PWV_{80,t}$ (m/s)								
	4	5	6	7	8	9	10	11	12
4	2	0	0	0	0	0	0	0	0
5	682	1	0	0	0	0	0	0	0
6	1203	1035	36	0	0	0	0	0	0
7	850	832	874	25	0	0	0	0	0
8	561	267	600	895	51	0	0	0	0
9	21	497	194	205	775	19	0	0	0
10	56	90	284	186	371	215	0	0	0
11	292	27	0	248	4	103	0	0	0
12	0	0	0	0	117	8	33	0	0
13	0	0	0	0	0	0	0	0	0
14	0	0	0	0	0	0	120	5	0
15	0	0	0	0	0	0	0	112	133
16	0	0	0	0	0	0	0	0	5

6.8 APPENDIX C: PARAMETER SELECTION ALGORITHM

Parameter selection algorithm

To take the PWV measurements as a guideline for parameter space reduction, rather than as an exact representation of the material behavior, it is the aim not to limit the choice of parameter set to the set with the PWV_{80} and PWV_{110} closest to the requirements. Moreover, it might be sufficient for some applications to consider one parameter set in the required range, rather than applying the upper and lower boundary of the requested range. Therefore, an algorithm was developed to determine a parameter set based on the parameter value combination with the highest frequency of occurrence over the 2D subspaces.

First of all, the algorithm selects the parameter sets that fulfill the PWV_{80} and PWV_{110} requirements (including a predefined uncertainty range), based on the 12,032 sets that are listed in supplementary material, which can be found in the online version of the paper [171]. For this selection of parameter sets, the frequency of occurrence is determined for each parameter value combination and per 2D subspace. The parameter value combination with the highest frequency of occurrence is taken and the corresponding parameter values are assigned to the two GOH parameters. Next, the frequency of occurrence of all parameter value combinations is updated for the GOH parameters that still have to be determined, while ensuring compatibility with the GOH parameters that are already known from all previous iterations. In this respect, the frequency of occurrence of the GOH parameter value combinations that have been selected are assigned as 0, as well as the parameter value combinations which are incompatible with these selected values. In the next iterations, the parameter value combination with the highest frequency of occurrence over all updated 2D subspaces is, again, selected. At the end of each iteration, an update of the frequencies of occurrence of the 2D subspaces is performed. The iterative process finishes when a parameter value for each GOH parameter was found. A schematic representation is illustrated in figure 6.10.

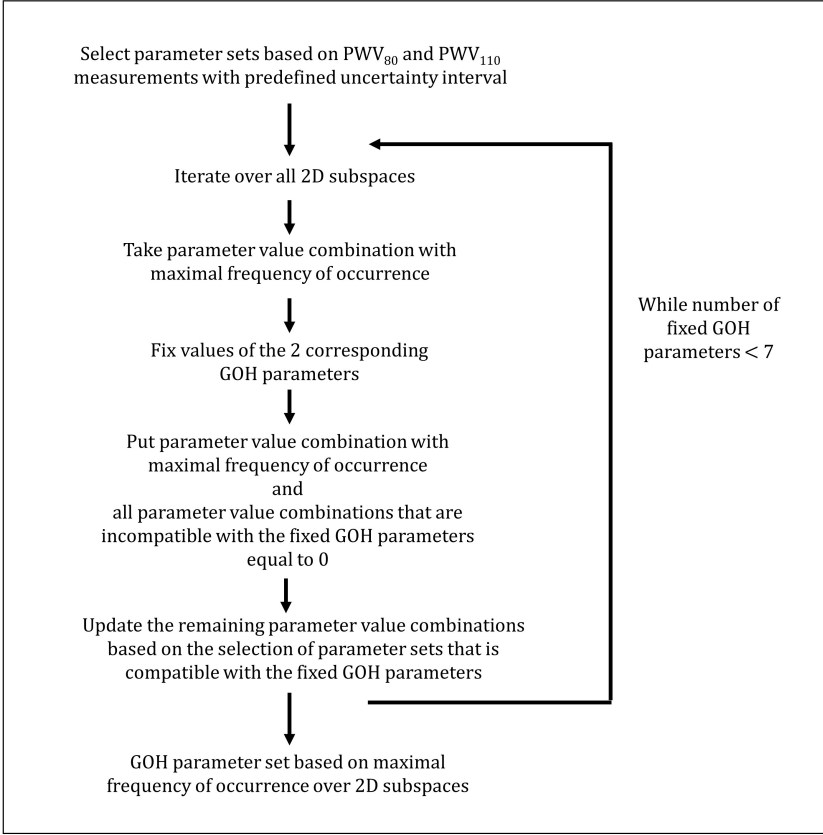


Figure 6.10: Schematic overview of the selection algorithm to determine the parameter set based on the maximal frequency of occurrence over the 2D subspaces.

6.9 APPENDIX D: EFFECT OF VARIATIONS IN WALL GEOMETRY

Methods

Effect of total wall thickness

A fixed wall thickness of 1.90 mm was assumed for the descending thoracic aorta in the main analysis of this study. In practice, the exact wall thickness is, however, often not known as it cannot be retrieved from e.g. clinical computed tomography (CT) scans. In order to elucidate the robustness of the considered approach with respect to the wall thickness, the 2D reduction analysis was repeated for a pooled data set with wall thicknesses covering the physiological range (1.30 mm, 1.90 mm and 2.50 mm) [6–8].

Effect of medial and adventitial thickness fractions

The fractions of medial and adventitial thickness were assumed to be 75% and 25% of the total wall thickness, respectively. These fractions can, unfortunately, not be derived from the standard clinical imaging. Moreover, these fractions have been shown to be highly variable, e.g. due to the presence of hypertension [192]. It is, therefore, important to consider the sensitivity of the presented analysis to changes in the medial and adventitial thickness fractions. Therefore, the 2D reduction analysis was repeated for a pooled data set, analogous to the total wall thickness. The pooled data set contained data for three different fractions of the media and adventitia thickness (65-35%, 75-25% and 85-15%), which are expected to cover the physiological range when being combined [6–8].

Results*Effect of total wall thickness*

Figure 6.11 shows two example 2D subspaces, k_1-c_{10} and α_M-k_1 , where the results of a wall thickness of 1.90 mm are compared to the results based on the pooled data set. The extent of reduction was slightly decreased, compared to the analysis with a wall thickness of 1.90 mm, but similar trends were observed. Moreover, the location and frequency of occurrence was similar for $PWV_{80,t}$ up to 8 m/s. For $PWV_{80,t}$ from 9 m/s on, some differences were observed, in particular for combinations including α_M .

Effect of medial and adventitial thickness fractions

Very similar results were found for the 2D subspace plots of the reference model data and the pooled data, in particular for $PWV_{80,t}$ of 4-8 m/s. From 9-12 m/s, small discrepancies between both data sets occurred that lead to a slight decrease in reduction for the pooled data set, especially for 2D subspaces with α_M . Figure 6.12 illustrates the difference between the media and adventitia fractions of 25% and 75% and the pooled data set for subspaces k_1-c_{10} and α_M-k_1 .

6. PULSE WAVE VELOCITY AS MEASURE TO AID MATERIAL
PARAMETER ESTIMATION

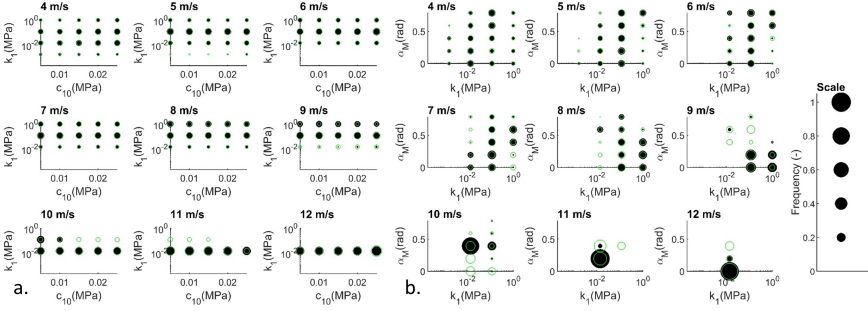


Figure 6.11: The GOH combination plots show the location and frequency of occurrence of the parameter value combinations per $PWV_{80,t}$ for (a) k_1 - c_{10} with a wall thickness of 1.90 mm and the pooled wall thickness data, (b) α_M - k_1 with a wall thickness of 1.90 mm and the pooled wall thickness data. The black markers indicate the result obtained with a wall thickness of 1.90 mm, while the green markers represent the pooled data, i.e. the combined data of wall thicknesses of 1.30 mm, 1.90 mm and 2.50 mm. The marker size is scaled proportional to the relative frequency of occurrence, with respect to the total number of parameter sets per $PWV_{80,t}$.

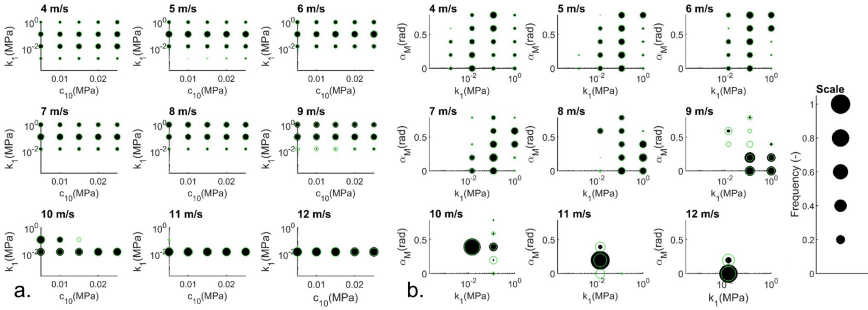


Figure 6.12: The GOH combination plots show the location and frequency of occurrence of the parameter value combinations per $PWV_{80,t}$ for (a) k_1 - c_{10} with medial and adventitial thickness fractions of 75% and 25% and the pooled medial and adventitial thickness fraction data, (b) α_M - k_1 with medial and adventitial thickness fractions of 75% and 25% and the pooled medial and adventitial thickness fraction data. The black markers indicate the result obtained with a medial and adventitial thickness fraction of 75% and 25%, while the green markers represent the pooled data, i.e. the combined data of medial and adventitial thickness fractions of 65-35%, 75-25% and 85-15%. The marker size is scaled proportional to the relative frequency of occurrence, with respect to the total number of parameter sets per $PWV_{80,t}$.

Uncertainty quantification in an idealized dissected aortic wall

While dissected aortic wall models already have been developed, they significantly simplify either the wall geometry or material behavior. Moreover, the impact of an uncertain wall thickness and stiffness on the resulting wall stress and deformation has not yet been evaluated, while these parameters cannot be accurately retrieved from the clinical imaging modalities used for aortic dissections. Therefore, this chapter presents the development of a physiology-inspired dissected aortic wall model that includes a state-of-the-art pre-stressed material model and is utilized to quantify the effect of unknown material and geometrical parameters on the predicted wall stress and deformation.

This chapter is based on the paper "*Uncertainty quantification of the wall thickness and stiffness in an idealized dissected aorta*", published in the *Journal of the Mechanical Behavior of Biomedical Materials* [195].

7.1 INTRODUCTION

A type B aortic dissection is a disease that is characterized by a delamination of the inner part of the descending thoracic aortic wall, i.e. the intimal and a part of the medial layer. In the presence of one or more tears, this delamination allows the blood to flow along its

normal pathway via the true lumen as well as along an alternative channel in between the dissected membrane and the remaining part of the wall, i.e. the false lumen. An example of such a patient-specific anatomy is shown in figure 7.1. Although the incidence rate is limited to 1.85/100,000, severe long-term complications such as aortic expansion, spinal cord ischemia, renal failure, paraplegia and aortic rupture can occur if the disease is not treated properly [1–3]. A common treatment for type B aortic dissections is thoracic endovascular aortic repair (TEVAR), implying that a stent-graft is implanted at the site of the proximal tear in order to seal off the false lumen. By sealing it off, surgeons aim to trigger complete thrombus formation of the false lumen, which results in healing of the dissection. Although TEVAR has a high acute success-rate, the long-term success rate of complete false lumen thrombosis varies from 91% to values of only 22% [47, 90, 91]. Moreover, while some of the remaining patients show a fully patent false lumen, partial thrombosis was observed for ca. 10% of the treated patients in most studies, which was found to result in a higher mortality rate [47, 91–93]. Furthermore, 20% to 30% of the treated patients requires a re-intervention within the first year post-TEVAR and an expanded aortic diameter was observed for a similar fraction of the patients within the first year too [2, 4]. It is, however, not yet elucidated how to determine *a priori* for which patients the desired outcome will be achieved.

Computational biomechanical models of the blood flow, dissected aortic wall and stent-graft deployment can contribute in gaining insight into the acute, mid- and long-term effect of TEVAR. Models of the dissected aortic wall with varying geometrical and material complexity have been proposed. Indeed, some geometrically patient-inspired and -specific dissected wall models have been developed as part of a fluid-structure-interaction model, which most often leads to a simplified single-layered soft tissue model with a linear elastic or an isotropic hyperelastic behavior [21, 138–140]. Moreover, only the model of Bäumlér et al. included the effect of pre-stress, confirming its large effect on the resulting model stresses and strains [21, 101, 124]. Others integrated advanced anisotropic hyperelastic material models, including the effect of elastin and collagen, with a medial and adventitial layer in their, axially stretched and/or residually stressed, dissected wall model [65, 71, 72, 145, 146]. They mainly focused on the dissection propagation, while limiting the geometrical complexity. In this respect, Zhang et al. modeled dissected membrane buckling, caused by an artificially induced dissection, in a residually stressed, though unloaded, circular sample of the aortic wall

[144]. In an attempt to include dissection propagation in the model, Rolf-Pissarczyk et al. developed a constitutive law that includes the degradation of the elastic fibers that interconnect the elastic lamellae in the media and applied it to an axially stretched and pressurized idealized dissected wall [147]. No models were found that accounted for both the geometrical complexity and the constituent-specific and, consequently, anisotropic material behavior, which might affect the result when aiming at the long-term outcome prediction of type B dissections.

Moreover, in most of these models, assumptions regarding the material behavior, the thickness of the non-dissected aortic wall and the fraction of the dissected membrane and, if applicable, the medial thickness have inevitably been made. Often, the acquired values were adopted from literature, as an idealized geometry was considered or no patient-specific structural data was available. In the current clinical practice, these thickness and stiffness parameters can, indeed, not be retrieved from the standard imaging modalities, which are mainly contrast-enhanced computed tomography (CT) scans with typical image resolutions in the axial plane in the order of 0.60 mm to 1.00 mm for qualitative scans, according to the authors' experience. Insight into the effect of these parameters on the predicted output is essential when envisioning models that assist in the clinical decision making for the treatment of type B aortic dissections. To the best of the authors' knowledge, the uncertainty induced by an unknown true wall thickness and stiffness of the dissected aorta on the predicted wall stress and deformation has not yet been investigated.

Therefore, this study aims (i) to develop an idealized dissected aortic wall framework that includes an anisotropic hyperelastic material model with a medial and adventitial layer that (ii) enables the quantification of the global uncertainty of the characteristic deformation patterns and maximum principal stress values with respect to varying wall stiffness and thickness parameters and the parameter-specific contributions of these parameters to the uncertainty.

7.2 METHODS

An overview of the main uncertainty analysis is presented in figure 7.2. First, section 7.2.1 describes the general model framework of the dissected aortic wall. This model framework is, in section 7.2.2, applied to assess the uncertainty induced by unknown thickness and stiffness parameters (section 7.2.2.1) on the wall displacement and

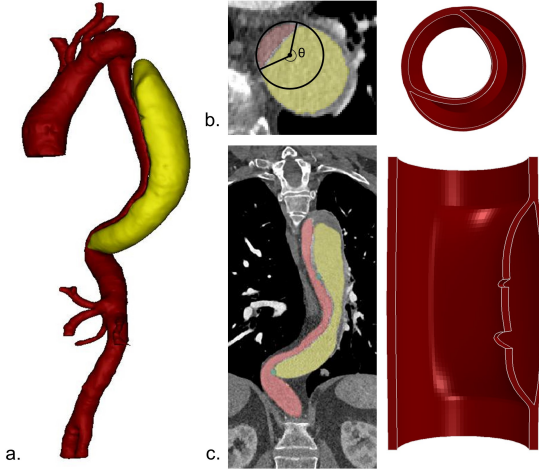


Figure 7.1: Overview of a patient-specific anatomy of a type B aortic dissection and the corresponding views of the idealized dissection model. (a) three-dimensional segmentation of an aortic dissection obtained from a patient-specific CT scan, together with (b) an axial and (c) a coronal slice and the corresponding view of the dissected wall model. On the CT slices, the true lumen is indicated in red, the false lumen in yellow and the tears in green. On (b) the axial slice, the best-fit circle of the intact true lumen wall is indicated together with the circumferential angle θ that covers the dissected membrane.

stress (section 7.2.2.2). In section 7.2.2.3, the uncertainty is assessed on a global level, i.e. related to the combined effect of the considered input parameters for a set of 300 finite element analyses. In section 7.2.2.4, the uncertainty analysis is extended to the parameter-specific level, in which the contribution of each input parameter to the global uncertainty is assessed, which requires the development of a surrogate model to generate the necessary large number (10,000) of model results. Finally, section 7.2.3 considers the impact of some intrinsic assumptions of the model framework.

7.2.1 Dissected wall model framework

7.2.1.1 Geometry and mesh

The dissected wall model was generated starting from a cylindrical geometry with a length of 60.00 mm and a diameter of 27.30 mm, which is in the range of reported diameters of descending thoracic aortas without dissection [184, 196, 197]. The false lumen, with an axial length of 40.00 mm, and the tears were inserted at predetermined locations, thus creating a dissected membrane and a remain-

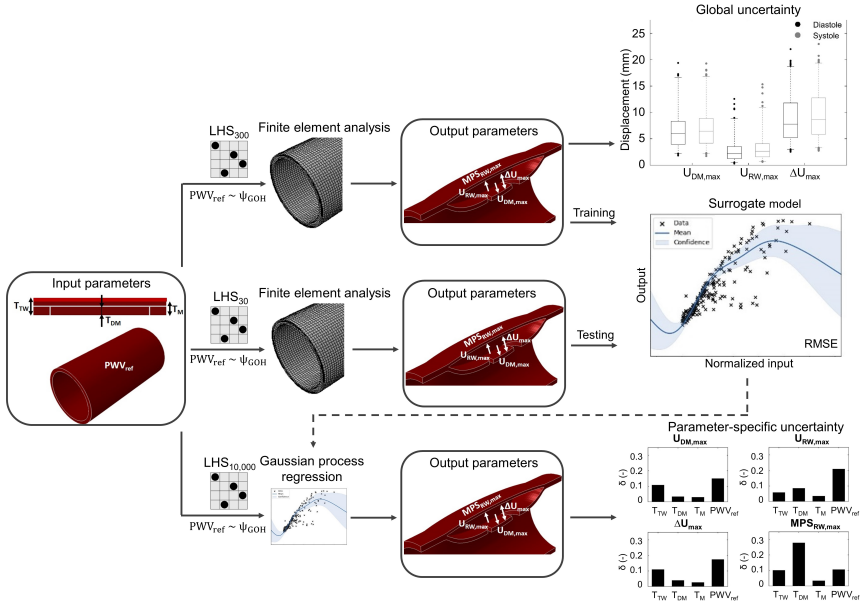


Figure 7.2: Overview of the general workflow for the global uncertainty quantification and the parameter-specific contributions. The input parameters T_{TW} , T_{DM} , T_M and PWV_{ref} refer, respectively, to the total wall thickness, the relative dissected membrane thickness, the relative medial thickness and the pulse wave velocity of the reference model. The four output parameters $U_{DM,max}$, $U_{RW,max}$, ΔU_{max} and $MPS_{RW,max}$ indicate the maximal displacement of the dissected membrane, the maximal displacement of the remaining wall, the maximal distance between the dissected membrane and remaining wall and the maximal principal Cauchy stress at the maximal displacement of the remaining wall. The Latin hypercube samplings with 30, 300 and 10,000 samples are abbreviated as LHS₃₀, LHS₃₀₀ and LHS_{10,000}.

ing wall (figure 7.3). The circumferential false lumen size was determined based on the pre-operative CT scans of a patient-specific case with a type B dissection, obtained from the University Hospital of Düsseldorf with consent of the local ethical committee (reference number: 2017064325) [198]. To do so, the healthy pre-dissection diameter was estimated as the diameter of the best-fit circle based on the curvature of the true lumen wall, for each axial CT slice of the dissection in which the true and false lumen could be distinguished (figure 7.1(b)). The circumferential false lumen size was then determined as the angle, within that best-fit circle, that covered the section with dissected wall tissue. Calculating the median angle over the axial CT slices, lead to a circumferential false lumen size of 245° .

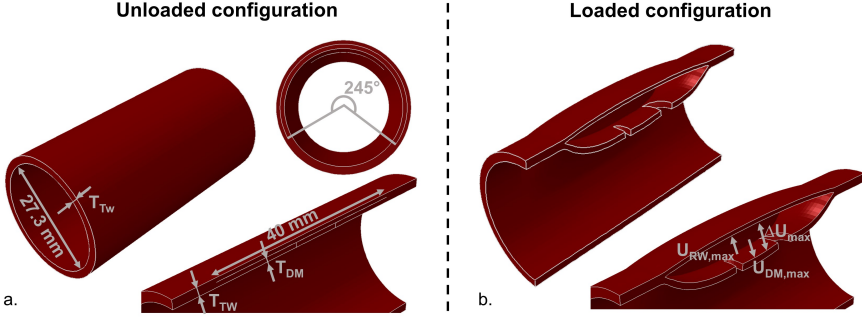


Figure 7.3: Geometry of the idealized dissection model in the (a) unloaded and (b) loaded configuration at diastolic pressure (80 mmHg). On the unloaded configuration, T_{TW} and T_{DM} , i.e. the total wall and the relative dissected membrane thickness, are indicated. On the loaded configuration, the displacement output parameters are visualized, with $U_{DM,max}$, $U_{RW,max}$ and ΔU_{max} being, respectively, the maximal displacement of the dissected membrane, the maximal displacement of the remaining wall and the maximal distance between the dissected membrane and the remaining wall.

7.2.1.2 Material behavior

The dissected aortic wall contained a medial and adventitial layer, both behaving as an incompressible anisotropic hyperelastic Gasser-Ogden-Holzapfel (GOH) material [15]. The strain energy density function of each layer, Ψ_{layer} , was defined as

$$\Psi_{layer} = c_{10}(I_1^e - 3) + \frac{k_1}{2k_2} \left(\sum_{j=4,6} e^{k_2(\kappa I_1^c + (1-3\kappa)I_j^c - 1)^2} - 1 \right) \quad (7.1)$$

with c_{10} representing the elastin shear modulus, k_1 the collagen fiber stiffness, k_2 the intrinsic collagen fiber stiffening, κ the collagen fiber dispersion and α the mean collagen fiber angle with respect to the circumferential direction. The first, fourth and sixth invariant of the constituent Cauchy-Green tensor \mathbf{C}^i are, respectively, indicated by I_1^i , I_4^i and I_6^i . The superscripts e and c , respectively, refer to elastin and collagen.

Physiological ranges for the medial and adventitial material parameters were determined, based on reported uniaxial and biaxial experimental data of (descending) thoracic aortas without dissection (table 7.1) [8, 186]. The stiffness of the elastin and collagen of the adventitial layer, indicated with index A , was assumed to depend on

that of the medial layer, indicated with index M , by accounting for the relative area fraction of elastin and collagen in both material layers [12]. Moreover, all collagen fibers of the aortic wall were assumed to have the same intrinsic stiffening and, hence, k_2 . Combining these assumptions with equation (7.1) resulted in

$$\Psi_M = c_{10M}(I_1^e - 3) + \frac{k_{1M}}{2k_2} \left(\sum_{j=4,6} e^{k_2(\kappa_M I_1^c + (1-3\kappa_M)I_j^c - 1)^2} - 1 \right) \quad (7.2)$$

$$\Psi_A = c_{10A}(I_1^e - 3) + \frac{k_{1A}}{2k_2} \left(\sum_{j=4,6} e^{k_2(\kappa_A I_1^c + (1-3\kappa_A)I_j^c - 1)^2} - 1 \right) \quad (7.3)$$

$$\text{with } c_{10A} = 0.34c_{10M} \text{ and } k_{1A} = 1.17k_{1M}. \quad (7.4)$$

The *in vivo* pre-stretched state of the aortic wall was integrated using a Matlab (The MathWorks Inc., USA) implementation of the deposition stretch algorithm of Famaey et al. for thick-walled cylinders [126, 185]. The collagen and axial elastin deposition stretch was assumed to remain constant throughout the geometry and equal to 1.10, representative for the descending aorta of a 65 year old person, which corresponds to the average age of a patient with a type B aortic dissection [103, 198].

The selection of GOH parameters was coupled to the pulse wave velocity (PWV) of a reference cylinder, PWV_{ref} , at diastolic pressure (80 mmHg). By using PWV_{ref} as a representation of the aortic wall stiffness, GOH parameter combinations that lead to a physiological material behavior were ensured. Therefore, a full factorial design was performed on discretized physiological ranges of the GOH parameters, to eliminate incompatible combinations (table 7.1, chapter 6) [171]. For each combination of the full factorial design, the deposition stretches at 80 mmHg were calculated for a cylindrical thick-walled reference model with dimensions corresponding to the average values of the applied thickness ranges as reported in table 7.1 [185]. The combinations leading to a tensile circumferential elastin deposition stretch, g_{circ}^e , throughout the wall were retained as they complied with the assumption that elastin has been stretched during human development [111, 112]. The PWV at 80 mmHg was then calculated for the resulting GOH parameter combinations. Consequently, the GOH parameter combination with the PWV_{ref} that best matched the required PWV, was selected.

Table 7.1: Overview of the applied input ranges for the Latin hypercube sampling and the full factorial design, performed to couple the GOH parameters for the media and adventitia to the PWV_{ref} , similar to chapter 6 [171]. The corresponding references are mentioned as well. LB and UB, respectively, indicate the lower and upper bound of the range.

Parameter	Meaning	Range			Reference
		LB	UB	Mean	
Thickness					
T_{TW} (mm)	Total wall thickness	1.30	2.50	1.90	[7–9, 199–203]
T_M ($\%T_{TW}$)	Medial thickness, relative to total wall	65	85	75	[6–9]
T_{DM} ($\%T_M$)	Dissected membrane thickness, relative to media	50	90	70	[6, 9]
Stiffness					
PWV_{ref} (m/s)	PWV of reference cylinder	4.00	12.00		[181]
c_{10M} (MPa)	Elastin stiffness in media	0.005	0.025		[8, 186]
k_{1M} (MPa)	Collagen stiffness in media	0.0002	1.000		[8, 186]
k_{2M} (-)	Collagen stiffening in media	4.0	35.0		[8, 186]
α_M ($^\circ$)	Mean fiber angle in media	0.0	45.0		[7, 16]
κ_M (-)	Fiber dispersion in media	0	1/3		[15]
α_A ($^\circ$)	Mean fiber angle in adventitia	45.0	90.0		[7, 16]
κ_A (-)	Fiber dispersion in adventitia	0	1/3		[15]

7.2.1.3 Finite element analysis

The *in vivo* mechanical loading state of the dissected aorta at a physiological diastolic (80 mmHg) and systolic (120 mmHg) blood pressure was modeled using a finite element analysis in Abaqus/Standard (Dassault Systèmes, France). The cylindrical geometry (section 7.2.1.1) was meshed with hybrid hexahedral elements, using the in-house developed software pyFormex for geometrical operations and pre- and post-processing of finite element analyses [123, 204]. Herein, the tears and false lumen were implemented as unconnected elements at the corresponding interfaces (figure 7.3).

To compute the deformed dissected wall configuration, first, the deposition stretches were calculated for the healthy cylindrical aortic wall, i.e. without tears or false lumen, at the location of the element centroid (section 7.2.1.1). The *in vivo* diastolic configuration was then obtained by applying the resulting deposition stretches to the dissected wall model together with the diastolic pressure, both in the true and false lumen. Since the mesh consists of unconnected elements at the tears and the false lumen, this allowed the dissected membrane to deform as a result of the release of the residual stresses. This approach ensured a realistic deformation of the dissected wall. Next, the intra-arterial pressure in the true and false lumen was further increased to systolic pressure. As the same pressure was applied to the true and false lumen, no net pressure gradient over the dissected membrane was assumed. At the proximal and distal end of the model, only radial displacement was allowed.

To ensure mesh-independent results, a mesh sensitivity study, with the number of elements ranging from 36,000 to 162,000, was performed for a reference geometry with average wall thickness parameters (table 7.1) and a stiffness corresponding to a physiological PWV of 5.00 m/s [181].

7.2.2 Uncertainty quantification of unknown thickness- and stiffness parameters

7.2.2.1 Input parameters and sampling

The uncertainty related to the unknown material stiffness and wall thickness was quantified using four input parameters: (i) the total wall thickness (T_{TW} ; mm); (ii) the medial thickness relative to T_{TW} (T_M ; % of T_{TW}); (iii) the dissected membrane thickness relative to T_M (T_{DM} ; % of T_M) and (iv) PWV_{ref} as representation of the aortic wall stiffness. T_M and T_{DM} were expressed relative to T_{TW} and T_M ,

respectively, to ensure parameter independence. The use of PWV_{ref} allows a continuous sampling of the stiffness parameter, while avoiding incompatible GOH parameter combinations (section 7.2.1.2).

The four-dimensional (4D) input parameter space was sampled using a Latin hypercube sampling, which is more efficient and robust compared to a random Monte Carlo sampling [165]. This sampling implies that each input parameter was divided into intervals of equal probability, which are represented by one sample only. A uniform probability distribution was assumed for the four independent input parameters.

Note that each sample contains a PWV_{ref} , obtained for a reference cylinder with an average T_{TW} and T_M , and thickness values that, most likely, deviate from these average thicknesses. As the deposition stretch has to reflect the effective residual stresses in the considered sample geometry, the corresponding g_{circ}^e was calculated for the selected GOH parameters, based on PWV_{ref} , and the sample thicknesses, instead of the reference model with average thickness parameters. Consequently, the sample g_{circ}^e might be compressive, while only tensile g_{circ}^e are considered to be physiological (section 7.2.1.2). Therefore, samples leading to a compressive g_{circ}^e were excluded from the uncertainty analysis.

7.2.2.2 Output parameters

In total, four output parameters were considered. To determine the uncertainty related to the dissected wall deformation, the following output parameters were determined: (i) the maximal displacement of the dissected membrane relative to the healthy cylindrical configuration, $U_{DM,max}$, (ii) the maximal displacement of the remaining wall relative to the healthy configuration, $U_{RW,max}$, and (iii) the maximal distance between initially coinciding nodes of the dissected membrane and remaining wall, ΔU_{max} , which corresponds to the maximal distance between the dissected membrane and remaining wall as visible on clinical CT scans. Furthermore, (iv) the maximum principal Cauchy stress at the location of $U_{RW,max}$, $MPS_{RW,max}$, was assessed, by averaging the maximal principal stress over the integration points of the elements that surround the considered node and the corresponding nodes on the same radial axis throughout the remaining wall. It is noteworthy, that $MPS_{RW,max}$ does not necessarily correspond to the maximal stress in the remaining wall. However, as the acute dissected wall was of interest, rather than the potential of the dissection to propagate, the choice was made to exclude the

regions at the false lumen boundaries and to focus on the stress at the location of the largest remaining wall deformation, which is often essential in the estimation of the rupture risk.

7.2.2.3 *Global uncertainty quantification based on finite element analyses*

The combined effect of the uncertainty on the four independent input parameters was assessed using a Latin hypercube with 300 samples (LHS₃₀₀). For each sample with a corresponding $g_{circ}^e \geq 1.00$ (section 7.2.1.2), a finite element analysis was performed with the dissected wall model framework that was adapted according to the considered stiffness and thickness parameters. For each of the four output variables, the median value as well as the interquartile range (IQ) and the interval between the minimum and maximum value (min-max) over the LHS₃₀₀ were determined.

7.2.2.4 *Parameter-specific contribution to global uncertainty based on surrogate models*

To quantify the parameter-specific contribution to the global uncertainty related to the idealized dissected wall model, large amounts of samples need to be assessed, which would be too computationally expensive when using finite element analyses. Therefore, the development of a surrogate model is discussed before continuing with the analysis of the parameter-specific contribution to the global uncertainty.

Surrogate model of the dissected wall

A surrogate model was developed based on the input from the LHS₃₀₀ and the corresponding results obtained with the finite element analyses. As the relatively limited amount of input samples might introduce uncertainty in the surrogate model, it was opted to train a Gaussian process regression model, which accounts for the uncertainty in the surrogate model itself, instead of a regular neural network, using the open-source package GPy in Python 3.7 [205].

Here, an important consideration is that it is the aim of the Gaussian process regression to surrogate the finite element analysis as accurately as possible. Given that perspective, PWV_{ref} (as an encompassing material parameter) was replaced by the corresponding seven GOH parameters and the calculated g_{circ}^e at the inner radius of the sample geometry, similar to the input for the finite element analyses. Thus, when combined with the three thickness input parameters, this results in a Gaussian process with 11 input parameters.

The input parameters were normalized between 0 and 1, by

$$x_{i,norm} = \frac{x_i - x_{i,min}}{x_{i,max} - x_{i,min}}, \quad (7.5)$$

with $x_{i,norm}$, $x_{i,min}$ and $x_{i,max}$ being the respective normalized, minimal and maximal value of input parameter X_i . For the output parameters, the mean was subtracted in order to comply to the zero-mean assumption during the training of the Gaussian process. No further normalization was applied, to facilitate the interpretation of the predicted output.

The Gaussian process was trained by using a radial basis function of the form

$$K_{GP}(\mathbf{x}, \mathbf{x}') = \sigma^2 e^{-\frac{1}{2} \frac{\|\mathbf{x} - \mathbf{x}'\|^2}{L^2}} \quad (7.6)$$

as kernel, with \mathbf{x} and \mathbf{x}' two points in the multi-dimensional input space, σ the variance and L the length scale, both being hyperparameters of the Gaussian process. While the kernel contains one σ parameter, an anisotropic kernel with a different length scale for each input parameter was included. The hyperparameters were determined by optimizing the log-likelihood during the training process in maximally 100,000 iterations. The process was trained on the available samples of the LHS₃₀₀ and a new, randomly generated, LHS₃₀ was used as test set. The root mean squared error (RMSE) was calculated for the test set. A RMSE ≤ 1.00 mm was pursued for the displacement output parameters to limit the mean error to a representative pixel size of a clinical CT scan. No predefined RMSE for $MPS_{RW,max}$ was assigned, as not much is currently known regarding the stress in a dissected wall.

Delta moment-independent analysis

The trained surrogate model was used to perform a global sensitivity analysis in order to gain insight into the effect of the uncertainty on the individual input parameters. Therefore, the trained Gaussian processes were applied to calculate the output of a Latin hypercube sampling of 10,000 samples (LHS_{10,000}) based on the four independent input parameters (T_{TW} , T_M , T_{DM} and PWV_{ref}) as discussed in section 7.2.2.1. To be consistent with the finite element analyses, the GOH parameter combination that lead to the closest PWV compared to the required PWV_{ref} was determined for each of the 10,000 samples, the corresponding sample g_{circ}^e was calculated and samples leading to $g_{circ}^e < 1.00$ were excluded (section 7.2.2.1). Of the remaining samples, those leading to an output value in the lower and

upper 2.5% were excluded to limit the weight attributed to these extreme values, which might potentially be the result of regions of large uncertainty in the Gaussian process and, thus, less reliable.

The remaining samples of the LHS_{10,000}, combined with the determined results for the four considered output parameters, were subjected to a δ moment-independent analysis, using the SALib python package [161, 206]. This analysis considers the importance of each input parameter, by taking into account the complete output distribution, instead of a moment of the distribution, i.e. a characteristic of the distribution shape as the variance or skewness. Indeed, δ_i considers the expected shift between the unconditional and conditional output distribution for an input parameter X_i and is, thus, defined as

$$\delta_i = \frac{1}{2}E_{X_i}[s(X_i)] \text{ with} \quad (7.7)$$

$$s(X_i) = \int |f_Y(y) - f_{Y|X_i}(y)|dy \text{ and} \quad (7.8)$$

$$E_{X_i}[s(X_i)] = \int f_{X_i}(x_i)[s(X_i)]dx_i. \quad (7.9)$$

E_{X_i} indicates the expected value of shift s for input parameter X_i , which considers the difference between $f_Y(y)$ and $f_{Y|X_i}(y)$ that, respectively, indicate the unconditional distribution of output Y and the conditional distribution of output Y for a known input parameter X_i .

7.2.3 Additional sources of uncertainty

In this section, the impact of some intrinsic assumptions of the model framework and their contribution to the output uncertainty is considered.

7.2.3.1 Pressure gradient

The standard model framework does not include a pressure gradient over the dissected membrane, while pressure differences of 3 mmHg between the true and false lumen have been measured *in vivo* [207]. To assess the impact of neglecting the pressure gradient, a pressure difference of 3 mmHg over the dissected membrane was applied to 10 randomly selected samples of the LHS₃₀₀. Similar to the *in vivo* measurements, the higher pressure was located in the false lumen in diastole and in the true lumen during systole [207]. The difference in output was assessed using the median value of the difference between the results obtained with and without pressure gradient at the considered loading state, i.e. either diastole or systole. The width of the

min-max range was determined too to assess the effect on the output uncertainty. Moreover, by taking the difference between $U_{DM,max}$ at diastolic and systolic pressure with the inclusion of the pressure gradient, the dissected membrane movement was estimated.

7.2.3.2 Axial dissection length

Compared to *in vivo* observations, where type B dissections often distend from the arch to the abdominal aorta, an axial dissection length of 40.00 mm is rather limited [21, 22, 47]. To assess the effect of this assumption on the output parameters, a slice model of the idealized dissected wall, i.e. without tears or proximal and distal connection between the dissected membrane and the remaining wall, with an axial length of 5.00 mm was developed. Accordingly, this slice model represents an infinitely long dissection and, thus, the expected upper boundary of the potential dissected membrane displacement for the considered samples. The slice model was applied to 10 samples, randomly chosen from LHS₃₀₀, i.e. the same samples as in section 7.2.3.1. The impact on the output parameters was determined as the median difference between the result of the idealized dissected wall and slice model. The effect on the output uncertainty range was considered by using the min-max range.

7.3 RESULTS

7.3.1 Reference dissected wall model

The results of the idealized dissected wall model are similar for the reference geometry irrespective of the element number. Indeed, the results of the finer meshes (with 54,000 to 162,000 elements) deviate 0.5% to 2.8% from those of the coarsest mesh (with 36,000 elements) for the considered wall displacement and stress output parameters. The computational time increases from 13 minutes with 5 cores to 55 minutes with 16 cores (250 GiB RAM and 180 GB local storage per core) with an increasing element number. Due to the minor differences in the output parameters, it is opted to perform the uncertainty analysis with the coarsest mesh to minimize the computational cost.

Figure 7.4 illustrates the deformation and maximal principal wall stress obtained for the reference model with the final (coarsest) mesh at diastolic and systolic pressure. The maximal deformation of the remaining wall and the dissected membrane is observed at the central part of the dissection. While a local increase in maximal principal wall stress is observed in the remaining wall at the location of separation with the dissected membrane, the central part of the membrane shows negligible stresses.

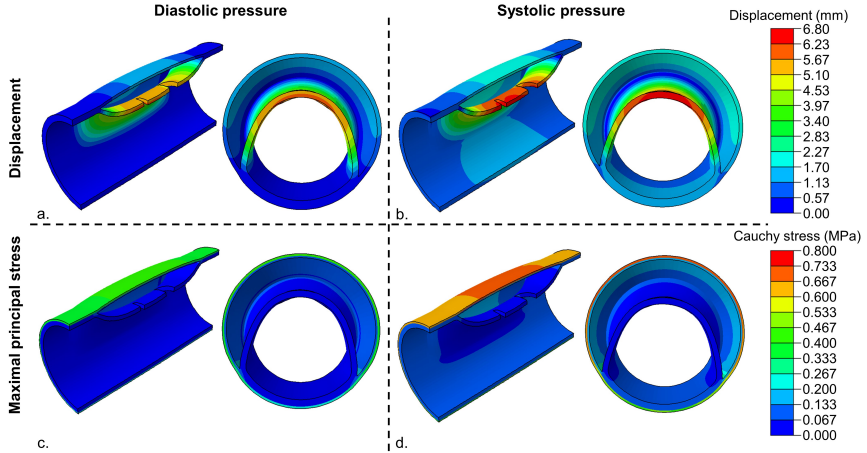


Figure 7.4: Overview of the resulting (a, b) displacement magnitude, with respect to the undeformed configuration, and (c, d) maximal principal wall stress of the reference model at (a, c) diastolic (80 mmHg) and (b, d) systolic (120 mmHg) pressure.

7.3.2 Global uncertainty quantification based on finite element analyses

Out of the 300 samples from the LHS_{300} , 237 useful results are obtained. From the 63 excluded samples, 25 do not fulfill the convergence criteria of the finite element analysis, while 38 samples result in non-physiological deposition stretches ($g_{circ}^e < 1.00$) when applying the algorithm to the sample instead of the reference geometry. The non-physiological deposition stretches are obtained for sample geometries with a larger absolute medial thickness than the reference model. Figure 7.5 illustrates the displacement magnitude of 12 example deformed configurations at diastolic pressure, with respect to the initial cylindrical configuration. Some examples of representative maximal principal stress patterns are shown in appendix A (section 7.6). While the complete overview of input and output parameters is reported in the supplementary material of the online version of the paper, the median values and the IQ and min-max uncertainty ranges of the 237 samples for the four output parameters, at the considered pressures, are shown in figure 7.6 and summarized in table 7.2 [195]. Larger median displacements were obtained for parameters involving the dissected membrane ($U_{DM,max}$ and ΔU_{max}) compared to those obtained for $U_{RW,max}$ at both pressure levels. When going from diastolic to systolic pressure, the median displacements show a maximal increase of 0.84 mm. Similarly, the highest median $MPS_{RW,max}$ was found at 120 mmHg. The fraction of the IQ range, relative to the

min-max range, varies from 24% to 34% for the displacement parameters that include the dissected membrane deformation ($U_{DM,max}$ and ΔU_{max}) and from 14% to 18% for parameters related to the remaining wall ($U_{RW,max}$ and $MPS_{RW,max}$), at both diastole and systole. Higher fractions were observed for the fourth quartile for all output parameters, with intervals ranging from 51% (for ΔU_{max} at systolic pressure) to 80% (for $MPS_{RW,max}$ at diastolic pressure).

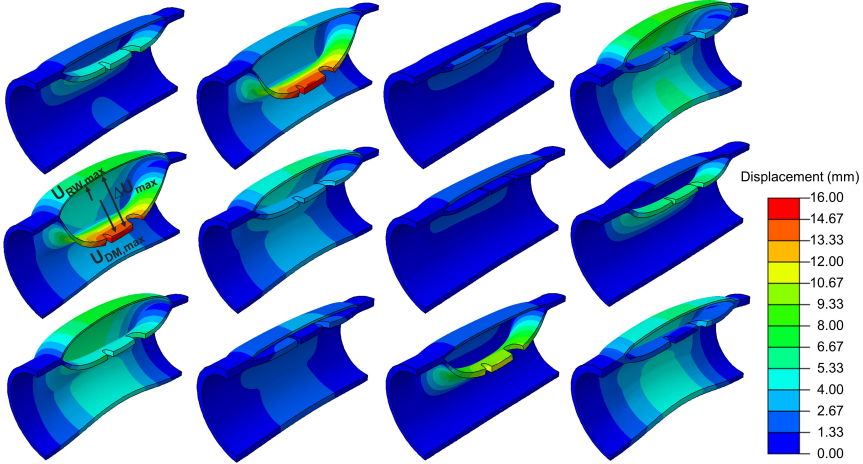


Figure 7.5: Overview of the deformed dissected wall configuration at diastolic pressure (80 mmHg) of 12 example samples of the LHS₃₀₀. The color scale indicates the displacement of the nodes with respect to the initial cylindrical configuration. The output parameters $U_{DM,max}$, $U_{RW,max}$ and ΔU_{max} are indicated for one example configuration and, respectively, correspond to the maximal displacement of the dissected membrane, the maximal displacement of the remaining wall and the maximal distance between the dissected membrane and remaining wall.

7.3.3 Parameter-specific contribution to global uncertainty based on surrogate models

7.3.3.1 Surrogate model of the dissected wall

The Gaussian processes are trained on the 237 samples of the LHS₃₀₀ and tested on 26 samples, obtained from the LHS₃₀ after excluding the samples with a $g_{circ}^e < 1.00$ for the sample geometry. The RMSE of the Gaussian processes varies from 0.73 mm to 1.43 mm for the displacement output parameters and from 0.075 MPa to 0.120 MPa for $MPS_{RW,max}$ at diastolic and systolic pressure (appendix B, section 7.7). This translates into RMSE values between 10% and 22% of the corresponding median values, based on the LHS₃₀₀ results, for

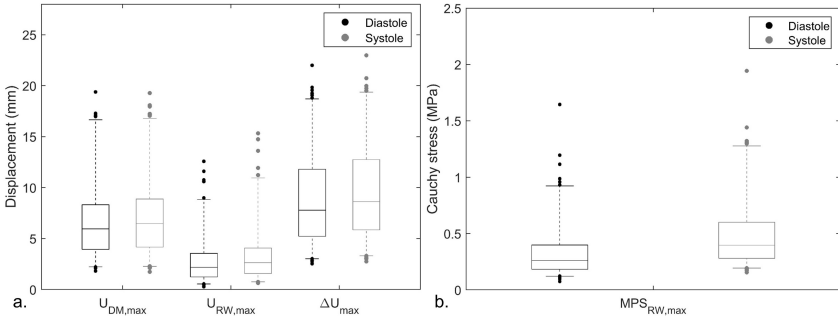


Figure 7.6: Boxplots of the 237 deformed configurations at diastolic (80 mmHg) and systolic (120 mmHg) pressure. The output (a) displacements $U_{DM,max}$, $U_{RW,max}$ and ΔU_{max} and (b) Cauchy stress $MPS_{RW,max}$ represent the maximal displacement of the dissected membrane, the maximal displacement of the remaining wall, the maximal distance between the dissected membrane and remaining wall and the maximal principal Cauchy stress at the maximal displacement of the remaining wall. The span of the whiskers represents the central 95% of the output values.

Table 7.2: Median value, interquartile (IQ) and min-max ranges of $U_{DM,max}$, $U_{RW,max}$ and ΔU_{max} and $MPS_{RW,max}$ of the 237 deformed configurations at diastolic (80 mmHg) and systolic (120 mmHg) pressure. The IQ and min-max ranges are expressed as the absolute deviation with respect to the corresponding median value.

Output	Median	IQ range	min-max range
Diastole			
$U_{DM,max}$ (mm)	5.95	[-1.99; 2.28]	[-4.13; 13.44]
$U_{RW,max}$ (mm)	2.19	[-0.96; 1.31]	[-1.91; 10.38]
ΔU_{max} (mm)	7.78	[-2.55; 4.01]	[-5.24; 14.22]
$MPS_{RW,max}$ (MPa)	0.259	[-0.076; 0.138]	[-0.183; 1.383]
Systole			
$U_{DM,max}$ (mm)	6.46	[-2.29; 2.36]	[-4.72; 12.81]
$U_{RW,max}$ (mm)	2.64	[-1.06; 1.40]	[-2.01; 12.68]
ΔU_{max} (mm)	8.62	[-2.76; 4.12]	[-5.87; 14.36]
$MPS_{RW,max}$ (MPa)	0.397	[-0.117; 0.202]	[-0.242; 1.547]

$U_{DM,max}$ and ΔU_{max} , while errors from 30% to 48% are obtained for $MPS_{RW,max}$ and $U_{RW,max}$. The output distribution obtained as result of the Gaussian process and the $LHS_{10,000}$ was compared to the one based on the finite element analyses of LHS_{300} , as indicated in figure 7.7(a, b). In particular, the central 95% of the output distribution was found to be comparable.

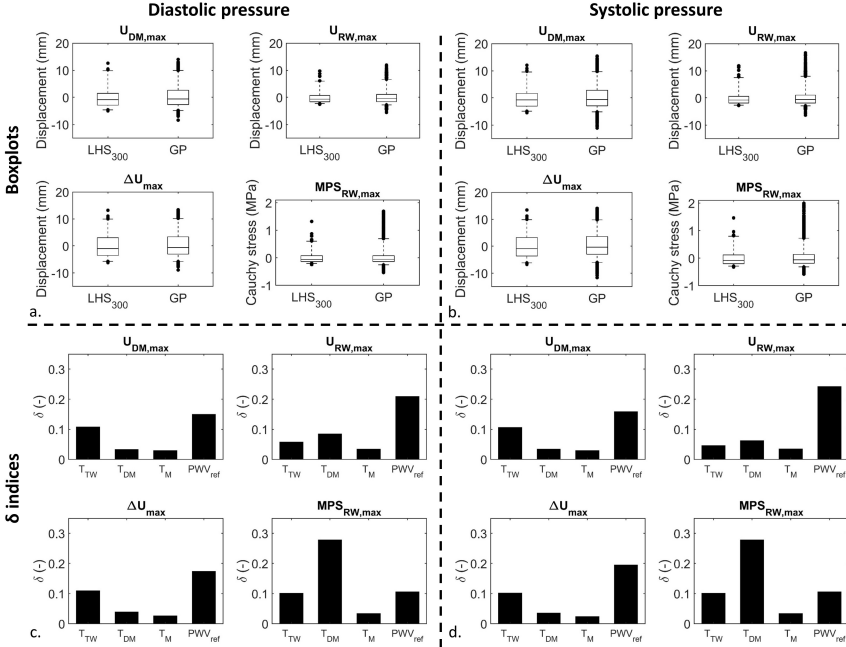


Figure 7.7: The resulting (a, b) boxplots based on the LHS_{300} and the Gaussian process (GP) with the corresponding (c, d) δ indices at (a, c) diastolic (80 mmHg) and (b, d) systolic (120 mmHg) pressure. The output parameters $U_{DM,max}$, $U_{RW,max}$, ΔU_{max} and $MPS_{RW,max}$ indicate the maximal displacement of the dissected membrane, the maximal displacement of the remaining wall, the maximal distance between the dissected membrane and remaining wall and the maximal principal Cauchy stress at the maximal displacement of the remaining wall. The whiskers of the boxplots show the central 95% of the output values, i.e. the values used for the δ moment-independent analysis.

7.3.3.2 Delta moment-independent analysis

The δ indices at diastolic and systolic pressure, resulting from the application of the Gaussian process on the performed $LHS_{10,000}$ sampling are shown in figure 7.7(c, d) and appendix C (section 7.8). The thickness input parameters lead to $\delta \leq 0.11$ for $U_{DM,max}$,

$U_{RW,max}$ and ΔU_{max} . While T_{TW} is the thickness parameter that affects the displacement output distribution the most for $U_{DM,max}$ and ΔU_{max} , T_{DM} and T_M induce a minor shift in output distribution ($0.02 \leq \delta \leq 0.08$). For $U_{RW,max}$, all thickness parameters resulted in $\delta \leq 0.08$, with T_{DM} being slightly more important compared to T_{TW} and T_M . The input parameter with the highest importance for all displacement output parameters is PWV_{ref} , with $0.15 \leq \delta \leq 0.24$. On contrary, for $MPS_{RW,max}$, the largest impact is attributed to T_{DM} with $0.28 \leq \delta \leq 0.30$. The distribution is to a lesser extent affected by T_{TW} and PWV_{ref} ($0.10 \leq \delta \leq 0.11$) and T_M ($\delta = 0.03$).

7.3.4 Additional sources of uncertainty

7.3.4.1 Pressure gradient

The absolute values of the median displacement differences, with respect to the corresponding results without pressure gradient, are larger at diastolic than at systolic pressure, but remain below 1.00 mm (table 7.3). In diastole, the magnitude of $U_{DM,max}$ and ΔU_{max} increases, while a decreasing displacement magnitude is found for $U_{RW,max}$ by adding the pressure gradient. In systole, the opposite effect is observed. The impact of the pressure gradient on $MPS_{RW,max}$ is negligible with a median difference below 0.001 MPa. The width of the resulting min-max interval varies between 92% and 103% of the corresponding interval obtained without pressure gradient, again indicating a limited effect. Taking the difference between $U_{DM,max}$ of the corresponding diastolic and systolic configurations, with inclusion of the pressure gradient, results in estimated dissected membrane movements of 0.01 mm to 1.71 mm.

7.3.4.2 Axial dissection length

The slice model results in median displacement differences up to 2.08 mm and indicates an increasing displacement in $U_{DM,max}$ and ΔU_{max} , while $U_{RW,max}$ decreases (table 7.3). Similarly, the width of the min-max intervals increases for $U_{DM,max}$ and ΔU_{max} with up to 53%, compared to the idealized dissection model results, whereas a 55% decrease in interval width is observed for $U_{RW,max}$. For $MPS_{RW,max}$, the median difference is limited to an increase of 0.032 MPa, while the width of the min-max interval increases with 29%.

7.4 DISCUSSION

7.4.1 Dissected wall model framework

A computational framework for an idealized dissected two-layered aortic wall was developed. Although an idealized wall geometry is

7. UNCERTAINTY QUANTIFICATION IN AN IDEALIZED DISSECTED AORTIC WALL

Table 7.3: The effect of altering the pressure gradient or dissection length in 10 configurations, at diastolic (80 mmHg) and systolic (120 mmHg) pressure. The median value of the difference between $U_{DM,max}$, $U_{RW,max}$, ΔU_{max} and $MPS_{RW,max}$ in the adapted and the original idealized dissected wall framework is presented. The width of the min-max range obtained based on the 10 configurations is included as well and is presented relative to the min-max interval of the counterpart results of the idealized dissected model framework.

Output	Pressure gradient		Dissection length	
	Median difference	Min-max width (%)	Median difference	Min-max width (%)
Diastole				
$U_{DM,max}$ (mm)	0.69	103	1.76	153
$U_{RW,max}$ (mm)	-0.11	97	-0.80	45
ΔU_{max} (mm)	0.39	92	0.60	106
$MPS_{RW,max}$ (MPa)	-0.0004	99	0.022	122
Systole				
$U_{DM,max}$ (mm)	-0.32	94	2.08	153
$U_{RW,max}$ (mm)	0.07	101	-0.86	46
ΔU_{max} (mm)	-0.32	99	0.72	108
$MPS_{RW,max}$ (MPa)	0.0007	100	0.032	129

applied, it contains the main characteristics of an aortic dissection, i.e. the false lumen and the tears. Moreover, it includes anisotropic hyperelastic material behavior as well as deposition stretches. Despite the fact that the cause and progression of the dissection is discarded in this study, the current framework allows for an, at least partially, physiological representation of an acute aortic dissection. Indeed, the shape of the true and false lumen is not predetermined, but is created based on the release of the deposition stretches in the dissected membrane and the application of the true and false lumen pressure. Consequently, a realistic deformation is ensured, without requiring detailed knowledge on the exact cause of the dissection.

Based on the implemented framework, 237 out of the 300 considered samples (LHS₃₀₀) fulfilled the finite element analysis convergence criteria (8% of the 300 samples excluded) and resulted in $g_{circ}^e \geq 1.00$ throughout the wall for the sample geometry (13% of the 300 samples excluded). As 79% of the LHS₃₀₀ samples leads to useful results, the framework in itself was considered to be quite robust. The finite element analysis in itself was even more robust with a success rate of 90%. Indeed, after excluding the samples based on g_{circ}^e , 90% of the simulations lead to a converged result.

7.4.2 Global uncertainty quantification based on finite element analyses

Based on the developed model framework of the dissected wall and the performed finite element analyses, the overall uncertainty on the considered deformation and stresses, as a consequence of uncertain thickness and stiffness parameters, was estimated at diastolic and systolic pressure levels. Despite slight differences in the absolute median values, the magnitude of the global min-max and IQ uncertainty ranges was very similar at diastolic and systolic pressure, especially when considering the large variety in the input parameter space (figure 7.6 and table 7.2). It might, therefore, be sufficient to study the uncertainty based on one loading state for a quasi-static model.

The IQ uncertainty ranges were maximally 6.88 mm and 0.319 MPa for the displacement and stress output parameters, respectively, whereas the min-max ranges showed uncertainty intervals up to 20.22 mm and 1.788 MPa, which is in particular induced by the large variation in the fourth quartile for all output parameters (figure 7.6 and table 7.2). The min-max interval width of $U_{DM,max}$ can be interpreted as the maximal error in the predicted true lumen diameter decrease, which is linked to the risk of malperfusion. $U_{RW,max}$ can be interpreted as the maximal error in the total diameter increase, which is currently used as a clinical decision criterion. At diastolic pressure, the current study estimates model output errors up to 64% for the decrease in true lumen diameter and up to 45% for the increase in total diameter, relative to the diameter of the healthy descending aorta. Note that this interpretation implicitly assumes that axial bending of the dissected wall is negligible. Although these extreme values are expected to occur rarely, it is of major importance to acknowledge their presence, as their exclusion could result in an under- or overestimation of the malperfusion and rupture risk and, consequently, in inappropriate clinical decisions.

Despite this increased insight, the model framework is expected to underestimate the true uncertainty. Indeed, the direct coupling of PWV_{ref} to a set of GOH parameters assumes that the PWV is measured with high accuracy and fully represents the material behavior. However, some measurement errors might be expected and the PWV is mainly a stiffness measure of the circumferential behavior. Therefore, PWV is rather a guide than an exact measure to obtain proper material parameters (chapter 6) [171]. The link between the PWV_{ref} and the GOH parameter set is, consequently, not straightforward and includes additional uncertainty, which was

not accounted for in the main uncertainty analysis. The impact of the use of PWV_{ref} as material parameter is considered in appendix D (section 7.9) and reveals remarkable variations, in particular for the wall deformation, for slight changes in PWV_{ref} , while applying constant thickness parameters. Although this additional uncertainty is not accounted for in the main analysis, it does not invalidate the obtained results, but indicates that the quantified uncertainty must be considered as a lower boundary as the tissue-specific GOH parameter are often unknown.

7.4.3 Parameter-specific contribution to global uncertainty based on surrogate models

The δ moment-independent analysis shows the importance of each individual input parameter on the output distribution, thus, indicating which information is an essential prerequisite for the development of reliable predictive models (figure 7.7 and appendix C, section 6.7). T_M was found to have a negligible effect on all considered output parameters, and is, consequently, not expected to largely influence the predicted wall deformation and stress. The impact of the other thickness parameters depends on the considered output parameter. On the one hand, T_{TW} affects the output distribution of $MPS_{RW,max}$ and the displacement parameters involving the dissected membrane, i.e. $U_{DM,max}$ and ΔU_{max} , to some extent, but has little effect on the output distribution of $U_{RW,max}$. On the other hand, knowing the true value for T_{DM} is of minor importance for all displacement output parameters, but leads to the largest impact on the output distribution of $MPS_{RW,max}$. For the material stiffness, represented by PWV_{ref} , the opposite effect is noticed. Indeed, uncertainty on PWV_{ref} yields the strongest impact on the displacement output distributions, while its influence on the $MPS_{RW,max}$ distribution remains moderate. These observations suggest that, in particular, patient-specific knowledge on the global material stiffness and the relative thickness of the dissected membrane is essential when one is interested in the respective prediction of the deformation and peak wall stress in aortic dissections, which is in line with basic mechanical insights.

The actual values of the obtained δ indices might, however, be affected by the considered input parameter space and the Gaussian process regression, which depends on the specific training and test set. To assess the added value of the trained Gaussian process to quantify the parameter-specific contribution to the uncertainty, the indices obtained for the LHS_{10,000} are compared to those directly

obtained from the LHS₃₀₀ together with the corresponding 95% confidence intervals on the δ indices. As indicated in appendix C (section 7.8), most general trends are, although less pronounced, similar for both sets of δ indices, which enhances the confidence in the reported indices. Nevertheless, the confidence intervals of the indices largely decrease with an increasing number of samples, which confirms the added value of training a surrogate model based on the finite element results to perform the global sensitivity analysis. In addition, the robustness of the obtained δ indices, based on LHS_{10,000}, is tested with respect to the sampling based on the trained Gaussian process (appendix C, section 7.8). Therefore, the same LHS_{10,000} is resampled with the same Gaussian process, which yields very similar δ indices. It might, therefore, be assumed that the indices are the result of the intrinsic trends of the Gaussian process, rather than being a result of a specific sampling and, thus, the Gaussian process uncertainty.

7.4.4 Physiological relevance of idealized dissected wall framework

While mean dissected membrane movements of 1.7-5.5 mm in the descending aorta throughout the cardiac cycle have been measured *in vivo*, the idealized dissected wall model resulted in dissected membrane movements between diastolic and systolic pressure from 0.01 mm to 1.71 mm when adding a physiological pressure difference of 3 mmHg between the true and false lumen [21, 22, 207, 208]. Despite differences in the methodology to measure the dissected membrane movement over the cardiac cycle, due to the different nature of the computational and experimental results, this indicates that the model framework results in displacements which are in the same order of magnitude, but smaller compared to the *in vivo* measurements.

It is speculated that at least part of the remaining difference between the modeled and measured dissected membrane movement is related to the limited axial dissection length of 40.00 mm. Indeed, physiological dissections often extend from the left subclavian artery until the abdominal aorta [21, 22]. The slice model represents an infinitely long dissection and results at systolic pressure in a median $U_{DM,max}$ deviation of 33%, relative to the median of the corresponding idealized dissected wall samples (table 7.3). This deviation is three times higher than the median difference obtained by the addition of the pressure gradient. This suggests that the axial dissection length impacts $U_{DM,max}$ to a larger extent than the inclusion of the pressure gradient. It is, therefore, expected that an increased

axial dissection length will enhance the dissected membrane movement during the cardiac cycle.

In addition, the similarity between the wall stress pattern of the current model and the idealized dissection model of Rolf-Pissarczyk et al. (figure 3.5) supports that the limited dissected membrane movement results from the short dissection length rather than from physiological limitations of the presented model framework [147]. Indeed, in both models, local concentrations in maximal principal stress were obtained in the remaining wall at the location of separation with the dissected membrane, while the dissected membrane was found to contain negligible stresses (figure 7.4 and appendix A, section 7.6).

Despite the differences in absolute values compared to physiological measurements, it must be emphasized that the current study aims to quantify the uncertainty. On the one hand, adding the pressure gradient over the dissected membrane leads to slight deviations of 0% to 8% in the width of the min-max interval (table 7.3). On the other hand, the slice model resulted for $U_{RW,max}$ in an interval that was 55% smaller, while 53% larger ranges were obtained for $U_{DM,max}$ (table 7.3). Despite the fact that using a limited axial dissection length might underestimate the expected uncertainty, in particular for $U_{DM,max}$, it should be noted that the slice model also represents an upper boundary rather than a physiological case. Moreover, the obtained uncertainty ranges of the additional finite element analyses, still fall within the reported min-max interval based on the complete LHS₃₀₀. Therefore, the use of an idealized model framework is not expected to largely compromise the uncertainty quantification.

7.4.5 Lessons learned from surrogate modeling

In the current study, it was opted to train a Gaussian process as surrogate model, rather than a neural network. Indeed, neural networks provide a deterministic result, which is reasonable when large datasets are available and, consequently, accurate networks can be trained. Due to the computational cost, the sample number for the finite element analyses in this study is limited to 300, thus the samples do not cover the input parameter space very densely. The fact that a Gaussian process accounts for the remaining uncertainty in the surrogate model, therefore, enhances the reliability of the results of the δ moment-independent analysis. Note that the 5% extreme output values were, nevertheless, excluded to find a trade-off between the inclusion of the intrinsic uncertainty, which increases the reliabil-

ity, and the exclusion of potentially non-physiological results, which might negatively affect the reliability.

To train the Gaussian processes, the PWV_{ref} is replaced by the seven corresponding GOH material parameters (section 7.2.1.2) and the resulting sample g_{circ}^e to obtain a sufficiently low RMSE (≤ 1.00 mm) for the displacement output parameters. Although this target is not reached for the Gaussian process of $U_{DM,max}$ and $U_{RW,max}$ at systolic pressure, this methodology best approaches the RMSE requirement. Indeed, Gaussian processes trained with less input parameters result in insufficiently accurate surrogate models (appendix B, section 7.7). Note that the seven GOH parameters and the sample g_{circ}^e are also required as input to the finite element model, which justifies the obtained Gaussian processes as it follows the same steps as the finite element analysis.

Moreover, it is worth mentioning that the reported RMSE values provide an indication, rather than a general statement, as a different Latin hypercube sampling for the training and/or test set results in a different Gaussian process and/or corresponding RMSE. The effect of a different test set is assessed by generating a control test sampling $LHS_{30}^{control}$ and subjecting it to the trained Gaussian processes. Compared to the LHS_{30} , the $LHS_{30}^{control}$ yields lower RMSE values for most Gaussian processes and fulfills the required RMSE threshold of 1.00 mm for all displacement output parameters. Although these results enhance the reliability of the Gaussian processes, it mainly illustrates that caution should be taken when evaluating a Gaussian process on a single RMSE value.

Besides, one could argue whether a RMSE threshold of 1.00 mm, based on a representative resolution of clinical CT scans, is sufficiently strict for the developed surrogate models. Indeed, as the idealized deformation might underestimate the physiological one, the absolute RMSE might also be an underestimation of the expected physiological deviation, when assuming that the relative RMSE remains constant.

In this respect, it is important to emphasize that the current aim of the trained Gaussian processes is to provide insight into the uncertainty, rather than providing a clinically applicable surrogate model. As the overall output distribution obtained from the Gaussian processes was similar to those of the finite element analyses, in particular for values within the central 95% of the output distribution, the applicability of the current methodology for uncertainty quantification is supported.

Nevertheless, the technique might be promising for outcome prediction and uncertainty quantification in a clinical setting too, as it yields real-time probabilistic predictions. Indeed, accurate Gaussian processes of the false lumen size, i.e. ΔU_{max} , could for example assist in deriving proper GOH parameter combinations from the deformation of the dissection, which can be observed in clinical CT scans, and inverse Bayesian inference. However, this would require more data and/or knowledge as a prerequisite to further enhance the accuracy of the Gaussian process.

7.4.6 Limitations

Although aimed at uncertainty quantification, the current framework inevitably contains assumptions as well. The studied geometry was fixed and only one inner diameter and one configuration for the tears and false lumen was implemented. Moreover, the wall thicknesses and the deposition stretches were assumed to be homogeneous along the circumferential and axial directions, which does not correspond to the physiological reality [106, 192]. Besides, the idealized geometry deviates from a patient-specific one, not only in terms of pressure difference and dissection length as discussed above, but also in terms of geometrical complexity, as no side branches, tortuosity or external soft tissue support was included. These aspects might result in an under- or overestimation of the deformation and wall stress of the remaining wall and dissected membrane [209, 210]. Although including these complexities might further advance the translation of the obtained uncertainty results to the clinical practice in absolute terms, it was opted to use an idealized model with the most important characteristics to allow the use of a systematic approach to unravel the effect of the unknown wall thicknesses and stiffness. Moreover, the added value of the model framework is situated in the increased insight into the uncertainty quantification, on a global as well as on a parameter-specific basis.

Regarding the material behavior, the collagen fiber dispersion was considered as axisymmetric, while differences between the in- and out-of-plane dispersion have been observed [7, 16]. A material model that accounts for dispersion asymmetry, such as proposed by Holzapfel et al., is expected to more accurately approach the *in vivo* aortic wall mechanics, which was confirmed by an improved fitting with experimental data [211, 212]. However, no radial tensile stresses were observed in the idealized dissection model, which implies that radial collagen fibers will not contribute to the overall stress state as they are not recruited. An asymmetric dispersion model will, hence,

only differ from the implemented model in its increased amount of fibers close to or in the local axial-circumferential plane. While this deviation might affect the absolute wall stress and deformation, as indicated by Niestrawska et al., the overall material behavior remains similar, which suggests a limited impact on the uncertainty [213]. Moreover, the properties of healthy aortic wall tissue were used as a starting point. Consequently, the developed framework is assumed to represent an acute type B aortic dissection. Indeed, to model a chronic type B aortic dissection, growth and remodeling should be applied to represent the stiffening of the membrane after dissection [44]. In this respect, the quantified uncertainty and the parameter-specific importance is only valid in the situation of an acute dissection. Indeed, the addition of growth and remodeling might result in a different impact of the considered thickness and stiffness parameters on the long-term deformation and stress of the dissected wall.

Moreover, the cause of dissection might be related to altered wall properties. Indeed, type B dissections are associated with degradation in the medial layer which is, amongst others, characterized by fragmented elastic fibers, a reduced elastin fraction and the accumulation of glycosaminoglycans in pools [6, 214]. Therefore, it is possible that the included state-of-the-art material model, with integration of the anisotropic behavior and constituent-specific deposition stretches, is not fully representative for the dissected wall tissue. However, Rolf-Pissarczyk et al. implemented a constitutive law to include the radial elastic fiber degradation in between the medial elastic lamellae, but did not see a clear effect of the adapted material model in their model of the dissected wall [147]. Nevertheless, adaptations in circumferential and longitudinal stiffness and strength as well as changes in collagen content of the acute dissected wall, compared to non-dissected aortic walls, have been observed [9, 38–40, 215]. These effects were not considered by Rolf-Pissarczyk et al. and might affect the resulting wall stress and deformation of the model [147]. As the considered material parameter combinations cover a large range of pulse wave velocities in health and disease, the impact of these differences between the material of the dissected and healthy aortic wall on the quantified uncertainty is expected to remain limited.

7.5 CONCLUSION

In summary, a robust idealized dissected wall framework was developed that included an anisotropic hyperelastic material behavior as well as deposition stretches. It enabled the prediction of the acute

wall deformation in a physiology-inspired manner. With this framework, the effect of uncertainty related to wall thickness and stiffness parameters on the wall deformation and stress was assessed. Large ranges of potential wall deformations and stresses were identified by the global uncertainty analysis, in particular when including the extreme outcomes, which might strongly affect the clinical decision. The analysis of the parameter-specific contribution to the uncertainty suggested that the modeled material stiffness strongly affects the dissected wall deformation, while the relative dissected membrane thickness was the most important determinant for the wall stress. The large uncertainty ranges and the varying impact of, often unknown, wall stiffness and thickness parameters emphasize the need for caution when interpreting the outcome of dissected wall models. Moreover, it supports the use of probabilistic rather than deterministic predictions for clinical decision making in aortic dissections.

7.6 APPENDIX A: EXAMPLES OF MAXIMAL PRINCIPAL STRESS PATTERNS

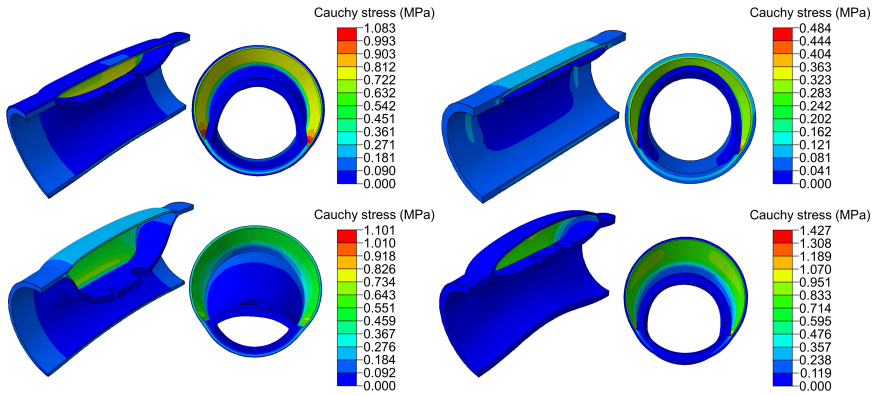


Figure 7.8: Overview of the maximal principal wall stress on the deformed configuration at diastolic pressure (80 mmHg) for four examples of the LHS₃₀₀, i.e. those corresponding to the first row of figure 7.4. For each example, an axial and a cross-sectional cut is shown, together with the corresponding color scale.

7.7 APPENDIX B: RMSE OF GAUSSIAN PROCESSES

LHS₃₀ and LHS₃₀^{control}

Table 7.4: Overview of the RMSE of the trained Gaussian process per output parameter at diastolic (80 mmHg) and systolic (120 mmHg) pressure based on the test set LHS₃₀ and the control test set LHS₃₀^{control}. The RMSE are presented as absolute values as well as relative to the median LHS₃₀₀ value.

RMSE	LHS ₃₀	LHS ₃₀ ^{control}
Diastole		
$U_{DM,max}$ (mm)	0.94 (16%)	0.71 (12%)
$U_{RW,max}$ (mm)	0.73 (33%)	0.83 (38%)
ΔU_{max} (mm)	0.77 (10%)	0.60 (8%)
$MPS_{RW,max}$ (MPa)	0.075 (29%)	0.032 (12%)
Systole		
$U_{DM,max}$ (mm)	1.43 (22%)	0.83 (13%)
$U_{RW,max}$ (mm)	1.26 (48%)	0.96 (36%)
ΔU_{max} (mm)	0.88 (10%)	0.74 (9%)
$MPS_{RW,max}$ (MPa)	0.120 (30%)	0.054 (14%)

Gaussian processes with different number of input parameters

Table 7.5: Overview of the RMSE of the Gaussian process based on four (GP₄, i.e. based on the four independent input thickness and stiffness parameters T_{TW} , T_M , T_{DM} and PWV_{ref} only), 10 (GP₁₀, i.e. with exclusion of g_{circ}^e as input parameter) and 11 (GP₁₁, i.e. the Gaussian process used in the study) input parameters at diastolic (80 mmHg) and systolic (120 mmHg) pressure. The RMSE are presented as absolute values as well as with respect to the median LHS₃₀₀ value.

RMSE	GP ₄	GP ₁₀	GP ₁₁
Diastole			
$U_{DM,max}$ (mm)	3.65 (61%)	1.54 (26%)	0.94 (16%)
$U_{RW,max}$ (mm)	2.08 (95%)	0.72 (33%)	0.73 (33%)
ΔU_{max} (mm)	4.05 (52%)	1.50 (19%)	0.77 (10%)
$MPS_{RW,max}$ (MPa)	0.188 (73%)	0.089 (34%)	0.075 (29%)
Systole			
$U_{DM,max}$ (mm)	3.69 (57%)	2.19 (34%)	1.43 (22%)
$U_{RW,max}$ (mm)	3.23 (122%)	0.99 (37%)	1.26 (48%)
ΔU_{max} (mm)	3.91 (45%)	1.65 (19%)	0.88 (10%)
$MPS_{RW,max}$	0.210 (53%)	0.127 (32%)	0.120 (30%)

7.8 APPENDIX C: COMPARISON OF DELTA INDICES

Comparison of delta indices of LHS₃₀₀ and LHS_{10,000}**Table 7.6:** Overview of δ indices and the corresponding 95% confidence interval (δ_{conf}) as a result of the δ moment-independent analysis for output parameters $U_{DM,max}$, $U_{RW,max}$, ΔU_{max} and $MPS_{RW,max}$ based on the results of LHS₃₀₀ and the central 95% of the output of LHS_{10,000} at diastolic (80 mmHg) and systolic (120 mmHg) pressure.

Input parameter		$U_{DM,max}$		$U_{RW,max}$		ΔU_{max}		$MPS_{RW,max}$	
		δ	δ_{conf}	δ	δ_{conf}	δ	δ_{conf}	δ	δ_{conf}
Diastole									
T_{TW}	LHS ₃₀₀	0.085	0.037	0.028	0.028	0.076	0.039	0.099	0.041
	LHS _{10,000}	0.107	0.006	0.057	0.007	0.109	0.007	0.101	0.008
T_{DM}	LHS ₃₀₀	0.044	0.033	0.091	0.041	0.045	0.034	0.198	0.060
	LHS _{10,000}	0.033	0.005	0.084	0.008	0.039	0.006	0.278	0.008
T_M	LHS ₃₀₀	0.021	0.030	0.039	0.032	0.009	0.027	0.071	0.031
	LHS _{10,000}	0.029	0.005	0.034	0.005	0.026	0.005	0.033	0.005
PWV_{ref}	LHS ₃₀₀	0.045	0.032	0.131	0.047	0.075	0.042	0.132	0.033
	LHS _{10,000}	0.150	0.009	0.209	0.010	0.173	0.011	0.106	0.008
Systole									
T_{TW}	LHS ₃₀₀	0.091	0.037	0.039	0.025	0.080	0.040	0.099	0.036
	LHS _{10,000}	0.106	0.007	0.046	0.005	0.102	0.007	0.103	0.007
T_{DM}	LHS ₃₀₀	0.051	0.034	0.077	0.040	0.050	0.037	0.224	0.053
	LHS _{10,000}	0.034	0.006	0.062	0.007	0.035	0.007	0.303	0.009
T_M	LHS ₃₀₀	0.025	0.029	0.053	0.027	0.010	0.029	0.063	0.033
	LHS _{10,000}	0.029	0.005	0.034	0.005	0.024	0.005	0.028	0.005
PWV_{ref}	LHS ₃₀₀	0.040	0.033	0.117	0.036	0.093	0.042	0.117	0.031
	LHS _{10,000}	0.159	0.010	0.242	0.011	0.195	0.012	0.095	0.008

Comparison of delta indices of LHS_{10,000} and a resampling

Table 7.7: Overview of δ indices and the corresponding 95% confidence interval as a result of the δ moment-independent analysis for output parameters $U_{DM,max}$, $U_{RW,max}$, ΔU_{max} and $MPS_{RW,max}$ based on the results of the central 95% of the output of LHS_{10,000} and a resampling of the same LHS_{10,000} with the same Gaussian process, indicated as LHS_{10,000}^{resample}, at diastolic (80 mmHg) and systolic (120 mmHg) pressure.

Input parameter		$U_{DM,max}$		$U_{RW,max}$		ΔU_{max}		$MPS_{RW,max}$	
		δ	δ_{conf}	δ	δ_{conf}	δ	δ_{conf}	δ	δ_{conf}
Diastole									
T_{TW}	LHS _{10,000} ^{resample}	0.096	0.007	0.067	0.007	0.111	0.006	0.096	0.006
	LHS _{10,000}	0.107	0.006	0.057	0.007	0.109	0.007	0.101	0.008
T_{DM}	LHS _{10,000} ^{resample}	0.034	0.006	0.084	0.008	0.040	0.006	0.305	0.008
	LHS _{10,000}	0.033	0.005	0.084	0.008	0.039	0.006	0.278	0.008
T_M	LHS _{10,000} ^{resample}	0.032	0.005	0.034	0.005	0.025	0.005	0.036	0.005
	LHS _{10,000}	0.029	0.005	0.034	0.005	0.026	0.005	0.033	0.005
PWV_{ref}	LHS _{10,000} ^{resample}	0.152	0.009	0.214	0.009	0.166	0.010	0.105	0.008
	LHS _{10,000}	0.150	0.009	0.209	0.010	0.173	0.011	0.106	0.008
Systole									
T_{TW}	LHS _{10,000} ^{resample}	0.100	0.007	0.046	0.005	0.119	0.007	0.101	0.008
	LHS _{10,000}	0.106	0.007	0.046	0.005	0.102	0.007	0.103	0.007
T_{DM}	LHS _{10,000} ^{resample}	0.036	0.005	0.054	0.006	0.034	0.005	0.299	0.009
	LHS _{10,000}	0.034	0.006	0.062	0.007	0.035	0.007	0.303	0.009
T_M	LHS _{10,000} ^{resample}	0.032	0.006	0.038	0.005	0.027	0.006	0.035	0.005
	LHS _{10,000}	0.029	0.005	0.034	0.005	0.024	0.005	0.028	0.005
PWV_{ref}	LHS _{10,000} ^{resample}	0.157	0.010	0.234	0.012	0.183	0.009	0.094	0.008
	LHS _{10,000}	0.159	0.010	0.242	0.011	0.195	0.012	0.095	0.008

7.9 APPENDIX D: IMPACT OF DIRECT COUPLING BETWEEN THE PWV_{ref} AND GOH PARAMETERS

Methods

In chapter 6, it was found that the PWV can guide the selection of GOH parameters, but does not provide a direct relation [171]. In the current framework, this direct link was, nevertheless, assumed in order to facilitate the use of the Latin hypercube sampling. To consider the effect of this assumption, the reference geometry (section 7.2.1.3) was simulated with the 10 GOH parameter combinations that most closely corresponded to a PWV_{ref} of 5.00 m/s. The median difference, with respect to the results that would be obtained with the idealized dissected wall framework, was determined. Note that one of the 10 analyses, by definition, corresponded to the result of the presented framework. The uncertainty induced by coupling the PWV to other GOH parameter combinations was assessed as the resulting min-max range.

Results

The 10 samples with the PWV_{ref} closest to 5.00 m/s maximally deviated 0.0017 m/s from this target. While the median difference of $MPS_{RW,max}$ shows a maximal decrease in magnitude of 0.005 MPa, median increases in magnitude up to 4.97 mm, with respect to the initial framework, are obtained for the displacement output parameters (table 7.8). The width of the resulting min-max ranges was close to 50% of the min-max interval of the LHS_{300} for the displacement parameters. Smaller min-max intervals are found for $MPS_{RW,max}$, with the maximal width being 14% of the corresponding LHS_{300} min-max interval.

Discussion

The width of the intervals ranged up to 53%, i.e. for $U_{DM,max}$, relative to the min-max range of LHS_{300} , which is remarkable as constant thickness parameters and a nearly constant PWV_{ref} , with a maximal deviation of 0.0017 m/s, are assumed. This reveals a significant uncertainty in the use of PWV_{ref} as material parameter, superimposed on the uncertainty of not knowing the true PWV_{ref} .

Table 7.8: The effect of altering the coupling between the GOH parameters and PWV_{ref} in 10 configurations at diastolic (80 mmHg) and systolic (120 mmHg) pressure. The median value of the difference between $U_{DM,max}$, $U_{RW,max}$, ΔU_{max} and $MPS_{RW,max}$ in the adapted and the original idealized dissected wall framework, is presented, with positive values indicating an increase in displacement or stress magnitude compared to the original idealized dissected wall framework. The width of the min-max range obtained based on the 10 configurations is expressed with respect to the total LHS_{300} min-max width.

Output	GOH- PWV_{ref} coupling	
	Median difference	Min-max width (%)
	Diastole	
$U_{DM,max}(mm)$	1.85	47
$U_{RW,max}(mm)$	2.41	44
$\Delta U_{max}(mm)$	4.61	52
$MPS_{RW,max}(MPa)$	-0.002	11
	Systole	
$U_{DM,max}(mm)$	1.85	51
$U_{RW,max}(mm)$	2.03	45
$\Delta U_{max}(mm)$	4.97	53
$MPS_{RW,max}(MPa)$	-0.005	14

Growth and remodeling of the dissected membrane in an idealized dissected aorta

Clinical observations indicate that the diameter and wall thickness of the dissected aortic wall evolve during its transition from the acute to chronic phase. While growth and remodeling of the aortic wall is increasingly investigated, the knowledge regarding the required parameters remains limited and the transition of the dissected wall from the acute to chronic phase has not yet been considered. Therefore, this chapter assesses the feasibility to reproduce the clinical observations regarding this transition based on the current, limited, knowledge of the growth and remodeling parameters.

This chapter is based on the paper "*Growth and remodeling of the dissected membrane in an idealized dissected aorta model*", published in *Biomechanics and Modeling in Mechanobiology* [216].

8.1 INTRODUCTION

Similar to the healthy aorta, the dissected aortic wall evolves over time as a consequence of soft tissue growth and remodeling. This typically leads to aortic expansion as well as thickening and a reduced motion of the dissected membrane, i.e. the delaminated part of the aortic wall that separates the true lumen (normal blood path)

from the false lumen (newly formed blood path) between the delaminated and the remaining part of the wall [44, 92, 132]. Moreover, inflammation has been observed in the region of the dissection, which is expected to affect the soft tissue growth and remodeling [55–57]. Understanding the impact of growth and remodeling in the context of aortic dissections might contribute to treatment optimization. Indeed, both medically and endovascularly treated patients regularly show the development of complications, such as aortic expansion and malperfusion, and/or the need for late (re)interventions [2, 4]. This indicates that the current treatment strategies are often not able to determine the optimal patient-specific treatment at hospital admission. Moreover, the timing of the intervention has been found to impact the long-term outcome of the treatment in terms of maximal aortic diameter, false lumen size and true lumen expansion [94]. In combination with accurate models of the blood flow and thrombus formation, the inclusion of growth and remodeling in models of aortic dissection will help in the prediction of potential complications and/or the preferred timing of stent-graft placement.

Multiple theoretical frameworks to represent soft tissue growth and remodeling, such as the (homogenized) constrained mixture theory, have been proposed over the past decades and applied to arterial diseases as hypertension and aneurysm formation, where the growth and remodeling process was explained as a consequence of elastin degradation and collagen remodeling induced by changes in stress and/or inflammation [137, 148–154]. Furthermore, a multi-scale framework was developed and used to model the effect of the microstructural constituent remodeling on the macroscopic soft tissue deformation in a chronic dissection [158].

However, these growth and remodeling models come with a large set of parameters and knowledge regarding proper physiological values thereof is still limited. In case longitudinal experimental data is available, values for the considered parameters can be determined through parameter fitting [148]. However, often insufficient or even no data is available and parameter values have to be assumed. In this respect, the impact of adopted parameter values for the stress-induced growth and remodeling has been tested, but not in the framework of aortic dissections [137, 149, 150, 153, 154, 217]. Indeed, the transition from the acute to the chronic phase in the dissected aorta has, to the authors' knowledge, not yet been modeled and proper parameter values have, consequently, not yet been established.

Therefore, this study aims to investigate whether the transition of the dissected aorta from the acute to the chronic phase, and the

corresponding dissected membrane thickening, can be represented by applying stress- and inflammation-mediated growth and remodeling of elastin and collagen using reported ranges for the growth and remodeling parameters.

8.2 METHODS

8.2.1 Model framework

8.2.1.1 Geometry

The reference geometry is based on an idealized model of a slice of a dissected aorta (comparable to chapter 7; appendix A, section 8.6). The dissected wall model was developed as a cylindrical geometry with an axial length of 5.00 mm, an inner diameter of 27.30 mm and a total wall thickness of 1.90 mm (figure 8.1) [197]. Of the total wall thickness, a fraction of 75% was assumed to correspond to the media and 25% to the adventitia [6, 8]. The false lumen is implemented in the cylindrical reference geometry by integrating unconnected elements at 70% of the medial layer, thus in the outer third of the media, and comprises 245° of the circumference, a value retrieved from a patient computed tomography (CT) scan and in correspondence to Brunet et al. [54, 62]. The CT scan was acquired from the University Hospital of Düsseldorf with consent of the local ethical committee (reference number: 2017064325) [198]. In its unloaded state, the false lumen is not visible and the model appears as the geometry of a healthy cylindrical aortic wall (figure 8.1(a, c)). The model does not include the tears or connection with the healthy aortic wall and, therefore, represents an infinitely long dissection.

8.2.1.2 Acute material behavior

Both the medial and the adventitial layer of the dissected wall model are assumed to behave as an incompressible anisotropic hyperelastic Holzapfel-Gasser-Ogden (HGO) material with two non-dispersed fiber families [95]. The strain energy density functions for the elastin and collagen fraction of each layer, Ψ_M^e , Ψ_M^c , Ψ_A^e and Ψ_A^c , were, consequently, defined as

$$\begin{aligned} \Psi_M^e &= \frac{c_{10M}}{\rho_{0M}^e} (I_1^e - 3); \quad \Psi_M^c = \frac{k_{1M}}{\rho_{0M}^c} \frac{1}{2k_2} \left(\sum_{j=4,6} e^{k_2(I_{jM}^c - 1)^2} - 1 \right) \\ \Psi_A^e &= \frac{c_{10A}}{\rho_{0A}^e} (I_1^e - 3); \quad \Psi_A^c = \frac{k_{1A}}{\rho_{0A}^c} \frac{1}{2k_2} \left(\sum_{j=4,6} e^{k_2(I_{jA}^c - 1)^2} - 1 \right) \end{aligned} \quad (8.1)$$

$$\text{with } c_{10A} = 0.34c_{10M} \text{ and } k_{1A} = 1.17k_{1M}$$

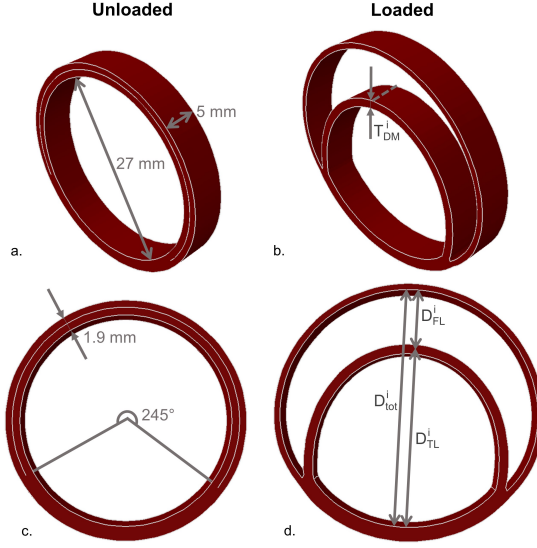


Figure 8.1: Overview of the slice model in the (a, c) unloaded and (b, d) loaded configuration. The predefined dimensions of the model are indicated on the (a, c) unloaded shape, which corresponds to the geometry of the *in vivo* healthy wall, but already includes the predefined location of the false lumen. A schematic indication of the measured geometrical parameters is illustrated on the (b, d) loaded configuration, with T_{DM}^i being the dissected membrane thickness and D_{tot}^i , D_{FL}^i and D_{TL}^i referring to the respective total, false lumen and true lumen diameter, where day i indicates the day of interest in the growth and remodeling process. Note that D_{tot}^i , D_{FL}^i and D_{TL}^i are measured at the same line, but are indicated next to each other for better visualization.

where subscripts M and A , respectively, indicate the medial and adventitial layer and superscripts e and c refer to elastin and collagen, respectively. Parameters c_{10} , k_1 and k_2 correspond to the elastin shear modulus, the collagen stiffness and the collagen fiber stiffening, respectively. Parameters c_{10} and k_1 were linked for the media and adventitia based on the observed elastin and collagen area fractions in both layers [12]. The invariants of the right Cauchy-Green tensor \mathbf{C}^i of constituent deformation gradient tensor \mathbf{F}^i , with $\mathbf{C}^i = \mathbf{F}^{iT} \mathbf{F}^i$, are indicated as I_1^i and I_j^i , with $j = 4, 6$. The fourth and sixth invariants, I_4^c and I_6^c , depend on fiber stretch and the mean fiber angles α_M and α_A , which are defined with respect to the circumferential direction and differ for the media and adventitia. Note that the fibers are assumed to contribute to the load bearing in tensile stretch only. The initial density of constituent i , expressed as fraction with respect to the initial configuration, is accounted for by ρ_0^i . Including this

density allows the expression of the fraction of collagen and elastin with respect to a reference unit area within each material layer, which is assumed to contain no other constituents than collagen and elastin.

The parameters were determined based on a predefined value of the pulse wave velocity (PWV) as proposed in chapter 6, where the PWV of a full factorial design of the Gasser-Ogden-Holzapfel (GOH) parameters, including collagen fiber dispersion, was calculated for a reference cylinder [171]. A PWV of 6.00 m/s was assumed, which is representative for the aortic stiffness in middle-aged humans and, thus, corresponds to the average age of dissection patients [198]. As a non-dispersed one-dimensional fiber orientation was assumed in the growth and remodeling implementation (section 8.2.2.1), the GOH parameter combination that fulfilled the zero-dispersion condition, both in the media and adventitia, and was closest to the target PWV of 6.00 m/s was selected. This resulted in parameters $c_{10M} = 0.015$ MPa, $k_{1M} = 0.119$ MPa, $k_{2M} = 6.9$, $\alpha_M = 45.0^\circ$ for the media and $c_{10A} = 0.005$ MPa, $k_{1A} = 0.139$ MPa, $k_{2M} = 6.9$, $\alpha_A = 78.8^\circ$ for the adventitia. The aortic wall tissue was assumed to be composed of elastin and collagen, smooth muscle cells were not accounted for. Consequently, the initial fractions of collagen and elastin were determined as percentage of the total elastin and collagen area, based on the data of Iliopoulos et al. [12]. This resulted in a respective initial collagen fraction for the media and adventitia of 0.27 and 0.40, for each fiber family. The corresponding initial elastin fractions were 0.46 for the medial and 0.20 for the adventitial layer.

8.2.1.3 Loading and boundary conditions

To account for the *in vivo* loading state of the aortic wall, an axial stretch as well as circumferential and radial deposition stretches have been included using a Matlab (The MathWorks Inc., USA) implementation of the deposition stretch algorithm of Famaey et al. [126]. This pre-stressing algorithm was first applied to a healthy cylindrical geometry, without false lumen, with a constant deposition strain of 10% in the fiber direction for collagen and in the axial direction for elastin [103, 113]. The *in vivo* deformation of the acute dissection was subsequently obtained by applying the resulting deposition stretches, obtained from the deposition stretch algorithm in Matlab, simultaneous with a diastolic pressure of 80 mmHg to the true and false lumen to a finite element model, with 3,000 hybrid hexahedral elements, in Abaqus/Standard (Dassault Systèmes, France). The healthy configuration was not explicitly determined in the finite element analysis. Note that no load was applied to the dissected membrane, due to

the assumption that the pressure exerted by the true and false lumen compensate each other. The slight difference in surface on which the pressure is acting indicates that the applied loading conditions provide an approximation of the *in vivo* situation. At the proximal and distal boundaries, only radial expansion was allowed for the adventitial layer and the connected medial layer, while the circumferential direction was an additional degree of freedom for the dissected membrane. This procedure leads to a dissected wall, shown in figure 8.1(b, d), that embeds initial stresses in the (remaining) aortic wall, while stress is relieved in the dissected membrane as the delamination takes place and the diastolic pressure is applied.

8.2.2 Transition from acute to chronic dissection

While the medical consensus on the definition of the acute, subacute and chronic phase of the dissection is, respectively, 0 to 14 days, 2 weeks to 3 months and more than 3 months after onset of the symptoms, a different definition was adopted for the experimental data of Peterss et al., where the dissected membrane thickening from the acute to the chronic phase was assessed [24, 44]. Indeed, they considered the membrane thickening after 2 to 6 weeks as subacute and after 6 weeks as chronic. In order to allow for a comparison with the experimental data, the definition of Peterss et al. was adopted here [44]. In total, 30 growth steps were implemented, each accounting for a time step of 3 days, thus considering growth and remodeling during 90 days.

8.2.2.1 Homogenized constrained mixture theory

The evolution of the dissected wall during the transition from an acute to a chronic dissection was modeled using an implementation of the homogenized constrained mixture algorithm in Abaqus/Standard. While the details of the theory, developed by Cyron et al., and the implementation, proposed by Maes et al. and Maes and Famaey, have been extensively described before, the most important aspects are summarized below [135, 136, 148].

In the homogenized constrained mixture theory, the total deformation gradient tensor at time s , $\mathbf{F}(s)$, is the result of the soft tissue growth \mathbf{F}_g and the constituent-specific remodeling \mathbf{F}_r^i and elastic deformation \mathbf{F}_{elas}^i according to

$$\mathbf{F}(s) = \mathbf{F}_{elas}^i(s)\mathbf{F}_r^i(s)\mathbf{F}_g(s) \quad (8.2)$$

with i indicating the considered constituent and $i = e, c$ corresponding to elastin and collagen, respectively. Consequently, the elastic

deformation gradient tensor \mathbf{F}_{elas}^i is determined if the total deformation, which can be determined using a finite element model, and the deformation due to growth and remodeling is known. The soft tissue growth is assumed to occur in the radial direction and to affect the different constituents in the same manner. Therefore, the soft tissue growth at time s , $\mathbf{F}_g(s)$, was implemented as

$$\mathbf{F}_g(s) = \frac{\rho^{tot}(s)}{\rho^{tot}(0)} \mathbf{a}_g \otimes \mathbf{a}_g + (\mathbf{I} - \mathbf{a}_g \otimes \mathbf{a}_g), \quad (8.3)$$

where \mathbf{a}_g is a unit vector that indicates the main growth direction, ρ^{tot} the total density of elastin and collagen together and \mathbf{I} the identity matrix [136, 137].

As it is assumed that elastin does not remodel, the deformation imposed by the remodeling only depends on the collagen and can be extracted from

$$\mathbf{F}_r^c(s) = \lambda_r^{c,f}(s) \mathbf{M}^f \otimes \mathbf{M}^f + \frac{1}{\sqrt{\lambda_r^{c,f}(s)}} (\mathbf{I} - \mathbf{M}^f \otimes \mathbf{M}^f), \quad (8.4)$$

for one-dimensional collagen fibers [135–137]. The mean collagen fiber direction in the initial configuration is indicated by \mathbf{M}^f , while $\lambda_r^{c,f}(s)$ represents the collagen remodeling stretch in the fiber direction of fiber family f at time s . For more details about the derivation of this equation, the reader is referred to the original papers [135–137].

The densities of collagen and elastin change over time due to the constituent degradation and, in case of collagen, production. Therefore, the current change in density of constituent i at time s , $\dot{\rho}^i(s)$, is determined as

$$\dot{\rho}^i(s) = \dot{\rho}_+^i(s) + \dot{\rho}_-^i(s), \quad (8.5)$$

where $\dot{\rho}_+^i(s)$ and $\dot{\rho}_-^i(s)$ represent the respective production and degradation rate of constituent i at time s . Note that the densities, and the corresponding changes, are expressed relative to the initial configuration.

The total strain energy density function Ψ^{tot} is calculated as a combination of the strain energy density function of the different constituents and their corresponding densities. Moreover, it is assumed that the strain energy only depends on the elastic part of the deformation. This results in

$$\Psi_j^{tot}(s) = \sum_i \rho_j^i(s) \Psi_j^i(\mathbf{F}_{elas}^i(s)) \quad (8.6)$$

where $j = M, A$ depending on whether the medial or adventitial layer is considered (section 8.2.1.2).

8.2.2.2 Stress-mediated growth and remodeling

As the aortic wall attempts to restore homeostasis, collagen is remodeled by sensing the difference between the current and the homeostatic stress state [134]. It is assumed that this stress-mediated growth and remodeling is present, both in health and disease, and, consequently, in the framework of aortic dissections. Therefore, the collagen production depends on the difference between the homeostatic and the current stress in the direction of fiber family f , $\sigma_h^{c,f}$ and $\sigma^{c,f}(s)$ respectively, and the gain factor k_σ^c . The homeostatic fiber stress, $\sigma_h^{c,f}$, is determined as the stress that corresponds to the imposed homeostatic collagen fiber deposition strain of 10%. The degradation rate is, on the contrary, assumed to be constant and to depend on the characteristic time of collagen T^c , which was taken as 101 days [137, 148]. This results in

$$\dot{\rho}_+^{c,f}(s) = \frac{\rho^{c,f}(s)}{T^c} \left(1 + k_\sigma^c \frac{\sigma^{c,f}(s) - \sigma_h^{c,f}}{\sigma_h^{c,f}} \right) \quad (8.7)$$

$$\dot{\rho}_-^{c,f}(s) = -\frac{\rho^{c,f}(s)}{T^c}. \quad (8.8)$$

This stress-mediated growth and remodeling, thus, retains the homeostatic configuration for a healthy aortic wall, which is indicated in appendix B (section 8.7).

8.2.2.3 Inflammation-mediated growth and remodeling

As inflammatory cells have been observed in the dissected region, inflammation might be involved in the process of the dissected membrane thickening [55–57]. In total, four inflammation patterns were considered based on the duration and location of the inflammation. As indications have been found for a transient and permanent effect of inflammation on the dissected membrane [35, 44], a transient and permanent inflammation process was studied similar to Maes et al. and Drews et al. [148, 218]. The transient inflammatory reaction (figure 8.2(a)), as a consequence of the dissection of the aortic wall, was defined as

$$\Gamma_t(s) = \left(\frac{\delta s}{\beta - 1} \right)^{\beta-1} e^{-\delta s + \beta - 1}, \quad (8.9)$$

with δ and β being shape parameters that determine the location and extent of the inflammation peak and s being the time expressed in days. The second pattern implies a permanent inflammatory reaction triggered by the dissection, which is in correspondence to the observations of Peterss et al., where no significant change in degree of inflammation of the dissected membrane was found between the acute and chronic phase (figure 8.2(a)) [44]. The permanent inflammation function is described as

$$\Gamma_p(s) = 1 - e^{-\delta s}, \quad (8.10)$$

with δ being the shape parameter that defines how fast the inflammatory process arises after occurrence of the dissection and s being again the time expressed in days.

Next to parameters δ and β , three gain factors were defined which impose the extent to which the inflammation-mediated growth and remodeling of collagen and elastin takes place. Indeed, $k_{\Gamma+}^c$, $k_{\Gamma-}^c$ and $k_{\Gamma-}^e$, respectively, represent the extent of the collagen production, collagen degradation and elastin degradation as a consequence of the inflammatory reactions. Adding the effect of this inflammation to the stress-mediated growth and remodeling (equations (8.7-8.8)) leads to

$$\dot{\rho}_+^{c,f}(s) = \frac{\rho^{c,f}(s)}{T^c} \left(1 + k_{\Gamma+}^c \Gamma(s) + k_{\sigma}^c \frac{\sigma^{c,f}(s) - \sigma_h^{c,f}}{\sigma_h^{c,f}} \right) \quad (8.11)$$

$$\dot{\rho}_-^{c,f}(s) = -\frac{\rho^{c,f}(s)}{T^c} (1 + k_{\Gamma-}^c \Gamma(s)) \quad (8.12)$$

$$\dot{\rho}_-^e(s) = -\frac{1}{3} \rho^e(s) k_{\Gamma-}^e \Gamma(s) \quad (8.13)$$

Here, Γ can be replaced by Γ_t or Γ_p , depending on the considered inflammation duration. The location of the inflammation was either applied to the full wall, i.e. the complete medial and adventitial layer, or to the media that surrounds the false lumen, i.e. the dissected membrane and the media of the remaining wall, which is referred to as local inflammation (figure 8.2(b)). The regions which are not subjected to inflammation are still affected by the stress-mediated growth and remodeling and equations (8.7) and (8.8), thus, apply.

8.2.2.4 Implications of the growth and remodeling algorithm

The applied homogenized constrained mixture algorithm has been discussed before [148], but it is worth to touch upon some implications of the considered dissected wall growth and remodeling. The

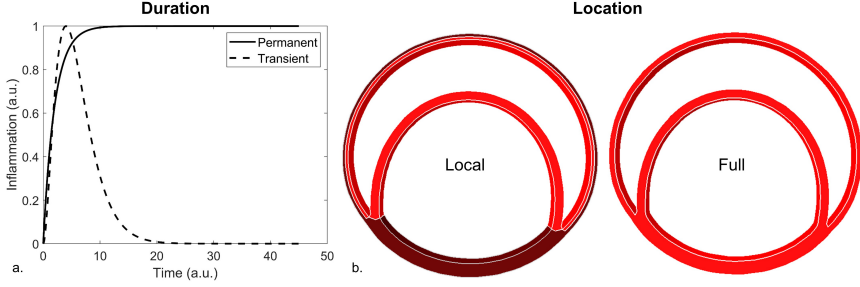


Figure 8.2: Schematic overview of the (a) duration, i.e. permanent or transient, and (b) location, i.e. full or local, of the inflammation patterns. For the (b) location, the area of inflammation is indicated in red.

modeled stress-mediated growth and remodeling depends on the difference between the current and the homeostatic collagen fiber stress, $\sigma^{c,f}(s)$ and $\sigma_h^{c,f}$ respectively, where collagen production is triggered in case of increased fiber stress. This is expected to happen in the remaining wall of the dissected aorta, as a thinner wall has to withstand the same pressure. Conversely, the production of fibers decreases if their stress level is below the homeostatic state, which is the case in the acute dissected membrane, where the delamination corresponds to the release of the stresses in the tissue and, consequently, in the collagen fibers.

Besides, note that the combination of stress- and inflammation-mediated remodeling implies that the collagen fibers remodel, even though their stress state equals the homeostatic one. In this case, the remodeling is triggered by the difference in inflammation-related production, $k_{\Gamma+}^c$, and degradation, $k_{\Gamma-}^c$. The concept that a severe inflammatory response might cause maladaptation and trigger the arterial wall to deviate from its homeostatic state was introduced by Latorre and Humphrey, where it was applied in a constrained mixture model in the framework of hypertension [219].

8.2.3 Parametric study of growth and remodeling parameters

8.2.3.1 Input parameters and sampling

As no clear parameter values for the stress- and inflammation-mediated growth and remodeling parameters (k_{σ}^c , $k_{\Gamma+}^c$, $k_{\Gamma-}^c$, $k_{\Gamma-}^e$, δ and β for transient inflammation and k_{σ}^c , $k_{\Gamma+}^c$, $k_{\Gamma-}^c$, $k_{\Gamma-}^e$ and δ for permanent inflammation) have been established in the framework of aortic dissections, previously reported values were used to

define ranges with potential parameters (table 8.1) [137, 148–150, 153]. The resulting parameter space was sampled using a Latin hypercube with 1,000 samples. Due to the different dimensions of the transient and permanent inflammation pattern, as a consequence of a difference in number of parameters, a different Latin hypercube sampling was required for both cases. The same Latin hypercube was, however, used for the local and full inflammation pattern. For all input parameters, a uniform probability distribution was assumed. For each Latin hypercube sample, a finite element analysis was performed and the success rate was assessed for the four inflammation patterns. Moreover, the range of the individual growth and remodeling parameters that resulted in a converged solution was determined.

8.2.3.2 Output parameters

In correspondence to the definition of the acute, subacute and chronic dissection phase of Peterss et al., the thickness of the dissected membrane was considered at 0, 15, 42 and 90 days [44]. Note that the subacute phase is commonly defined to start after 14 days, but that day 15 is considered since a time step of 3 days was chosen [24, 44]. The thickness was determined by extracting the coordinates of the circumferentially central nodes at the true and false lumen side of the dissected membrane, throughout the axial direction, for each of the considered time points (figure 8.1(b)). Consequently, the thickening rates corresponding to the three phases were determined in case of 30 converged growth and remodeling time steps in the finite element analysis. The thickening rates, R_T , of the dissected membrane were

Table 8.1: Overview of the applied parameter ranges for the Latin hypercube sampling of the transient and permanent inflammation pattern, based on published data on parameters used in the homogenized constrained mixture theory. The minimal (min) and maximal (max) values of the published ranges are reported [137, 148, 150, 153].

Parameter	Transient inflammation [min; max]	Permanent inflammation [min; max]
k_σ^c (-)		[0.000; 0.420]
k_{T+}^c (-)		[1.74; 24.90]
k_{T-}^c (-)		[1.41; 20.70]
k_{T-}^e (step ⁻¹)		[0.0000; 0.0707]
δ (day ⁻¹)	[0.015; 0.478]	[2.77; 17.00]
β (-)	[1.10; 4.64]	NA

calculated as

$$R_T = \frac{T_{DM}^i - T_{DM}^j}{i - j}, \quad (8.14)$$

where T_{DM}^i and T_{DM}^j represent the thickness of the dissected membrane at day i and j (with $i > j$), respectively. Moreover, it was assessed which thickening rates agreed to the ranges as reported in Peterss et al. [44]. To account for the measurement uncertainty in the reported thickening measurements, additional uncertainty was added to the confidence intervals. A CT scan with a pixelsize of 1.00 mm was assumed, which leads to a maximal uncertainty of 2.00 mm per thickness measurement. As the thickening is the result of two thickness measurements, a total uncertainty of 4.00 mm was added to the lower and upper boundary of the reported confidence intervals. This resulted in an extended clinical range of [-3.50; 6.09] mm/year in the acute, [-4.13; 5.09] mm/year in the subacute and [-3.99; 4.03] mm/year in the chronic phase. In this respect, it was assessed which parameter values of the individual growth and remodeling parameters resulted in thickening rates within these extended clinical ranges.

The total diameter expansion of the aorta as a consequence of the dissection was assessed by calculating the cross-sectional distance of the total intraluminal space at day 0, 15, 42 and 90 (figure 8.1(d)). Moreover, the false and true lumen size were measured along this line as the distance between the inner side of the aortic wall and the middle of the dissected membrane. In this way, the sum of the true and false lumen sizes is by definition equal to the total diameter. As clinical data of the diameter expansion is often established based on follow-up data of multiple years, the expansion rate was estimated by extrapolating the diameter expansion using the growth rate in the chronic phase up to a duration of 365 days [92, 220–222]. The diameter expansion rate is, therefore, calculated as the sum of the modeled diameter expansion between day 0 and day 90 and the estimated diameter expansion from day 90 until day 365, by extrapolating the chronic expansion rate. In this way, the expansion rate, R_e^n , is represented in mm/year and expressed as

$$R_e^n = \left(D_n^{90} - D_n^0 \right) + \frac{D_n^{90} - D_n^{42}}{90 - 42} (365 - 90), \quad (8.15)$$

with superscript n referring to the respective total lumen (tot), false lumen (FL) and true lumen (TL) and D_n^i indicating the corresponding diameter at time i , which is indicated in days. The change in

volume of the dissected membrane, i.e. the combined volume of the elastin and collagen, over time was assessed as well.

In order to consider the change in the dissected membrane microstructure, the evolution of the collagen and elastin content, expressed relative to the initial volume, was analyzed at day 15, 42 and 90, similar to the thickening rates. At day 0, the collagen and elastin content corresponds to the predefined fractions as indicated in section 8.2.1.2. The collagen and elastin content was determined as the average of the content of each element of the dissected membrane, weighted by the corresponding volume.

8.3 RESULTS

8.3.1 Parametric study of growth and remodeling parameters

For the full and local permanent inflammation patterns, convergence until the chronic phase (90 days) is reached for only 3 (0.3%) and 1 (0.1%) of the 1,000 samples, respectively. The transient inflammation patterns result in higher success rates of 146 (14.6%) cases for the full and 88 (8.8%) for the local inflammation. Slightly lower success rates are, thus, found for the local compared to the full inflammation, irrespective of the considered duration. Due to the very limited convergence of the permanent inflammation patterns, the reported results are focused on the transient inflammation patterns. Some additional results regarding the permanent inflammation are, nevertheless, shown in appendix C (section 8.8).

An overview of the individual growth and remodeling parameter ranges that lead to convergence for growth and remodeling with transient inflammation over 90 days is given in figure 8.3, for all combinations that resulted in a converged solution and the selection of combinations with thickening rates within the extended clinical range (section 8.3.3). Overall, a larger reduction in parameter ranges is established for the full inflammation, compared to the local one. When combining the relative reduced individual parameter widths that result in convergence over 90 days, the total parameter space is reduced to 75.3% and 75.1% of the initial parameter space for the full and local transient inflammation pattern, respectively. When further refining the parameter space to those parameter ranges that lead to thickening rates within the extended clinical ranges, the parameter space related to the full and local inflammation pattern reduces to 13.2% and 44.9% of the initial space.

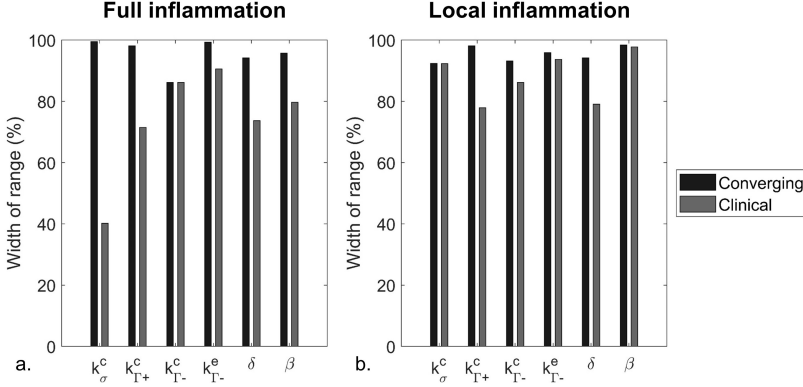


Figure 8.3: Overview of the width of the parameter range of the simulated samples that fulfilled the convergence criteria of the simulation during 90 days of growth and remodeling (converging) and resulted in thickening rates within the extended clinical range (clinical) for the full and the local transient inflammation pattern. The width is expressed as percentage of the initial width of the parameter range.

8.3.2 Example cases

The deformed configurations at day 0, 15, 42 and 90 of four illustrative transient inflammatory example cases are illustrated in figure 8.4 and in appendix D (section 8.9), while the change of their stresses and deformations over time is included as animation in the supplementary material of the online version of the paper [216]. For the example case with transient, local inflammation and thickening rates within the extended clinical range, figure 8.5 and 8.6, respectively, present the change in strain and fiber stress and the change in collagen and elastin content in the dissected wall over time. The corresponding growth and remodeling parameters of this example are $k_{\sigma}^c = 0.130$, $k_{\Gamma+}^c = 5.34$, $k_{\Gamma-}^c = 3.67$, $k_{\Gamma-}^e = 0.0533 \text{ step}^{-1}$, $\delta = 0.19 \text{ day}^{-1}$ and $\beta = 1.24$.

As a consequence of the dissection, the fiber stress in the remaining wall initially increases, to decrease again during the growth and remodeling process. The opposite effect is seen for the dissected membrane. The elastin and collagen content only adjusts once the growth and remodeling process starts. Therefore, figure 8.6 does not include the pre-dissection configuration. The growth and remodeling process induces a sudden decrease in the elastin content between day 0 and day 15 in the portion of the media that is subjected to inflammation. Afterwards, the elastin content remains, approximately, constant. The content of collagen initially decreases in the dissected

membrane, to increase again from day 42 onwards, while an overall increase in collagen content is observed, in the adventitia of the remaining wall.

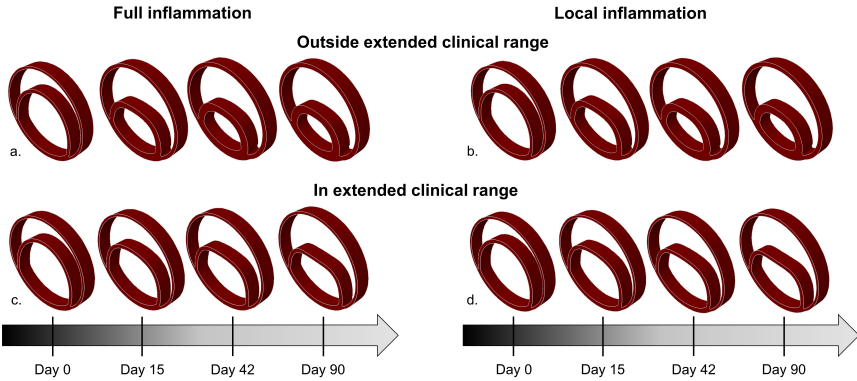


Figure 8.4: Examples of the predicted changes in geometry over time due to the growth and remodeling for samples with transient inflammation that is applied (a, c) over the full geometry and (b, d) locally around the false lumen, which result in thickening rates (a, b) outside and (c, d) within the extended clinical range.

8.3.3 Thickening rates of the dissected membrane

Figure 8.7 shows the dissected membrane thickening over time for the converged samples of the transient inflammatory cases. A decreasing thickening rate over time is found for the local and full transient inflammation pattern, where, respectively, 38 (3.8%) and 24 (2.4%) samples result in rates within the proposed extended clinical ranges for the acute, subacute and chronic phase. An overview of the corresponding growth and remodeling parameters is given in appendix E (section 8.10). In contrast, the converged samples with permanent inflammation indicate an increasing trend in thickening rate over time, for the local as well as the full inflammation pattern (appendix C, section 8.8).

8.3.4 Diameter expansion and volume change

Over the considered 90 days of soft tissue growth and remodeling, the total diameter increases for all parameter combinations within the extended clinical thickening range and a median total diameter expansion rate of 5.09 mm/year and 4.71 mm/year is observed for the full and local inflammation pattern, respectively (table 8.2). The false lumen size increases with a median rate of 19.63 mm/year for full and 19.73 mm/year for local inflammation. The true lumen size, however,

8. GROWTH AND REMODELING OF THE DISSECTED MEMBRANE IN AN IDEALIZED DISSECTED AORTA

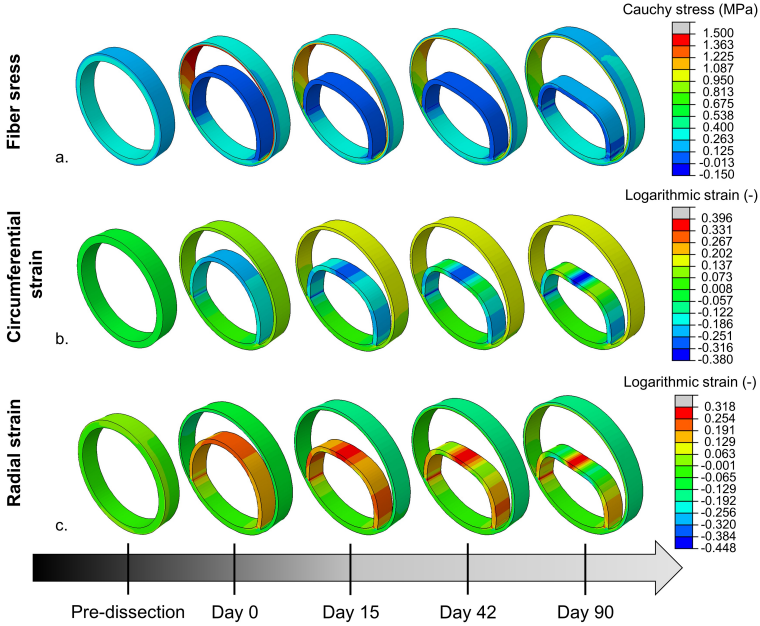


Figure 8.5: Evolution of the (a) fiber stress and (b) circumferential and (c) radial strain over time for an example sample with local and transient inflammation. The stress is expressed as the fiber Cauchy stress, while the circumferential and radial logarithmic strain are indicated to represent the deformation. The fiber stress is illustrated for one fiber family in the medial and one in the adventitial layer, which is representative for the second fiber family too. The radial and circumferential direction is defined according to the pre-dissected configuration.

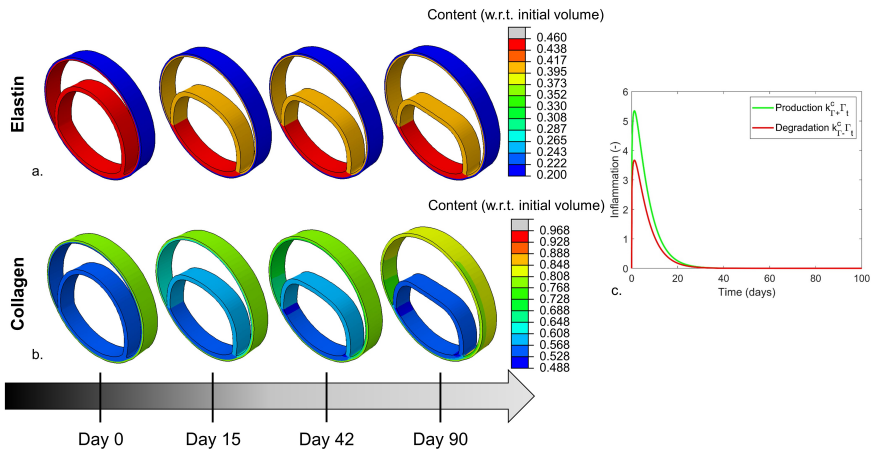


Figure 8.6: Evolution of the (a) elastin and (b) collagen content over time for an example sample with a local and transient inflammation pattern as illustrated in (c). The content is expressed as fraction of the initial volume.

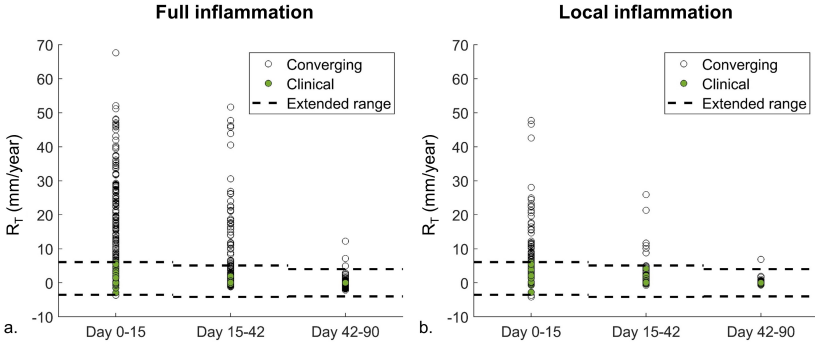


Figure 8.7: Resulting thickening rates, R_T , of the dissected membrane for the (a) full and (b) local transient inflammation pattern, for the acute (Day 0-15), subacute (Day 15-42) and chronic (Day 42-90) phase. The rates corresponding to converging simulations are indicated with black circles. The points corresponding to converged simulations that lead to thickening rates within the extended clinical range are filled in green. The upper and lower boundaries of the extended clinical range for the three phases are shown with a dashed line.

decreases over time at a respective median rate of 14.99 mm/year and 14.83 mm/year for the full and local inflammation pattern. The volume of the dissected membrane at 90 days varies from 83.6% to 106% of the initial volume for the full and from 84.3% to 111% for the local inflammation pattern.

8.3.5 Dissected membrane microstructure

An overview of the elastin and collagen content at day 90 is shown in figure 8.8 for the parameter combinations resulting in thickening rates within the extended clinical ranges. For both inflammation

Table 8.2: Expansion rate of the total diameter (R_e^{tot}), the true lumen (R_e^{TL}) and the false lumen (R_e^{FL}), expressed as mm/year, based on extrapolation of the expansion rate in the chronic phase up to a period of 365 days, for the full and local transient inflammation patterns that resulted in thickening rates within the extended clinical range. The median as well as the minimal (min) and maximal (max) expansion rate are indicated.

Expansion rate	Full inflammation median [min; max]	Local inflammation median [min; max]
R_e^{tot} (mm/year)	5.09 [2.57; 7.69]	4.71 [2.59; 7.76]
R_e^{TL} (mm/year)	-14.99 [-20.76; -13.65]	-14.83 [-21.39; -13.37]
R_e^{FL} (mm/year)	19.63 [16.74; 26.15]	19.73 [16.33; 26.81]

patterns, the amount of elastin remains similar or decreases, which results at day 90 in an elastin content between 28.0% and 45.8% of the initial volume (elastin content at day 0: 46.0%). The trend in collagen content is variable. At day 90, the collagen content of the full inflammation pattern ranges from 42.5 to 63.5% of the initial volume (collagen content at day 0: 54.0%) and the respective minimal and maximal collagen content as result of the local inflammation pattern varies from 39.5% to 76.4% of the initial volume. This indicates that both decreasing and increasing collagen contents are observed.

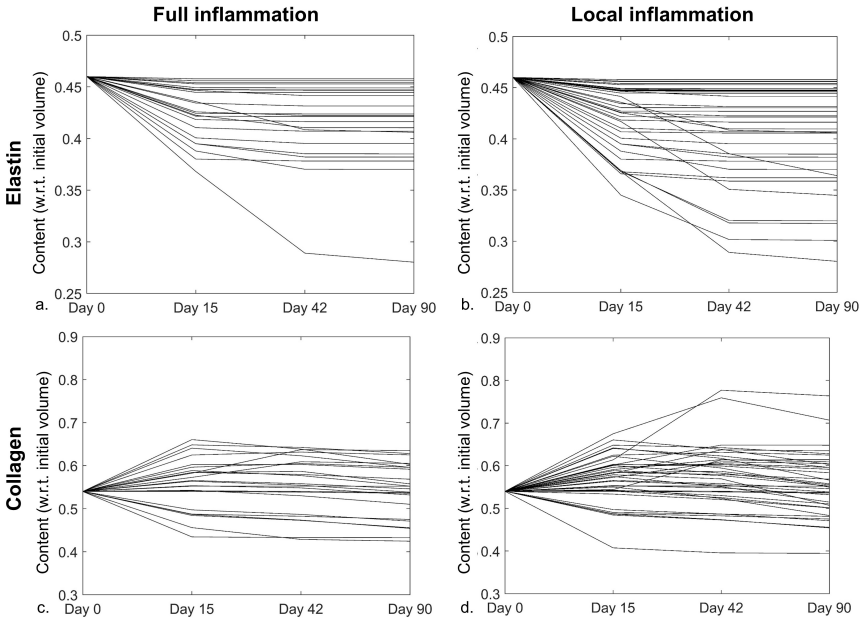


Figure 8.8: Overview of the (a, b) elastin and (c, d) collagen content of the dissected membrane for the (a, c) full and (b, d) local inflammation pattern, for the parameter combinations that lead to thickening rates within the extend clinical range. The content is expressed relative to the initial volume of the dissected membrane.

8.4 DISCUSSION

The current study aims to evaluate whether existing growth and remodeling algorithms, fed with parameters from literature, allow the reproduction of the soft tissue growth and remodeling in aortic dissections, with a particular focus on the thickening and change in microstructure of the dissected membrane. A slice model of an acute dissection with an anisotropic hyperelastic material that accounts for

the deposition stretches was used as starting point and a homogenized constrained mixture model was applied to represent a period of 90 days. The model included collagen production as a consequence of deviations from the homeostatic stress state as well as collagen and elastin degradation and/or production triggered by inflammation. Four inflammatory response patterns were considered, depending on the location and duration of the inflammation.

The overall success rate is limited to 14.6% for the considered inflammation patterns, which indicates that only particular growth and remodeling parameters are compatible. In this respect, the difference between the inflammation-mediated collagen production and degradation is hypothesized to be an important factor as only about 55.0-60.0% of the total $k_{\Gamma+}^c - k_{\Gamma-}^c$ range is able to reach convergence for transient inflammation, which further decreases to 1.8% for permanent inflammation (table 8.1). Introducing a dependency between both parameters in the sampling is expected to enhance the success rate of the model. Furthermore, a clear difference in success rate between transient and permanent inflammation is observed. Indeed, the transient inflammation results in success rates of 8.8% to 14.6%, while a maximal rate of only 0.3% is found for the permanent inflammation. Furthermore, the obtained thickening rates for the few converging samples with permanent inflammation show an increasing trend (appendix C, section 8.8), which would by definition result in increasingly thicker membranes until non-physiological thicknesses would be obtained. This persistent thickening is also hypothesized to be the main reason for the very limited convergence. Consequently, the permanent inflammation pattern is unrealistic and not able to reproduce the clinical observations of dissected membrane thickening. This suggests that transient inflammation, rather than permanent inflammation, takes place after dissection of the aorta. Although Peterss et al. reported no significant difference in the presence of inflammation between dissections in the acute and chronic phase, the transient pattern is in line with the findings of Xu and Burke, who reported that inflammation mainly occurred in the first week after dissection [35, 44].

It is important to highlight that this study is not aimed towards revealing the ground-truth growth and remodeling mechanisms and corresponding parameters in aortic dissections. Rather, this study investigates up to which extent the clinical observations of dissection patients can be reproduced based on the existing soft tissue growth and remodeling knowledge. As such, the ability to reproduce clinical trends does not necessarily imply that the model captures the

physiological reality. It only supports the assumptions that transient inflammation potentially plays an essential role in the soft tissue growth and remodeling of aortic dissections.

The resulting median total diameter expansion rates are 5.09 mm/year and 4.71 mm/year, respectively, for the full and local transient inflammation (table 8.2). Experimentally, mean and median total diameter expansion rates of 2.10 mm/year up to 5.28 mm/year were established for type B dissections with a patent false lumen [92, 220–222]. The model, thus, predicts expansion rates that are in the upper part, but still within the range, of the available experimental data. The slight increase in predicted expansion rate, compared to the measurements, might be explained by the limited time frame of the modeled results. Despite the fact that only the chronic phase was used to extrapolate the diameter expansion to a duration of one year (equation (8.15)), experimental expansion rates were calculated over longer time frames, with mean and median follow-ups ranging from 19.5 to 48.9 months, which is expected to result in a lower average expansion rate [92, 220–222]. Indeed, the largest expansion rates have been observed in the first days after the dissection, whereas lower mean expansion rates of 1.2 mm/year to 1.5 mm/year are reported in the chronic phase [223, 224]. Moreover, slight differences in the methodology to obtain the total diameter, e.g. considering the short-axis diameter, might lead to a discrepancy between the experimental and the modeled results too [221]. Taking this into account, the model predictions reasonably approach the existing measurements.

Only few data are available on the evolution of the true and false lumen size, but an increase of the false lumen size over time, both in absolute and relative terms, has been observed, in line with the simulated data [225, 226]. The extent to which the false lumen size increases, however, differs. While the current results show a median expansion rate of 19.63–19.73 mm/year in absolute terms, which corresponds to a relative increase from 24.9% to about 49.0% of the corresponding total diameter, a mean false lumen growth rate of 6.52 mm/year and a relative increase up to 12% of the total diameter was found [225, 226]. Even lower growth rates were established when considering growth from the chronic phase on [224]. Regarding the true lumen, a slight increase in absolute size was reported, with growth rates of 0.8 mm/year to 1.0 mm/year, both for measurements starting at the acute and chronic phase [224, 225]. A strong decrease, with median rates up to -14.99 mm/year, is, on the contrary, found in the current study. It is hypothesized that the distinction between the resulting and reported true and false lumen growth rates is related to the

use of a slice model, where the connection of the dissected membrane to the healthy aortic wall is limited and the movement of the dissected membrane, thus, less restricted compared to a patient-specific dissected aorta (figure 8.1). Moreover, the large circumferential size of the false lumen included in the model might play a role. Indeed, a false lumen angle of 245° , obtained based on a patient-specific CT scan, is at the higher range of the physiological values [62, 198]. Next to a strong decrease in true lumen diameter, a flattening of the true lumen was observed. To the authors' knowledge, experimental data which could confirm or contradict this observed trend is currently lacking and results are to be interpreted keeping in mind the explorative computational character of the study.

In this respect, it is noteworthy that the implemented material model assumes that the collagen fibers do not contribute to load bearing in compression. Doubts have, however, been raised regarding this assumption [227]. If collagen fibers would provide resistance against deformation in compression, decreased displacements of the dissected membrane and changes in true and false lumen size are expected over time. This might have some impact on the resulting thickening rates, the stress-mediated (decrease in) collagen production and, consequently, the collagen content of the dissected membrane. While determining the effect of this assumption on the dissected membrane would be of interest, no major effect on the total diameter expansion rate is expected. The assumption is, therefore, expected to affect the selection of material parameters that lead to thickening rates within the clinical extended range, rather than the pathophysiological relevance of the presented model.

The evolution of the false lumen, true lumen and total diameter was found to be similar for the full and local transient inflammation pattern (table 8.2). On the one hand, the change in true and false lumen diameter is generally dictated by the deformation of the dissected membrane. The total diameter, on the other hand, is mainly impacted by the deformation of the remaining wall as a consequence of the increased load due to the dissection. As the medial collagen fibers are more circumferentially oriented compared to the adventitial ones, the medial tissue strength provides the highest resistance against the deformation, which takes place in the circumferential direction as the axial stretch is fixed. The medial layer that surrounds the false lumen, thus, largely determines the overall change in geometry, while the adventitial layer and the media of the true lumen wall play a limited role. As this tissue portion is not differently af-

ected by the local and full inflammation pattern, no major effects in the overall range of diameters are observed.

Interestingly, the overall modeled changes in microstructure correspond to the experimental observations. Indeed, the model indicates a decrease in functional elastin content over time, induced by the inflammation, which agrees with the presence of fragmented elastin in the dissected membrane (figure 8.8) [33, 41, 43]. While fibrosis, indicating an abundant presence of collagen, has been experimentally observed in the dissected membrane, the collagen content of the considered samples either increased or decreased [33, 43]. In this respect, it is worth noting that no constraints on the relation between $k_{\Gamma-}^c$ and $k_{\Gamma+}^c$ were applied, which implies that for some samples a higher inflammation-mediated collagen degradation than production was imposed. These simulations, naturally, lead to a net decrease in collagen. No requirements regarding the balance between the stress- and inflammation-mediated growth and remodeling were defined either. Indeed, the collagen production is expected to be purely attributed to the inflammation as the dissected membrane is in a quasi-stress-free state in the acute phase, which will impose a negative stress-mediated collagen production that decreases the overall collagen production. If $k_{\Gamma+}^c$ was only slightly higher than $k_{\Gamma-}^c$, a decrease in collagen content was obtained in case the corresponding k_{σ}^c was relatively large, in particular when the inflammatory response was restricted to a limited time frame. This is also illustrated by two examples shown in appendix F (section 8.11).

A slight difference between the local and full inflammation pattern was found in this respect. In case of local inflammation, 22 of the 38 samples that lead to a thickening rate within the extended clinical range resulted in the expected increased collagen content at day 90. For full inflammation, an increasing collagen content was observed for only 13 of the 24 samples within the extended clinical thickening range

Despite the limited differences between the full and local inflammation pattern, the presence of less samples with a decreasing collagen content with local inflammation might imply that the local inflammation is slightly more appropriate to represent the physiological process.

Although an increase in collagen and a decrease in elastin in the dissected membrane corresponds to the reported data, a quantitative comparison with published experiments is not straightforward [33,

41, 43]. Indeed, the model considers the functional elastin and collagen, while e.g. fragmented elastin might be part of the experimental staining, and thus the published area fractions. Moreover, the model only accounts for elastin and collagen, whereas other constituents are intrinsically included in the total soft tissue area determined in experiments. Thus, the total area or volume obtained from the model and experiments might differ. Furthermore, it is not always unambiguously indicated whether the results are compared to control samples in absolute amounts or with respect to the corresponding total soft tissue area/volume [43].

8.4.1 Limitations

The presented model approaches the soft tissue growth and remodeling in aortic dissections in terms of thickening rates, total diameter expansion rates and changes in elastin and collagen, but it does not account for the presence of other constituents as smooth muscle cells or glycosaminoglycans. Glycosaminoglycans are, however, expected to play a role in the dissection initiation and progression [6, 58]. Next, the model represents an idealized aortic dissection, without tears or healthy aortic wall, which is strongly simplified compared to a patient-specific geometry. Moreover, the obtained results are based on one set of HGO material parameters for the medial and adventitial layer and, thus, no fiber dispersion was included. The material parameters were selected based on a representative PWV for a healthy middle-aged human. As differences in the behavior of healthy and (pre-)dissected wall tissue are expected [38], the considered PWV and the corresponding material parameters should be considered as an approximation of the acute dissected wall behavior. However, no representative information on the PWV of pre-dissection or acute dissection patients was available, to the authors' knowledge.

For the acute material behavior, area fractions were used to determine the relation between the same constituents of the medial and adventitial layer, on the one hand, and between the elastin and collagen fractions within each material layer, on the other hand. This option was chosen in order to represent the elastin and collagen content in a more intuitive manner, i.e. as fraction of a tissue portion of the considered layer that contains no other constituents than elastin and collagen. To confirm that the impact is limited to the representation of the constituent content, the example case shown in figure 8.5 and 8.6 was repeated with the amount of elastin and collagen provided in absolute terms (data not shown). The maximal element-wise difference in fiber stress was limited to 1.0% for the dissected

wall after 90 days of growth and remodeling, when comparing the applied model to a model where the elastin and collagen content was expressed in absolute terms. This negligible difference is hypothesized to be the consequence of the rounding during the calculation of the relative fractions.

For the dissected membrane, no net load was assumed, to reduce the simulation time as convergence was more easily achieved. However, this assumption is an approximation as it neglects the difference in surface of both sides of the dissected membrane on which the pressure is applied. A comparison with and without an explicit pressure load on both surfaces of the dissected membrane indicated an average elementwise difference of 1.6% relative to the maximal fiber stress in the dissected membrane at the start of the growth and remodeling process (data not shown). This limited effect on the fiber stress of the dissected membrane, therefore, justifies the assumption that there is no net loading at the dissected membrane.

Furthermore, the current knowledge on the evolution of the dissected membrane thickness over time is limited. To the best of the authors' knowledge, the only reference reporting quantitative thickening rates of the dissected membrane is Peterss et al., with thicknesses measured from CT scans, which imposes quite some uncertainty on the obtained ranges [44]. This uncertainty was accounted for by including an additional range of 8.00 mm to the 95% confidence interval. This extended clinical range might, however, overestimate the true uncertainty of the CT measurement. Despite the potential overestimation, the predefined range allows the determination of a selection of growth and remodeling parameters that are able to approximate the experimental observations. This selection can be applied to guide the reduction of the total growth and remodeling parameter space to a subspace with a higher rate of potentially physiological parameter combinations, which are usable in computational models.

8.5 CONCLUSION

An idealized model was developed to represent the dissected membrane thickening during the transition from acute to chronic dissection as a consequence of stress- and inflammation-mediated growth and remodeling. A parametric study of the growth and remodeling parameters was performed for multiple inflammation patterns, that differed based on the applied location and duration. For a subset of the considered growth and remodeling parameter space, the transient inflammation was able to reproduce the experimentally observed

trends of the thickening rates and the total diameter expansion rate. The changes in elastin and collagen content over time could be represented by the transient inflammation as well, in particular when it was locally applied around the false lumen. The developed model framework is, consequently, able to represent the clinically observed situation, while it also provides guidance to reduce the growth and remodeling parameter space.

8.6 APPENDIX A: VERIFICATION OF SLICE MODEL

The slice model is a simplification of the dissected aortic wall model as indicated in chapter 7. The applied boundary and loading conditions are the same and also the material properties are similar. However, due to the nature of the model implementation, some slight differences in material behavior are present.

In chapter 7, the material is considered to be purely incompressible. The parameter D , defined as

$$D = \frac{2}{K}, \quad (8.16)$$

with K being the bulk modulus of the soft tissue, can therefore be considered as 0.

In this chapter, where the soft tissue can grow and remodel, the material has to be implemented as quasi-incompressible, thus requiring a small non-zero value for D , which was adopted to be 0.001 MPa^{-1} . As the material is still quasi-incompressible, hybrid elements were still applied, but a slightly different implementation to integrate the hydrostatic pressure stress was required by Abaqus.

In order to ensure correspondence between both the full and quasi-incompressible version, the acute geometry at diastolic pressure is compared in terms of maximal principal Cauchy stress and displacement magnitude. Therefore, the average and maximal element- and nodewise difference of the respective maximal principal Cauchy stress and displacement magnitude was considered. An average and maximal absolute elementwise maximal principal Cauchy stress deviation of 0.005 and 0.022 MPa was found, while the average and maximal nodewise difference in displacement magnitude was limited to $0.4 \cdot 10^{-4} \text{ mm}$ and $3.2 \cdot 10^{-4} \text{ mm}$. Compared to the maximum maximal principal Cauchy stress and displacement of, respectively, 0.480 MPa and 5.17 mm for the fully incompressible model, the maximal element- and nodewise deviations were 4.7% for the maximal principal Cauchy stress and $6.2 \cdot 10^{-3}\%$ for the displacement, and were thus sufficiently small to consider both methodologies as equivalent.

8.7 APPENDIX B: STRESS-MEDIATED GROWTH AND REMODELING OF A HEALTHY AORTIC WALL

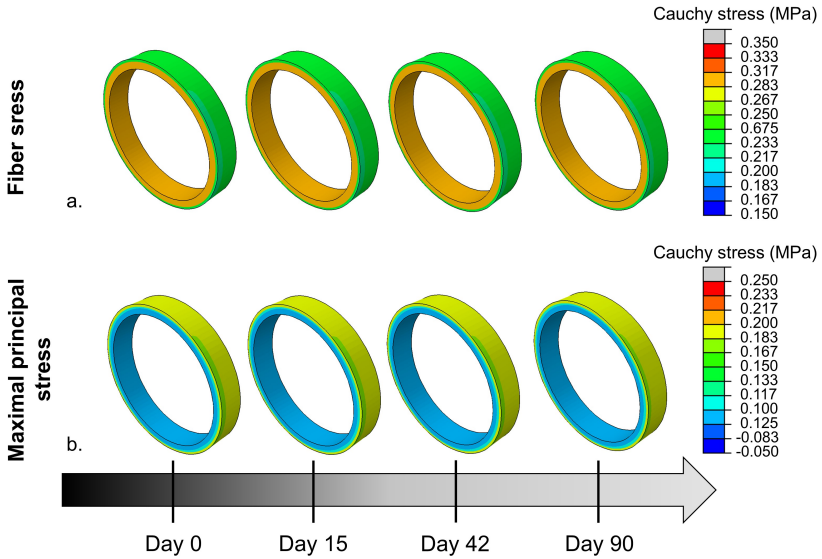


Figure 8.9: Evolution of the collagen fiber and the maximal principal Cauchy stress during stress-mediated growth and remodeling of a healthy aortic wall for an example sample, i.e. the same sample as indicated in figure 8.5 with $k_{\sigma}^c = 0.130$. Note that the fiber stress is shown for one fiber family of the medial and adventitial layer, which is representative for the second family too.

8. GROWTH AND REMODELING OF THE DISSECTED MEMBRANE IN AN IDEALIZED DISSECTED AORTA

8.8 APPENDIX C: THICKENING RATES FOR THE PERMANENT INFLAMMATION PATTERNS

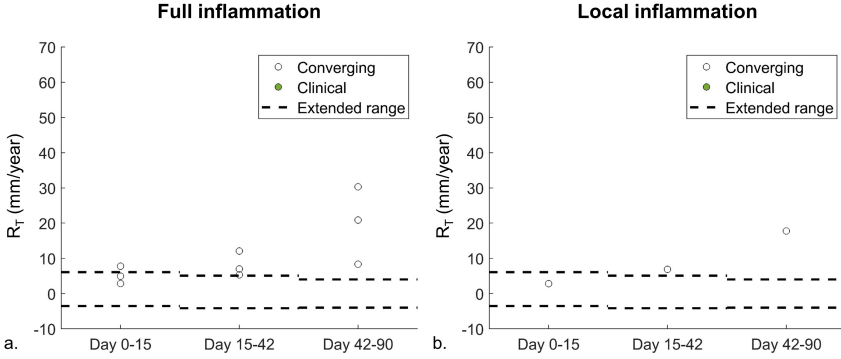


Figure 8.10: Resulting thickening rates, R_T , of the dissected membrane for the (a) full and (b) local permanent inflammation pattern, for the acute (Day 0-15), subacute (Day 15-42) and chronic (Day 42-90) phase. The rates corresponding to converging simulations are indicated with black circles. The points corresponding to converged simulations that lead to thickening rates within the extended clinical range would be filled in green, but are not present for the permanent inflammation pattern. The upper and lower boundaries of the extended clinical range for the three phases are shown with a dashed line.

8.9. Appendix D: Time evolution of example cases with a transient inflammation pattern

8.9 APPENDIX D: TIME EVOLUTION OF EXAMPLE CASES WITH A TRANSIENT INFLAMMATION PATTERN

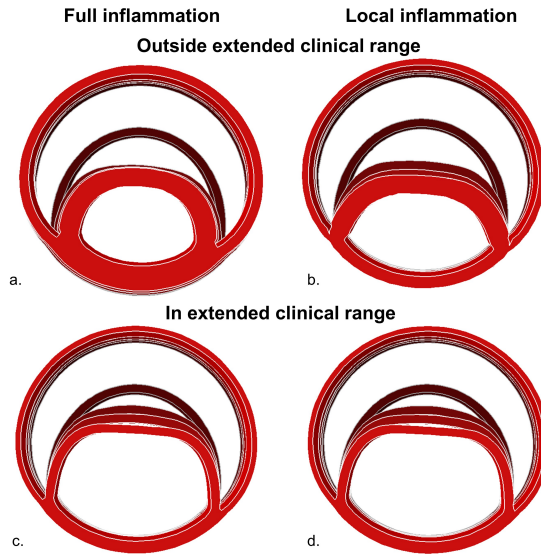


Figure 8.11: Front view of the predicted changes in geometry over time due to the growth and remodeling for samples with transient inflammation that is applied (a, c) over the full geometry and (b, d) locally at the false lumen, which result in thickening rates (a, b) outside and (c, d) within the extended clinical range. The presented samples correspond to those illustrated in figure 8.2. The deformed configurations at day 0, 15, 42 and 90 are shown in an increasingly bright shade of red.

8. GROWTH AND REMODELING OF THE DISSECTED MEMBRANE IN AN IDEALIZED DISSECTED AORTA

8.10 APPENDIX E: PARAMETER COMBINATIONS WITH CLINICALLY OBSERVED THICKENING RATES

Table 8.3: Growth and remodeling parameter combinations that result in thickening rates within the extended clinical range for the transient full inflammation pattern.

k_{σ}^c (-)	$k_{\Gamma+}^c$ (-)	$k_{\Gamma-}^c$ (-)	$k_{\Gamma-}^e$ (step ⁻¹)	δ (day ⁻¹)	β (-)
0.015	3.57	3.55	0.0403	0.349	3.23
0.074	11.64	10.60	0.0476	0.390	1.82
0.084	3.12	2.16	0.0145	0.253	1.37
0.033	4.30	2.82	0.0165	0.326	3.09
0.052	5.79	5.03	0.0147	0.145	2.97
0.130	5.34	3.67	0.0533	0.198	1.24
0.169	9.90	3.13	0.0135	0.343	1.28
0.075	18.58	16.82	0.0555	0.215	1.16
0.068	4.89	2.50	0.0671	0.454	3.24
0.001	4.46	7.87	0.0384	0.357	1.86
0.034	4.97	6.46	0.0230	0.296	3.86
0.002	5.09	4.58	0.0155	0.301	1.35
0.018	7.47	7.42	0.0462	0.171	1.52
0.099	5.62	6.91	0.0088	0.406	1.87
0.046	7.88	11.33	0.0367	0.460	1.41
0.168	3.83	2.96	0.0076	0.227	2.98
0.055	2.83	1.66	0.0227	0.276	2.41
0.046	2.01	1.46	0.0541	0.119	2.47
0.112	13.46	18.06	0.0197	0.450	1.21
0.045	3.44	2.43	0.0420	0.339	3.93
0.123	5.11	6.97	0.0031	0.356	1.54
0.090	2.32	2.00	0.0429	0.227	2.69
0.113	7.38	6.85	0.0217	0.249	1.11
0.134	16.44	7.16	0.0124	0.436	1.22

8.10. Appendix E: Parameter combinations with clinically
observed thickening rates

Table 8.4: Growth and remodeling parameter combinations that result in thickening rates within the extended clinical range for the transient local inflammation pattern.

k_{σ}^c (-)	$k_{\Gamma+}^c$ (-)	$k_{\Gamma-}^c$ (-)	$k_{\Gamma-}^e$ (step ⁻¹)	δ (day ⁻¹)	β (-)
0.015	3.57	3.55	0.0403	0.349	3.23
0.344	5.48	4.69	0.0173	0.094	3.17
0.074	11.64	10.60	0.0476	0.390	1.82
0.084	3.12	2.16	0.0145	0.253	1.37
0.033	4.30	2.82	0.0165	0.326	3.09
0.052	5.79	5.03	0.0147	0.145	2.97
0.226	4.79	2.18	0.0643	0.293	4.57
0.130	5.34	3.67	0.0533	0.198	1.24
0.087	6.06	4.80	0.0679	0.388	3.57
0.169	9.90	3.13	0.0135	0.343	1.28
0.075	18.58	16.82	0.0555	0.215	1.16
0.068	4.89	2.50	0.0671	0.454	3.24
0.290	11.88	9.53	0.0470	0.382	2.40
0.154	20.05	14.50	0.0342	0.394	1.18
0.002	5.09	4.58	0.0155	0.301	1.35
0.005	13.19	12.10	0.0628	0.271	4.33
0.018	7.47	7.42	0.0462	0.171	1.52
0.224	16.13	13.40	0.0241	0.356	1.29
0.099	5.62	6.91	0.0088	0.406	1.87
0.046	7.88	11.33	0.0367	0.460	1.41
0.168	3.83	2.96	0.0076	0.227	2.98
0.055	2.83	1.66	0.0227	0.276	2.41
0.035	6.11	5.31	0.0693	0.195	2.77
0.046	2.01	1.46	0.0541	0.119	2.47
0.129	17.26	17.15	0.0670	0.447	1.50
0.389	4.55	3.45	0.0206	0.243	3.49
0.112	13.5	18.06	0.0197	0.450	1.21
0.261	5.16	2.90	0.0691	0.457	4.24
0.163	5.50	3.77	0.0327	0.162	3.70
0.045	3.44	2.43	0.0420	0.339	3.93
0.123	5.11	6.97	0.0031	0.356	1.54
0.090	2.32	2.00	0.0429	0.227	2.69
0.038	13.91	16.09	0.0472	0.393	1.55
0.009	4.00	6.73	0.0074	0.370	3.50
0.113	7.38	6.85	0.0217	0.249	1.11
0.158	7.42	7.17	0.0104	0.447	3.20
0.239	4.81	4.09	0.0034	0.425	2.44
0.134	16.44	7.16	0.0124	0.436	1.22

8.11 APPENDIX F: EVOLUTION OF ELASTIN AND COLLAGEN CONTENT OF TWO EXAMPLE SAMPLES

The evolution of the elastin and collagen content is illustrated for two example samples with local transient inflammation, in particular differing by the timing and width of the peak of the inflammatory response (A: peak at day 14, width at 50% of the peak of 24 days; B: peak at day 1, width at 50% of the peak of 4 days). The parameters of both examples are indicated in table 8.5 and the transient inflammation pattern is illustrated in figure 8.12. Note that the inflammation-mediated collagen production, $k_{\Gamma+}^c$, is higher than the degradation, $k_{\Gamma-}^c$, in both examples. The peak of the inflammation pattern of example A extends, however, over a larger time frame compared to example B.

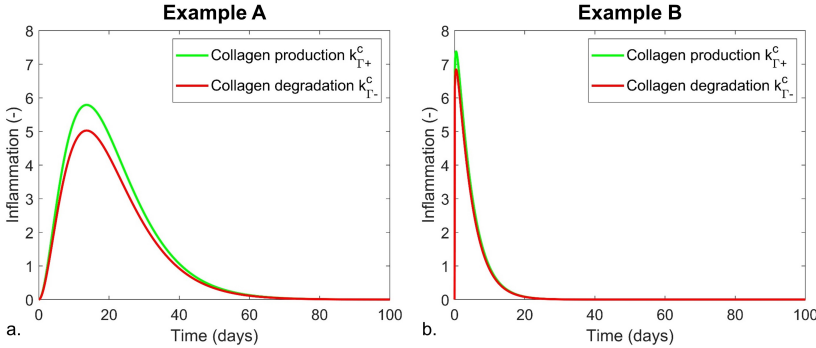


Figure 8.12: Overview of the transient inflammation pattern, Γ_t , of (a) example A and (b) example B. The pattern is indicated for the inflammation-mediated collagen production, $k_{\Gamma+}^c$, and degradation, $k_{\Gamma-}^c$, in green and red, respectively.

The resulting evolution in elastin and collagen content of the dissected membrane is shown in figure 8.13, where the content of elastin decreases for respective examples A and B to 40.6% and 44.8%. For collagen, the content increases to 63.5% for example A, while a decrease to 51.0% was found for example B. The reason for the overall decrease in collagen content in case B is attributed to the short period of inflammation in combination with the rather large decrease in stress-mediated collagen production.

The discussed examples both have a transient inflammation pattern. Note, however, that the evolution in dissected membrane microstructure is completely similar for the full inflammation pattern

8.11. Appendix F: Evolution of elastin and collagen content of two example samples

Table 8.5: Growth and remodeling parameters of example A and B.

Example	k_{σ}^c (-)	$k_{\Gamma+}^c$ (-)	$k_{\Gamma-}^c$ (-)	$k_{\Gamma-}^e$ (step ⁻¹)	δ (day ⁻¹)	β (-)
A	0.052	5.79	5.03	0.0147	0.145	2.97
B	0.113	7.38	6.85	0.0217	0.245	1.11

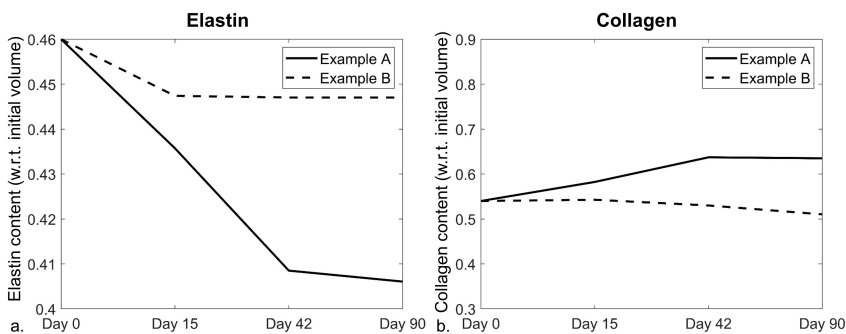


Figure 8.13: Evolution of the (a) elastin and (b) collagen content of both example samples. The evolution of example A and B is, respectively, indicated with a full and dashed line. Note that the constituent content was determined at day 0, 15, 42 and 90. The values in between were obtained via linear interpolation

as the same elastin and collagen content was obtained after 90 days of growth and remodeling.

III

General Discussion

CHAPTERS

9 Conclusion and outlook

137

Conclusion and outlook

9.1 SUMMARY

Computational biomechanical models are increasingly used to contribute to patient-specific clinical decision making, in particular for diseases where the current treatment procedure is suboptimal, which is the case for type B aortic dissections. The availability of medical imaging techniques, such as computed tomography (CT) or magnetic resonance imaging (MRI) scanning, yields the overall geometry of the patient-specific dissected aorta. However, more detailed geometrical information, such as the thickness of the aortic wall and its layers, and other functional parameters, such as the material behavior or the microstructural composition of the wall, can currently not yet be measured non-invasively in clinical practice. The lack of these data for individual patients introduces uncertainty in the computational models and their results. This dissertation attempts to estimate the impact of the introduced uncertainty for some aspects related to the biomechanical modeling of the dissected aortic wall. In this respect, the major sources of uncertainty are pointed out, thus providing guidelines for future advancements of models in the framework of aortic dissections. The uncertainty, as a consequence of the lack of non-invasive data of the wall geometry and material behavior, was considered at three levels in chapters 6-8.

Indeed, the impact of limited information on the material behavior was assessed in chapter 6 together with the potential of pulse

wave velocity measurements to reduce the corresponding uncertainty for non-dissected aortas. Chapter 7 discussed the importance of the wall thickness and stiffness as sources of uncertainty for the predicted wall stresses and displacements of an idealized acute dissection. In chapter 8, the growth and remodeling process of a slice of the idealized dissected aortic wall was considered, in an attempt to reproduce the clinically observed membrane thickening and diameter expansion, despite the large uncertainty in the existing growth and remodeling parameter ranges.

A strong impact of uncertain material parameters was found. If no information on the material is available, the assumed behavior is the most important source of uncertainty in the predicted deformation of the acute dissection (chapter 7). Clinical pulse wave velocity measurements might, however, provide guidance in selecting proper parameter combinations and are, therefore, able to reduce the uncertainty in terms of pressure-area behavior (chapter 6). Despite the potential reduction, the assumed material parameters still remain an important source of uncertainty for compliant arteries if only pulse wave velocity measurements at diastolic pressure are available, which can be further reduced with pulse wave velocity measurements at higher pressures, as dicrotic notch pressure.

While the dimensions of the dissected aortic wall were of lesser importance for the predicted deformations, an unknown percentage of dissected membrane thickness imposed a high uncertainty on the resulting wall stress, which is considered as an indicator for potential aortic wall rupture and, thus, the need for treatment (chapter 7).

Next to the uncertainty related to parameters of the acute dissection, the growth and remodeling process is not yet fully elucidated. Based on stress- and transient inflammation-mediated growth and remodeling, a selection of parameter combinations was obtained that resulted in a physiological dissected membrane thickening and diameter expansion (chapter 8). These results might contribute to the parameter space reduction of the growth and remodeling parameters and, therefore, reduce the corresponding uncertainty. Note, however, that the selected parameter combinations reproduce the clinical observations rather than clarify the underlying mechanobiological mechanisms that induce the dissected membrane thickening and diameter expansion.

9.2 DISCUSSION

9.2.1 Advancements in dissected aortic wall models

The presented idealized acute dissected aortic wall model advances the state-of-the-art, due to its combination of geometrical and material complexity. Together with the use of a microstructure-informed constitutive law, the model framework determines the *in vivo* configuration of an acute dissection starting from the pre-dissected geometry and, thus, as a consequence of the physiological stress release. Next to avoiding an artificially deformed configuration, as otherwise required in idealized geometries, this methodology benefits from a physiological material behavior, while strong simplifications are often imposed in patient-inspired geometries [21, 138–142, 147]. Moreover, the computational cost per simulation remains limited, which implies that the impact and importance of uncertain thickness and stiffness parameters on the resulting stresses and deformation of dissected wall models can be quantified based on a global sensitivity analysis. This was not investigated before in the framework of aortic dissections.

Furthermore, the growth and remodeling process of the dissected membrane and its thickening during the transition from the acute to chronic phase is reproduced for the first time, together with the corresponding diameter expansion rate. Moreover, the presented workflow, based on a geometrically simplified model, provides a method to determine potential growth and remodeling parameter combinations from clinical observations.

9.2.2 Coupling between pulse wave velocity and constitutive parameters

The potential of non-invasive pulse wave velocity measurements to reduce the parameter space was assessed by considering the Gasser-Ogden-Holzapfel material model. While this is one of the most commonly applied constitutive laws in arterial biomechanics, the method is easily transferable to other constitutive laws. The proposed technique mainly provides an innovative pragmatic perspective on the modeling of arterial tissues. While previous methodologies, commonly relying on parameter fitting, often aim to determine one ground-truth parameter combination, this method considers the global pressure-area behavior of a set of parameter combinations [172–176]. On the one hand, the selection of multiple potential parameter combinations enables the determination of the corresponding uncertainty on the global material behavior and, thus, the resulting deformation and stresses. On the other hand, it

avoids the need to assume that the applied parameter combination corresponds to the underlying ground-truth parameters, which is often unknown in clinical practice, while the technique still ensures a material behavior within the physiological range.

Note, however, that the resulting parameter sets are pragmatic, i.e. they represent the global material behavior, but not necessarily the true material microstructure. In applications where the reproduction of the global material behavior is sufficient, this technique is applicable, in particular when the uncertainty is accounted for. In the current dissertation, the link between the material parameters and the pulse wave velocity measurements was applied to the dissected aortic wall models too (chapter 7 and 8). When considering the growth and remodeling of the dissection, a lack of information on the tissue microstructure might affect the reliability of the result. Indeed, the (homogenized) constrained mixture growth and remodeling processes are intrinsically dependent on the modeled constituents and their stresses [134, 135]. The difference in behavior between two parameter combinations with a similar acute behavior might, thus, enlarge during growth and remodeling. Due to lacking knowledge on appropriate parameters for the short- and long-term behavior of the dissected aortic wall, the applied technique is considered acceptable. However, the impact of the corresponding uncertainty on the long-term result should be assessed before applying this technique systematically in the framework of growth and remodeling.

9.2.3 Uncertainty in dissected aortic wall models

While uncertainty was considered in chapters 6-8 of the dissertation, the analysis was performed in different ways. For the idealized acute dissected aortic wall model, the uncertainty was rigorously assessed based on a global sensitivity analysis, where the wall stiffness and relative dissected membrane thickness were found to be the most influential sources of uncertainty. This indicates that these parameters need to be systematically integrated in the uncertainty analysis as long as they cannot be determined more accurately from clinical data. The uncertainty in the relation between the constitutive model parameters and the pulse wave velocity measurements was considered based on the global material behavior, which is a tangible representation of the combined material parameters. Besides, the number of parameter combinations resulting in the clinically observed range, together with the corresponding (reduced) parameter space, represents the uncertainty in a more implicit way. This option was applied to

both the constitutive material and the growth and remodeling parameters. This parameter space reduction does not indicate the major sources of uncertainty, but narrows down the total search field of potentially useful parameter combinations for future computational (dissected) aortic wall models.

Despite the fact that the impact of uncertainty was assessed in each of the considered models, the combined uncertainty was not determined. This does not counteract the value of the presented results, but rather indicates that they should be considered as a lower boundary for the total uncertainty in dissected aortic wall models.

9.3 LIMITATIONS AND FUTURE PERSPECTIVES

9.3.1 Model assumptions and validation

While the presented dissected aortic wall models advance the state-of-the-art, they are based on some assumptions regarding the modeled geometry and material behavior.

The implemented material models accounted for the anisotropic hyperelastic behavior of a constrained mixture composed of elastin and collagen together with their deposition stretches and reproduced the aortic wall behavior of the media and adventitia on the short- and long-term. Other constituents as smooth muscle cells and glycosaminoglycans were, however, not included in the model. Moreover, the applied material behavior and pre-stresses were assumed to be constant throughout the circumferential and axial direction within the healthy and acute dissected aortic wall models. Only in the case of growth and remodeling with a local inflammation pattern, the soft tissue behavior could be heterogeneous in the circumferential direction as the tissue grew and/or remodeled. Furthermore, the aortic wall behavior relies on parameters obtained for the healthy thoracic aorta, due to a lack of data on material parameters of the dissected aortic wall. As indicated in section 2.2.2, the tissue of the dissected wall is, however, expected to differ on a microstructural level from the healthy aorta. While large ranges were considered for each of the material parameters, which strengthens the hypothesis that the results are representative for the dissected wall tissue, this emphasizes the need for experimental data of aortic dissection tissue to confirm this hypothesis. Irrespective of the applied material parameters, it is noteworthy that the Gasser-Ogden-Holzapfel constitutive model and homogenized constrained mixture theory are phenomenological

approaches, rather than directly reflecting the underlying biological processes [15, 134].

Moreover, the current conclusions are drawn based on one geometry for the idealized healthy and dissected aortic wall. This implies that no variations in lumen diameter, axial and circumferential false lumen size, location and size of the tears and curvature of the aorta were assessed. As these parameters might be estimated from clinical CT or MRI scans, their uncertainty is assumed to be limited to the measurement errors. It is, therefore, not expected that this additional uncertainty will strongly affect the reported global uncertainty estimations. Nevertheless, accounting for these measurement errors is encouraged in further studies, to expand the knowledge of their impact on the uncertainty on the predicted deformations and stresses. Besides, the geometry was idealized and increasing the geometrical complexity, and the axial (dissection) length in particular, is expected to affect the absolute values of the resulting wall deformation. However, the fact that the idealized models lead to deformations within the same order of magnitude as the clinical observations supports the future applicability of idealized, and thus less computationally expensive models, in assisting surgeons in the prediction of dissection progression in response to an optimal medical or endovascular treatment.

To confirm the obtained results, despite the limitations regarding the implemented material behavior and idealized geometry, validation of the current models is inevitable before considering the clinical applicability. The required validation is two-fold. First, the wall deformation and stress of the idealized models need to be compared to more complex, patient-inspired and -specific, aortic dissection geometries. Second, the predicted deformations should be validated against clinical *in vivo* observations, from the acute behavior as well as the growth and remodeling process from the acute to chronic phase. Validation of the *in vivo* stress predictions is, up to now, not yet possible in a clinical context. For both types of validation, attention has to be paid to the absolute values as well as the corresponding uncertainty. Indeed, the main goal of this dissertation and the presented models is to consider the importance of uncertain thickness and material parameters on the resulting deformations and stresses rather than reproducing the exact results.

9.3.2 Towards predictive dissection models

After validation of the short- and long-term dissected aortic wall models, the next steps are the inclusion of aspects such as the axial dissec-

tion propagation, interaction with the blood flow and treatment effect. As normotensive blood pressures were considered in the applied models, the modeled situation is comparable to the optimal medical treatment where, amongst others, drugs are provided to lower the hypertensive blood pressure to a normotensive one [25, 83]. In order to assess the effect of an endovascular treatment, the deployment of a stent-graft has to be included. This step is particularly useful when considering a patient-inspired or -specific geometry. In this respect, a thrombus formation model should be combined with the blood flow and dissected wall model to evaluate the patient-specific clinical outcome *a priori*. Indeed, the presence or absence of thrombus formation in the false lumen is one of the main clinical factors to assess whether the desired result of the treatment is achieved [84]. While models of the stent-graft deployment and thrombus formation have been developed in the framework of aortic dissections [142, 169, 228, 229], a combination of those models with an advanced dissected aortic wall model is yet to be developed.

9.3.3 Reducing the model input uncertainty

As the aortic wall behavior and the relative dissected membrane thickness were found to largely contribute to the output uncertainty, the development and integration of non-invasive techniques to accurately determine those parameters in the clinical environment is encouraged to enhance the reliability of the dissected aortic wall models. In this respect, improved reconstruction algorithms and ultra-high-resolution CT scans have, among others, been developed to increase the image quality and resolution, respectively [230–232]. Their applications are, however, mainly oriented towards smaller arteries, such as the coronary and hepatic arteries. When extrapolating these techniques towards the aorta, these CT scans might improve the *in vivo* estimation of the relative dissected membrane thickness. Although the spatial resolution of MRI scanning is increasing as well, it currently remains lower compared to that of CT scanning [233, 234].

A non-invasive manner to determine the aortic wall behavior has been the subject of multiple studies during the past decades. Inverse finite element models exist to iteratively determine the material properties of the aorta based on the observed deformation [235–238]. Similarly as for parameter fittings based on experimental data, this technique leads to a single parameter combination without estimation of the corresponding uncertainty. Moreover, inverse finite element models are often computationally very expensive as each iteration requires to perform a finite element analysis. Rather than

attempting to directly extract the parameter combination from *in vivo* information, the uncertainty might be further reduced more implicitly. For example, Vappou et al. coupled the average pulse wave velocity over a cardiac cycle to an average Young's modulus by using the Moens-Korteweg equation [239]. Requiring that the average stress-strain relation of proper parameter combinations approximates this observed average Young's modulus within the *in vivo* pressure range could, then, further restrict the number of potential parameter combinations.

Note that, even with a reduced input uncertainty of the wall behavior and thickness, it is recommended to integrate uncertainty quantification in the workflow when developing computational models, rather than aiming towards deterministic models. Indeed, measurement errors are unavoidable, which emphasizes the importance to quantify the expected variability on the output of interest. This does not necessarily require hundreds of model evaluations per case, which would limit the clinical applicability, but testing some extreme situations might already illustrate the expected variation in the output of interest. Determining which parameter values will result in these extreme situations is not straightforward in a multi-dimensional input parameter space. Here, extensive parametric studies, such as global sensitivity analyses, might contribute to appointing the most influential input parameters.

9.3.4 The contribution of surrogate models

The use of a surrogate for the finite element dissected wall model is an attractive idea for uncertainty quantification and global sensitivity analyses, where many data points of the parameter space need to be evaluated, and for clinical applications, where simulation time is a critical factor when aiming towards (quasi-)real-time computational models [162]. The training of these biomechanical surrogate models implies, however, some challenges. First of all, many model simulations are required to obtain a reliable surrogate. This was also illustrated by the surrogate model of the idealized acute dissected aortic wall, which did not consistently lead to errors below the pixel size of clinical CT scans (chapter 7). One of the expected main causes is the incompatibility of a large portion of the parameter combinations, which leads to non-physiological results. Although these results contribute to the uncertainty reduction, as discussed in chapter 6, they counteract the development of a surrogate model. The material parameters are, therefore, inappropriate as continuous and independent input parameters, which indicates a second challenge. To circumvent

the occurrence of many non-physiological parameter combinations, pulse wave velocity was used as material representation. Due to this coupling between the pulse wave velocity and the material parameters, no regular sampling of the material parameter space can be guaranteed, which might lead to untrained subspaces and, thus, a limited accuracy for model evaluations in this region. Similar to a random sampling, many samples might be required before covering the full physiological part of the material parameter space, which makes the use of surrogate modeling not straightforward.

In the framework of uncertainty quantification, Gaussian process regression might counteract this drawback by accounting for the additional model uncertainty in these untrained subspace [164]. Moreover, model simplifications might be implemented in the finite element analysis to limit the computational cost of the surrogate model training, despite the need for large amounts of model evaluations. This further supports the potential of artificial intelligence, and Gaussian process regression in particular, for uncertainty quantification purposes in dissected aortic wall models similar to the application presented in chapter 7.

Although the real-time prediction of the recommended patient-specific treatment for type B aortic dissections sounds very promising, the application of surrogate models in clinical practice in the near future is debatable. In this case, the surrogate model should be able to reproduce the results of patient-specific finite element analyses with a high accuracy. The corresponding model complexity and the expected increase in required sample size will result in a high computational cost to train surrogate models, in particular when accounting for the inter- and intra-patient variability in geometry and material behavior of the dissected aortic wall. Therefore, the availability of techniques to determine material parameters non-invasively and guidelines for the required complexity of patient-specific models, based on sensitivity analyses, is a prerequisite before surrogate models, and thus artificial intelligence, are expected to advance the clinical treatment practice of aortic dissections.

Rather than directly aiming at treatment prediction, a first step in the integration of surrogate models in clinical practice, could be the application of an improved version of the surrogate model presented in chapter 7 to non-invasively estimate potential patient-specific material parameter combinations for dissected aortic walls based on geometrical imaging information and an inverse Bayesian inference analysis.

9.4 TAKE HOME MESSAGE

Although patient-specific modeling might have the long-term potential to contribute to clinical decision making for aortic dissections, this dissertation emphasizes the strong impact of the current lack of non-invasive data on the predictive value of these models. While the uncertainty regarding the material behavior, on the short- as well as the long-term, affects the wall deformation, an unknown dissected membrane thickness results in uncertain wall stresses. This points out that those measures, which are considered to be potentially decisive for the treatment strategy of aortic dissections, cannot yet be reliably predicted based on the clinically available data. Rather than developing complex patient-specific models with deterministic predictions, probabilistic dissected aortic wall models should be aimed for as their inclusion of uncertainty provides more informative model results. Nevertheless, idealized dissected aortic wall models and clinical measurements can be utilized to reduce the uncertainty predicted by these probabilistic models.

Bibliography

- [1] R. R. DeMartino *et al.*, ‘Population-Based Assessment of the Incidence of Aortic Dissection, Intramural Hematoma, and Penetrating Ulcer, and Its Associated Mortality From 1995 to 2015’, *Circulation-Cardiovascular Quality and Outcomes*, vol. 11, no. 8, 2018.
- [2] R. Fattori *et al.*, ‘Survival After Endovascular Therapy in Patients With Type B Aortic Dissection A Report From the International Registry of Acute Aortic Dissection (IRAD)’, *Jacc-Cardiovascular Interventions*, vol. 6, no. 8, pp. 876–882, 2013.
- [3] P. Mastroberto, F. Onorati, S. Zofrea, A. Renzulli and C. Indolfi, ‘Outcome of open and endovascular repair in acute type B aortic dissection: a retrospective and observational study’, *Journal of Cardiothoracic Surgery*, vol. 5, 2010.
- [4] C. A. Nienaber, S. Kische, H. Ince and R. Fattori, ‘Thoracic endovascular aneurysm repair for complicated type B aortic dissection’, *Journal of Vascular Surgery*, vol. 54, no. 5, pp. 1529–1533, 2011.
- [5] E. M. Isselbacher, ‘Thoracic and abdominal aortic aneurysms’, *Circulation*, vol. 111, no. 6, pp. 816–828, 2005.
- [6] J. D. Humphrey, ‘Possible mechanical roles of glycosaminoglycans in thoracic aortic dissection and associations with dysregulated transforming growth factor-beta’, *Journal of Vascular Research*, vol. 50, no. 1, pp. 1–10, 2013.
- [7] A. J. Schrieffl, G. Zeindlinger, D. M. Pierce, P. Regitnig and G. A. Holzapfel, ‘Determination of the layer-specific distributed collagen fibre orientations in human thoracic and abdominal aortas and common iliac arteries’, *Journal of the Royal Society Interface*, vol. 9, no. 71, pp. 1275–1286, 2012.

-
- [8] H. Weisbecker, D. M. Pierce, P. Regitnig and G. A. Holzapfel, ‘Layer-specific damage experiments and modeling of human thoracic and abdominal aortas with non-atherosclerotic intimal thickening’, *Journal of the Mechanical Behavior of Biomedical Materials*, vol. 12, pp. 93–106, 2012.
- [9] C. Manopoulos *et al.*, ‘Identification of regional/layer differences in failure properties and thickness as important biomechanical factors responsible for the initiation of aortic dissections’, *Journal of Biomechanics*, vol. 80, pp. 102–110, 2018.
- [10] K. P. Dingemans, P. Teeling, J. H. Lagendijk and A. E. Becker, ‘Extracellular matrix of the human aortic media: An ultrastructural histochemical and immunohistochemical study of the adult aortic media’, *Anatomical Record*, vol. 258, no. 1, pp. 1–14, 2000.
- [11] P. Lacolley, V. Regnault, P. Segers and S. Laurent, ‘VASCULAR SMOOTH MUSCLE CELLS AND ARTERIAL STIFFENING: RELEVANCE IN DEVELOPMENT, AGING, AND DISEASE’, *Physiological Reviews*, vol. 97, no. 4, pp. 1555–1617, 2017.
- [12] D. C. Iliopoulos, E. P. Kritharis, A. T. Giagini, S. A. Papadodima and D. P. Sokolis, ‘Ascending thoracic aortic aneurysms are associated with compositional remodeling and vessel stiffening but not weakening in age-matched subjects’, *Journal of Thoracic and Cardiovascular Surgery*, vol. 137, no. 1, pp. 101–109, 2009.
- [13] J. K. Williams and D. D. Heistad, ‘Structure and function of vasa vasorum’, *Trends in Cardiovascular Medicine*, vol. 6, no. 2, pp. 53–57, 1996.
- [14] J. H. N. Lindeman *et al.*, ‘Distinct defects in collagen microarchitecture underlie vessel-wall failure in advanced abdominal aneurysms and aneurysms in Marfan syndrome’, *Proceedings of the National Academy of Sciences of the United States of America*, vol. 107, no. 2, pp. 862–865, 2010.
- [15] T. C. Gasser, R. W. Ogden and G. Holzapfel, ‘Hyperelastic modelling of arterial layers with distributed collagen fibre orientations’, *Journal of the Royal Society of Interface*, vol. 3, pp. 15–35, 2006.

-
- [16] J. A. Niestrawska, C. Viertler, P. Regitnig, T. U. Cohnert, G. Sommer and G. A. Holzapfel, ‘Microstructure and mechanics of healthy and aneurysmatic abdominal aortas: Experimental analysis and modelling’, *Journal of the Royal Society Interface*, vol. 13, no. 124, pp. 1–14, 2016.
- [17] J. M. Clark and S. Glagov, ‘TRANSMURAL ORGANIZATION OF THE ARTERIAL MEDIA - THE LAMELLAR UNIT REVISITED’, *Arteriosclerosis*, vol. 5, no. 1, pp. 19–34, 1985.
- [18] F. L. Wuyts, V. J. Vanhuyse, G. J. Langewouters, W. F. Decraemer, E. R. Raman and S. Buyle, ‘ELASTIC PROPERTIES OF HUMAN AORTAS IN RELATION TO AGE AND ATHEROSCLEROSIS - A STRUCTURAL MODEL’, *Physics in Medicine and Biology*, vol. 40, no. 10, pp. 1577–1597, 1995.
- [19] K. B. Rombouts, T. A. R. van Merrienboer, J. C. F. Ket, N. Bogunovic, J. van der Velden and K. K. Yeung, ‘The role of vascular smooth muscle cells in the development of aortic aneurysms and dissections’, *European Journal of Clinical Investigation*, vol. 52, no. 4, p. 24, 2022.
- [20] A. Giudici, I. B. Wilkinson and A. W. Khir, ‘Review of the Techniques Used for Investigating the Role Elastin and Collagen Play in Arterial Wall Mechanics’, *Ieee Reviews in Biomedical Engineering*, vol. 14, pp. 256–269, 2021.
- [21] K. Bäumlner *et al.*, ‘Fluid–structure interaction simulations of patient-specific aortic dissection’, *Biomechanics and Modeling in Mechanobiology*, pp. 1–22, 2020.
- [22] M. K. Ganten *et al.*, ‘Motion characterization of aortic wall and intimal flap by ECG-gated CT in patients with chronic B-dissection’, *European Journal of Radiology*, vol. 72, no. 1, pp. 146–153, 2009.
- [23] D. P. J. Howard *et al.*, ‘Population-Based Study of Incidence and Outcome of Acute Aortic Dissection and Premorbid Risk Factor Control 10-Year Results From the Oxford Vascular Study’, *Circulation*, vol. 127, no. 20, pp. 2031–+, 2013.
- [24] M. D. Dake, M. Thompson, M. van Sambeek, F. Vermassen, J. P. Morales and D. Investigators, ‘DISSECT: A New Mnemonic-based Approach to the Categorization of Aortic Dissection’, *European Journal of Vascular and Endovascular Surgery*, vol. 46, no. 2, pp. 175–190, 2013.

-
- [25] L. F. Hiratzka *et al.*, ‘2010 ACCF/AHA/AATS/ACR/ASA/SCA/SCAI/SIR/STS/SVM Guidelines for the Diagnosis and Management of Patients With Thoracic Aortic Disease’, *Journal of the American College of Cardiology*, vol. 55, no. 14, E27–E129, 2010.
- [26] P. O. Daily, H. W. Trueblood, E. B. Stinson, R. D. Wuerflein and N. E. Shumway, ‘Management of Acute Aortic Dissections’, *The Annals of Thoracic Surgery*, vol. 10, no. 3, pp. 237–247, 1970.
- [27] M. E. DeBakey, W. S. Henly, D. A. Cooley, G. C. Morris, E. S. Crawford and A. C. Beall, ‘SURGICAL MANAGEMENT OF DISSECTING ANEURYSMS OF AORTA’, *Journal of Thoracic and Cardiovascular Surgery*, vol. 49, no. 1, pp. 130–149, 1965.
- [28] R. Erbel *et al.*, ‘2014 ESC Guidelines on the diagnosis and treatment of aortic diseases’, *European Heart Journal*, vol. 35, no. 41, 2873–U93, 2014.
- [29] R. Fattori *et al.*, ‘Interdisciplinary Expert Consensus Document on Management of Type B Aortic Dissection’, *Journal of the American College of Cardiology*, vol. 61, no. 16, pp. 1661–1678, 2013.
- [30] R. S. Bonser *et al.*, ‘Evidence, Lack of Evidence, Controversy, and Debate in the Provision and Performance of the Surgery of Acute Type A Aortic Dissection’, *Journal of the American College of Cardiology*, vol. 58, no. 24, pp. 2455–2474, 2011.
- [31] P. Hagan, C. Nienaber, E. Isselbacher and D. Bruckman, ‘The International Registry of Acute Aortic Dissection (IRAD): New insights into an old disease’, *JAMA*, vol. 283, no. 7, pp. 897–903, 2000.
- [32] S. Trimarchi *et al.*, ‘Role of age in acute type A aortic dissection outcome: Report from the International Registry of Acute Aortic Dissection (IRAD)’, *Journal of Thoracic and Cardiovascular Surgery*, vol. 140, no. 4, pp. 784–789, 2010.
- [33] T. J. M. Schlatmann and A. E. Becker, ‘PATHOGENESIS OF DISSECTING ANEURYSM OF AORTA - COMPARATIVE HISTOPATHOLOGIC STUDY OF SIGNIFICANCE OF MEDIAL CHANGES’, *American Journal of Cardiology*, vol. 39, no. 1, pp. 21–26, 1977.

-
- [34] F. Del Porto *et al.*, ‘Inflammation and immune response in acute aortic dissection’, *Annals of Medicine*, vol. 42, no. 8, pp. 622–629, 2010.
- [35] L. R. Xu and A. Burke, ‘Acute Medial Dissection of the Ascending Aorta Evolution of Reactive Histologic Changes’, *American Journal of Surgical Pathology*, vol. 37, no. 8, pp. 1275–1282, 2013.
- [36] M. A. Cattell, P. S. Hasleton and J. C. Anderson, ‘GLYCOSAMINOGLYCAN CONTENT IS INCREASED IN DISSECTING ANEURYSMS OF HUMAN THORACIC AORTA’, *Clinica Chimica Acta*, vol. 226, no. 1, pp. 29–46, 1994.
- [37] F. S. Cikach *et al.*, ‘Massive aggrecan and versican accumulation in thoracic aortic aneurysm and dissection’, *Jci Insight*, vol. 3, no. 5, p. 16, 2018.
- [38] V. Deplano *et al.*, ‘Mechanical characterisation of human ascending aorta dissection’, *Journal of Biomechanics*, vol. 94, pp. 138–146, 2019.
- [39] H. Yamada, N. Sakata, H. Wada, T. Tashiro and E. Tayama, ‘Age-related distensibility and histology of the ascending aorta in elderly patients with acute aortic dissection’, *Journal of Biomechanics*, vol. 48, no. 12, pp. 3267–3273, 2015.
- [40] L. D. Borges, R. G. Jaldin, R. R. Dias, N. A. G. Stolf, J. B. Michel and P. S. Gutierrez, ‘Collagen is reduced and disrupted in human aneurysms and dissections of ascending aorta’, *Human Pathology*, vol. 39, no. 3, pp. 437–443, 2008.
- [41] H. Sariola, T. Viljanen and R. Luosto, ‘HISTOLOGICAL PATTERN AND CHANGES IN EXTRACELLULAR-MATRIX IN AORTIC DISSECTIONS’, *Journal of Clinical Pathology*, vol. 39, no. 10, pp. 1074–1081, 1986.
- [42] Z. L. Ren *et al.*, ‘Decreased expression of p54(nrb)/nono correlates with collagen deposition and fibrosis in human aortic dissection’, *Histopathology*, vol. 65, no. 4, pp. 570–580, 2014.
- [43] X. W. Wang *et al.*, ‘Increased collagen deposition and elevated expression of connective tissue growth factor in human thoracic aortic dissection’, *Circulation*, vol. 114, pp. I200–I205, 2006.
- [44] S. Peterss *et al.*, ‘Changing Pathology of the Thoracic Aorta From Acute to Chronic Dissection Literature Review and Insights’, *Journal of the American College of Cardiology*, vol. 68, no. 10, pp. 1054–1065, 2016.

-
- [45] E. W. Larson and W. D. Edwards, 'RISK-FACTORS FOR AORTIC DISSECTION - A NECROPSY STUDY OF 161 CASES', *American Journal of Cardiology*, vol. 53, no. 6, pp. 849–855, 1984.
- [46] T. Suzuki *et al.*, 'Clinical profiles and outcomes of acute type B aortic dissection in the current era: Lessons from the International Registry of Aortic Dissection (IRAD)', *Circulation*, vol. 108, no. 10, pp. 312–317, 2003.
- [47] C. A. Nienaber, S. Kische and H. Rousseau, 'Endovascular Repair of Type B Aortic Dissection: Long-term Results of the Randomized Investigation of Stent Grafts in Aortic Dissection Trial', *Circulation-cardiovascular interventions*, vol. 59, pp. 554–554, 2014.
- [48] H. Mitsui, H. Uchida and S. Teramoto, 'CORRELATION BETWEEN THE LAYER OF AN INTIMAL TEAR AND THE PROGRESSION OF AORTIC DISSECTION', *Acta Medica Okayama*, vol. 48, no. 2, pp. 93–99, 1994.
- [49] I. Vilacosta and J. A. San Roman, 'Acute aortic syndrome', *Heart*, vol. 85, no. 4, pp. 365–368, 2001.
- [50] K. Rajagopal, C. Bridges and K. R. Rajagopal, 'Towards an understanding of the mechanics underlying aortic dissection', *Biomechanics and Modeling in Mechanobiology*, vol. 6, no. 5, pp. 345–359, 2007.
- [51] N. F. MacLean, N. L. Dudek and M. R. Roach, 'The role of radial elastic properties in the development of aortic dissections', *Journal of Vascular Surgery*, vol. 29, no. 4, pp. 703–710, 1999.
- [52] C. A. Nienaber *et al.*, 'INTRAMURAL HEMORRHAGE OF THE THORACIC AORTA - DIAGNOSTIC AND THERAPEUTIC IMPLICATIONS', *Circulation*, vol. 92, no. 6, pp. 1465–1472, 1995.
- [53] I. Vilacosta *et al.*, 'Natural history and serial morphology of aortic intramural hematoma: A novel variant of aortic dissection', *American Heart Journal*, vol. 134, no. 3, pp. 495–507, 1997.
- [54] H. Osada, M. Kyogoku, M. Ishidou, M. Morishima and H. Nakajima, 'Aortic dissection in the outer third of the media: what is the role of the vasa vasorum in the triggering process?', *European Journal of Cardio-Thoracic Surgery*, vol. 43, no. 3, E82–E88, 2013.

-
- [55] R. M. He *et al.*, ‘Characterization of the inflammatory and apoptotic cells in the aortas of patients with ascending thoracic aortic aneurysms and dissections’, *Journal of Thoracic and Cardiovascular Surgery*, vol. 131, no. 3, 671–U65, 2006.
- [56] F. Luo, X. L. Zhou, J. J. Li and R. T. Hui, ‘Inflammatory response is associated with aortic dissection’, *Ageing Research Reviews*, vol. 8, no. 1, pp. 31–35, 2009.
- [57] X. H. Wang, H. P. Zhang, L. Cao, Y. He, A. R. Ma and W. Guo, ‘The Role of Macrophages in Aortic Dissection’, *Frontiers in Physiology*, vol. 11, p. 8, 2020.
- [58] H. Ahmadzadeh, M. K. Rausch and J. D. Humphrey, ‘Particle-based computational modelling of arterial disease’, *Journal of the Royal Society Interface*, vol. 15, no. 149, p. 14, 2018.
- [59] S. Roccabianca, G. A. Ateshian and J. D. Humphrey, ‘Biomechanical roles of medial pooling of glycosaminoglycans in thoracic aortic dissection’, *Biomechanics and Modeling in Mechanobiology*, vol. 13, no. 1, pp. 13–25, 2014.
- [60] B. Trachet *et al.*, ‘Dissecting abdominal aortic aneurysm in Ang II-infused mice: suprarenal branch ruptures and apparent luminal dilatation’, *Cardiovascular Research*, vol. 105, no. 2, pp. 213–222, 2015.
- [61] B. Trachet *et al.*, ‘Angiotensin II infusion into ApoE^{-/-} mice: a model for aortic dissection rather than abdominal aortic aneurysm?’, *Cardiovascular Research*, vol. 113, no. 10, pp. 1230–1242, 2017.
- [62] J. Brunet *et al.*, ‘In situ visualization of aortic dissection propagation in notched rabbit aorta using synchrotron X-ray tomography’, *Acta Biomaterialia*, vol. 155, pp. 449–460, 2023.
- [63] G. Sommer, T. C. Gasser, P. Regitnig, M. Auer and G. A. Holzapfel, ‘Dissection properties of the human aortic media: An experimental study’, *Journal of Biomechanical Engineering-Transactions of the Asme*, vol. 130, no. 2, p. 12, 2008.
- [64] E. Ban, C. Cavinato and J. D. Humphrey, ‘Critical Pressure of Intramural Delamination in Aortic Dissection’, *Annals of Biomedical Engineering*, vol. 50, no. 2, pp. 183–194, 2022.

-
- [65] O. Gultekin, S. P. Hager, H. Dal and G. A. Holzapfel, ‘Computational modeling of progressive damage and rupture in fibrous biological tissues: application to aortic dissection’, *Biomechanics and Modeling in Mechanobiology*, vol. 18, no. 6, pp. 1607–1628, 2019.
- [66] T. Dziodzio *et al.*, ‘Experimental Acute Type B Aortic Dissection: Different Sites of Primary Entry Tears Cause Different Ways of Propagation’, *Annals of Thoracic Surgery*, vol. 91, no. 3, pp. 724–727, 2011.
- [67] E. M. Faure, L. Canaud, P. Cathala, I. Serres, C. Marty-Anee and P. Alric, ‘Human ex-vivo model of Stanford type B aortic dissection’, *Journal of Vascular Surgery*, vol. 60, no. 3, pp. 767–775, 2014.
- [68] A. S. M. Tam, M. C. Sapp and M. R. Roach, ‘The effect of tear depth on the propagation of aortic dissections in isolated porcine thoracic aorta’, *Journal of Biomechanics*, vol. 31, no. 7, pp. 673–676, 1998.
- [69] B. L. Guo *et al.*, ‘Dissection Level Within Aortic Wall Layers is Associated with Propagation of Type B Aortic Dissection: A Swine Model Study’, *European Journal of Vascular and Endovascular Surgery*, vol. 58, no. 3, pp. 415–425, 2019.
- [70] S. V. Peelukhana *et al.*, ‘Role of Pulse Pressure and Geometry of Primary Entry Tear in Acute Type B Dissection Propagation’, *Annals of Biomedical Engineering*, vol. 45, no. 3, pp. 592–603, 2017.
- [71] J. Brunet, B. Pierrat and P. Badel, ‘A Parametric Study on Factors Influencing the Onset and Propagation of Aortic Dissection Using the Extended Finite Element Method’, *Ieee Transactions on Biomedical Engineering*, vol. 68, no. 10, pp. 2918–2929, 2021.
- [72] H. Han *et al.*, ‘Finite-element simulation of in-plane tear propagation in the dissected aorta: Implications for the propagation mechanism’, *International Journal for Numerical Methods in Biomedical Engineering*, p. 14, 2023.
- [73] H. W. Haslach *et al.*, ‘Crack Propagation and Its Shear Mechanisms in the Bovine Descending Aorta’, *Cardiovascular Engineering and Technology*, vol. 6, no. 4, pp. 501–518, 2015.
- [74] H. W. Haslach *et al.*, ‘Fracture mechanics of shear crack propagation and dissection in the healthy bovine descending aortic media’, *Acta Biomaterialia*, vol. 68, pp. 53–66, 2018.

-
- [75] C. M. Witzenburg *et al.*, ‘Failure of the Porcine Ascending Aorta: Multidirectional Experiments and a Unifying Microstructural Model’, *Journal of Biomechanical Engineering-Transactions of the Asme*, vol. 139, no. 3, p. 14, 2017.
- [76] X. J. Yu, B. Suki and Y. H. Zhang, ‘Avalanches and power law behavior in aortic dissection propagation’, *Science Advances*, vol. 6, no. 21, p. 8, 2020.
- [77] L. Horny *et al.*, ‘Correlation between age, location, orientation, loading velocity and delamination strength in the human aorta’, *Journal of the Mechanical Behavior of Biomedical Materials*, vol. 133, p. 9, 2022.
- [78] I. Rios-Ruiz, M. A. Martinez and E. Pena, ‘Is location a significant parameter in the layer dependent dissection properties of the aorta?’, *Biomechanics and Modeling in Mechanobiology*, vol. 21, no. 6, pp. 1887–1901, 2022.
- [79] D. P. Sokolis and S. A. Papadodima, ‘Regional delamination strength in the human aorta underlies the anatomical localization of the dissection channel’, *Journal of Biomechanics*, vol. 141, p. 10, 2022.
- [80] H. J. Hansmann, N. Dobert, H. Kucherer and G. M. Richter, ‘Different Spiral CT protocol types and their significance in the diagnosis of aortic dissections: results of a prospective study’, *Rofo-Fortschritte Auf Dem Gebiet Der Rontgenstrahlen Und Der Bildgebenden Verfahren*, vol. 172, no. 11, pp. 879–887, 2000.
- [81] E. M. Isselbacher *et al.*, ‘2022 ACC/AHA Guideline for the Diagnosis and Management of Aortic Disease: A Report of the American Heart Association/American College of Cardiology Joint Committee on Clinical Practice Guidelines’, *Circulation*, vol. 146, no. 24, E334–E482, 2022.
- [82] J. J. W. Grp, ‘Guidelines for Diagnosis and Treatment of Aortic Aneurysm and Aortic Dissection (JCS 2011) - Digest Version’, *Circulation Journal*, vol. 77, no. 3, pp. 789–828, 2013.
- [83] A. L. Estrera *et al.*, ‘Outcomes of medical management of acute type B aortic dissection’, *Circulation*, vol. 114, pp. I384–I389, 2006.

-
- [84] M. Grabenwoger *et al.*, ‘Thoracic Endovascular Aortic Repair (TEVAR) for the treatment of aortic diseases: a position statement from the European Association for Cardio-Thoracic Surgery (EACTS) and the European Society of Cardiology (ESC), in collaboration with the European Association of Percutaneous Cardiovascular Interventions (EAPCI)’, *European Heart Journal*, vol. 33, no. 13, 1558–U19, 2012.
- [85] M. Brandt *et al.*, ‘Stent-graft repair versus open surgery for the descending aorta: A case-control study’, *Journal of Endovascular Therapy*, vol. 11, no. 5, pp. 535–538, 2004.
- [86] A. Harky, J. S. K. Chan, C. H. M. Wong, N. Francis, C. Grafton-Clarke and M. Bashir, ‘Systematic review and meta-analysis of acute type B thoracic aortic dissection, open, or endovascular repair’, *Journal of Vascular Surgery*, vol. 69, no. 5, pp. 1599–1609, 2019.
- [87] J. C. Iannuzzi *et al.*, ‘Favorable impact of thoracic endovascular aortic repair on survival of patients with acute uncomplicated type B aortic dissection’, *Journal of Vascular Surgery*, vol. 68, no. 6, pp. 1649–1655, 2018.
- [88] C. A. Nienaber *et al.*, ‘Nonsurgical reconstruction of thoracic aortic dissection by stent-graft placement’, *New England Journal of Medicine*, vol. 340, no. 20, pp. 1539–1545, 1999.
- [89] M. Cooper, C. Hicks, E. V. Ratchford, M. J. Salameh and M. Malas, ‘Diagnosis and treatment of uncomplicated type B aortic dissection’, *Vascular Medicine*, vol. 21, no. 6, pp. 547–552, 2016.
- [90] Z. C. Gao *et al.*, ‘Risk factors for incomplete thrombosis in false lumen in sub-acute type B aortic dissection post-TEVAR’, *Heart and Vessels*, vol. 37, no. 3, pp. 505–512, 2022.
- [91] E. M. Xie *et al.*, ‘Timing and Outcome of Endovascular Repair for Uncomplicated Type B Aortic Dissection’, *European Journal of Vascular and Endovascular Surgery*, vol. 61, no. 5, pp. 788–797, 2021.
- [92] S. Trimarchi *et al.*, ‘Importance of false lumen thrombosis in type B aortic dissection prognosis’, *Journal of Thoracic and Cardiovascular Surgery*, vol. 145, no. 3, S208–S212, 2013.
- [93] T. T. Tsai *et al.*, ‘Partial thrombosis of the false lumen in patients with acute type B aortic dissection’, *New England Journal of Medicine*, vol. 357, no. 4, pp. 349–359, 2007.

-
- [94] M. Jubouri *et al.*, ‘Mid- and long-term outcomes of thoracic endovascular aortic repair in acute and subacute uncomplicated type B aortic dissection’, *Journal of Cardiac Surgery*, vol. 37, no. 5, pp. 1328–1339, 2022.
- [95] G. A. Holzapfel, T. C. Gasser and R. W. Ogden, ‘A new constitutive framework for arterial wall mechanics and a comparative study of material models’, *Journal of Elasticity*, vol. 61, no. 1-3, pp. 1–48, 2000.
- [96] S. Baek, R. L. Gleason, K. R. Rajagopal and J. D. Humphrey, ‘Theory of small on large: Potential utility in computations of fluid-solid interactions in arteries’, *Computer Methods in Applied Mechanics and Engineering*, vol. 196, no. 31-32, pp. 3070–3078, 2007.
- [97] N. Famaey, J. Vander Sloten and E. Kuhl, ‘A three-constituent damage model for arterial clamping in computer-assisted surgery’, *Biomechanics and Modeling in Mechanobiology*, vol. 12, no. 1, pp. 123–136, 2013.
- [98] P. B. Dobrin, T. H. Schwarcz and R. Mrkvicka, ‘LONGITUDINAL RETRACTIVE FORCE IN PRESSURIZED DOG AND HUMAN ARTERIES’, *Journal of Surgical Research*, vol. 48, no. 2, pp. 116–120, 1990.
- [99] R. N. Vaishnav and J. Vossoughi, ‘RESIDUAL-STRESS AND STRAIN IN AORTIC SEGMENTS’, *Journal of Biomechanics*, vol. 20, no. 3, pp. 235–+, 1987.
- [100] A. Desyatova, J. MacTaggart and A. Kamenskiy, ‘Effects of longitudinal pre-stretch on the mechanics of human aorta before and after thoracic endovascular aortic repair (TEVAR) in trauma patients’, *Biomechanics and Modeling in Mechanobiology*, vol. 19, no. 1, pp. 401–413, 2020.
- [101] L. Wang *et al.*, ‘Effects of Residual Stress, Axial Stretch, and Circumferential Shrinkage on Coronary Plaque Stress and Strain Calculations: A Modeling Study Using IVUS-Based Near-Idealized Geometries’, *Journal of Biomechanical Engineering-Transactions of the Asme*, vol. 139, no. 1, p. 11, 2017.
- [102] C. Diaz, J. A. Pena, M. A. Martinez and E. Pena, ‘Unraveling the multilayer mechanical response of aorta using layer-specific residual stresses and experimental properties’, *Journal of the Mechanical Behavior of Biomedical Materials*, vol. 113, p. 15, 2021.

-
- [103] L. Horny, T. Adamek and M. Kulvajtova, ‘Analysis of axial prestretch in the abdominal aorta with reference to post mortem interval and degree of atherosclerosis’, *Journal of the Mechanical Behavior of Biomedical Materials*, vol. 33, pp. 93–98, 2014.
- [104] G. A. Holzapfel, G. Sommer, M. Auer, P. Regitnig and R. W. Ogden, ‘Layer-specific 3D residual deformations of human aortas with non-atherosclerotic intimal thickening’, *Annals of Biomedical Engineering*, vol. 35, no. 4, pp. 530–545, 2007.
- [105] J. A. Pena, M. A. Martinez and E. Pena, ‘Layer-specific residual deformations and uniaxial and biaxial mechanical properties of thoracic porcine aorta’, *Journal of the Mechanical Behavior of Biomedical Materials*, vol. 50, pp. 55–69, 2015.
- [106] D. P. Sokolis, ‘Time-course of axial residual strain remodeling and layer-specific thickening during aging along the human aorta’, *Journal of Biomechanics*, vol. 112, p. 110065, 2020.
- [107] M. R. Labrosse, E. R. Gerson, J. P. Veinot and C. J. Beller, ‘Mechanical characterization of human aortas from pressurization testing and a paradigm shift for circumferential residual stress’, *Journal of the Mechanical Behavior of Biomedical Materials*, vol. 17, pp. 44–55, 2013.
- [108] H. C. Han and Y. C. Fung, ‘Direct measurement of transverse residual strains in aorta’, *American Journal of Physiology-Heart and Circulatory Physiology*, vol. 270, no. 2, H750–H759, 1996.
- [109] M. Amabili, P. Balasubramanian, I. Bozzo, I. D. Breslajsky and G. Ferrari, ‘Layer-specific hyperelastic and viscoelastic characterization of human descending thoracic aortas’, *Journal of the Mechanical Behavior of Biomedical Materials*, vol. 99, pp. 27–46, 2019.
- [110] D. P. Sokolis, G. D. Savva, S. A. Papadodima and S. K. Kourkoulis, ‘Regional distribution of circumferential residual strains in the human aorta according to age and gender’, *Journal of the Mechanical Behavior of Biomedical Materials*, vol. 67, pp. 87–100, 2017.
- [111] J. T. Powell, N. Vine and M. Crossman, ‘On the accumulation of D-aspartate in elastin and other proteins of the aging aorta’, *Atherosclerosis*, vol. 97, no. 2-3, pp. 201–208, 1992.

-
- [112] S. D. Shapiro, S. K. Endicott, M. A. Province, J. A. Pierce and E. J. Campbell, ‘Marked longevity of human lung parenchymal elastic fibers deduced from prevalence of D-aspartate and nuclear-weapons related radiocarbon’, *Journal of Clinical Investigation*, vol. 87, no. 5, pp. 1828–1834, 1991.
- [113] C. Bellini, J. Ferruzzi, S. Roccabianca, E. S. Di Martino and J. D. Humphrey, ‘A Microstructurally Motivated Model of Arterial Wall Mechanics with Mechanobiological Implications’, *Annals of Biomedical Engineering*, vol. 42, no. 3, pp. 488–502, 2014.
- [114] N. Famaey, G. Sommer, J. Vander Sloten and G. A. Holzapfel, ‘Arterial clamping: Finite element simulation and in vivo validation’, *Journal of the Mechanical Behavior of Biomedical Materials*, vol. 12, pp. 107–118, 2012.
- [115] T. C. Gasser, C. A. J. Schulze-Bauer and G. A. Holzapfel, ‘A three-dimensional finite element model for arterial clamping’, *Journal of Biomechanical Engineering-Transactions of the Asme*, vol. 124, no. 4, pp. 355–363, 2002.
- [116] M. L. Raghavan, S. Trivedi, A. Nagaraj, D. D. McPherson and K. B. Chandran, ‘Three-dimensional finite element analysis of residual stress in arteries’, *Annals of Biomedical Engineering*, vol. 32, no. 2, pp. 257–263, 2004.
- [117] D. Balzani, J. Schröder and D. Gross, ‘Numerical simulation of residual stresses in arterial walls’, *Computational Materials Science*, vol. 39, no. 1, pp. 117–123, 2007.
- [118] S. de Putter, B. Wolters, M. C. M. Rutten, M. Breeuwer, F. A. Gerritsen and F. N. van de Vosse, ‘Patient-specific initial wall stress in abdominal aortic aneurysms with a backward incremental method’, *Journal of Biomechanics*, vol. 40, no. 5, pp. 1081–1090, 2007.
- [119] H. Weisbecker, D. M. Pierce and G. A. Holzapfel, ‘A generalized prestressing algorithm for finite element simulations of preloaded geometries with application to the aorta’, *International Journal for Numerical Methods in Biomedical Engineering*, vol. 30, no. 9, pp. 857–872, 2014.
- [120] M. L. Raghavan, B. S. Ma and M. F. Fillingner, ‘Non-invasive determination of zero-pressure geometry of arterial aneurysms’, *Annals of Biomedical Engineering*, vol. 34, no. 9, pp. 1414–1419, 2006.

-
- [121] M. W. Gee, C. Reeps, H. H. Eckstein and W. A. Wall, ‘Prestressing in finite deformation abdominal aortic aneurysm simulation’, *Journal of Biomechanics*, vol. 42, no. 11, pp. 1732–1739, 2009.
- [122] M. W. Gee, C. Förster and W. A. Wall, ‘A computational strategy for prestressing patient-specific biomechanical problems under finite deformation’, *International Journal for Numerical Methods in Biomedical Engineering*, vol. 26, no. 1, pp. 52–72, 2010.
- [123] J. Bols, J. Degroote, B. Trachet, B. Verheghe, P. Segers and J. Vierendeels, ‘Inverse modelling of image-based patient-specific blood vessels: Zero-pressure geometry and in vivo stress incorporation’, *ESAIM: Mathematical Modelling and Numerical Analysis*, vol. 47, no. 4, pp. 1059–1075, 2013.
- [124] M. Peirlinck, M. De Beule, P. Segers and N. Rebelo, ‘A modular inverse elastostatics approach to resolve the pressure-induced stress state for in vivo imaging based cardiovascular modeling’, *Journal of the Mechanical Behavior of Biomedical Materials*, vol. 85, pp. 124–133, 2018.
- [125] L. Cardamone, A. Valentín, J. F. Eberth and J. D. Humphrey, ‘Origin of axial prestretch and residual stress in arteries’, *Biomechanics and Modeling in Mechanobiology*, vol. 8, no. 6, pp. 431–446, 2009.
- [126] N. Famaey *et al.*, ‘Numerical simulation of arterial remodeling in pulmonary autografts’, *Zamm-Zeitschrift Fur Angewandte Mathematik Und Mechanik*, vol. 98, no. 12, pp. 2239–2257, 2018.
- [127] K. Vander Linden, M. Ghasemi, L. Maes, J. Vastmans and N. Famaey, ‘Layer-specific fiber distribution in arterial tissue modeled as a constrained mixture’, *International Journal for Numerical Methods in Biomedical Engineering*, vol. 39, no. 4, p. 13, 2023.
- [128] J. D. Humphrey and M. A. Schwartz, ‘Vascular Mechano-biology: Homeostasis, Adaptation, and Disease’, in (Annual Review of Biomedical Engineering), Yarmush, M. L., Ed., Annual Review of Biomedical Engineering. Annual Reviews, 2021, vol. 23, pp. 1–27.
- [129] S. M. Arribas, A. Hinek and M. C. Gonzalez, ‘Elastic fibres and vascular structure in hypertension’, *Pharmacology & Therapeutics*, vol. 111, no. 3, pp. 771–791, 2006.

-
- [130] M. Lefevre and R. B. Rucker, 'AORTA ELASTIN TURNOVER IN NORMAL AND HYPERCHOLESTEROLEMIC JAPANESE QUAIL', *Biochimica Et Biophysica Acta*, vol. 630, no. 4, pp. 519–529, 1980.
- [131] R. Nissen, G. J. Cardinale and S. Udenfriend, 'INCREASED TURNOVER OF ARTERIAL COLLAGEN IN HYPERTENSIVE RATS', *Proceedings of the National Academy of Sciences of the United States of America*, vol. 75, no. 1, pp. 451–453, 1978.
- [132] C. Karmonik *et al.*, 'Preliminary findings in quantification of changes in septal motion during follow-up of type B aortic dissections', *Journal of Vascular Surgery*, vol. 55, no. 5, 1419–U598, 2012.
- [133] E. K. Rodriguez, A. Hoger and A. D. McCulloch, 'STRESS-DEPENDENT FINITE GROWTH IN SOFT ELASTIC TISSUES', *Journal of Biomechanics*, vol. 27, no. 4, pp. 455–467, 1994.
- [134] J. D. Humphrey and K. R. Rajagopal, 'A constrained mixture model for growth and remodeling of soft tissues', *Mathematical Models & Methods in Applied Sciences*, vol. 12, no. 3, pp. 407–430, 2002.
- [135] C. Cyron, R. Aydin and J. Humphrey, 'A homogenized constrained mixture (and mechanical analog) model for growth and remodeling of soft tissue', *Biomechanics and Modeling in Mechanobiology*, vol. 15, no. 6, pp. 1389–1403, 2016.
- [136] L. Maes and N. Famaey, 'How to implement constrained mixture growth and remodeling algorithms for soft biological tissues', *Journal of the Mechanical Behavior of Biomedical Materials*, vol. 140, p. 11, 2023.
- [137] F. A. Braeu, A. Seitz, R. C. Aydin and C. J. Cyron, 'Homogenized constrained mixture models for anisotropic volumetric growth and remodeling', *Biomechanics and Modeling in Mechanobiology*, vol. 16, no. 3, pp. 889–906, 2017.
- [138] M. Y. Chong, B. Gu, B. T. Chan, Z. C. Ong, X. Y. Xu and E. Lim, 'Effect of intimal flap motion on flow in acute type B aortic dissection by using fluid-structure interaction', *International Journal for Numerical Methods in Biomedical Engineering*, vol. 36, no. 12, p. 22, 2020.

-
- [139] M. Alimohammadi, J. M. Sherwood, M. Karimpour, O. Agu, S. Balabani and V. Diaz-Zuccarini, ‘Aortic dissection simulation models for clinical support: fluid-structure interaction vs. rigid wall models’, *BioMedical Engineering OnLine*, vol. 14, no. 1, 2015.
- [140] H. Keramati, E. Birgersson, J. P. Ho, S. Kim, K. J. Chua and H. L. Leo, ‘The effect of the entry and re-entry size in the aortic dissection: a two-way fluid-structure interaction simulation’, *Biomechanics and Modeling in Mechanobiology*, vol. 19, no. 6, pp. 2643–2656, 2020.
- [141] W. T. Tan *et al.*, ‘Effect of Vessel Tortuosity on Stress Concentration at the Distal Stent-Vessel Interface: Possible Link With New Entry Formation Through Biomechanical Simulation’, *Journal of Biomechanical Engineering-Transactions of the Asme*, vol. 143, no. 8, p. 9, 2021.
- [142] X. X. Kan, T. Ma, J. Lin, L. Wang, Z. H. Dong and X. Y. Xu, ‘Patient-specific simulation of stent-graft deployment in type B aortic dissection: model development and validation’, *Biomechanics and Modeling in Mechanobiology*, vol. 20, no. 6, pp. 2247–2258, 2021.
- [143] X. C. Wang, M. H. Ghayesh, A. Kotousov, A. C. Zander, J. A. Dawson and P. J. Psaltis, ‘Fluid-structure interaction study for biomechanics and risk factors in Stanford type A aortic dissection’, *International Journal for Numerical Methods in Biomedical Engineering*, vol. 39, no. 8, p. 25, 2023.
- [144] M. Zhang, H. F. Liu, Z. X. Cai, C. R. Sun and W. Sun, ‘A novel framework for quantifying the subject-specific three-dimensional residual stress field in the aortic wall’, *Journal of the Mechanical Behavior of Biomedical Materials*, vol. 125, p. 11, 2022.
- [145] L. Wang, N. A. Hill, S. M. Roper and X. Y. Luo, ‘Modeling peeling- and pressure-driven propagation of arterial dissection’, *Journal of Engineering Mathematics*, vol. 109, no. 1, pp. 227–238, 2018.
- [146] L. Wang, S. M. Roper, N. A. Hill and X. Y. Luo, ‘Propagation of dissection in a residually-stressed artery model’, *Biomechanics and Modeling in Mechanobiology*, vol. 16, no. 1, pp. 139–149, 2017.

-
- [147] M. Rolf-Pissarczyk, K. W. Li, D. Fleischmann and G. A. Holzapfel, ‘A discrete approach for modeling degraded elastic fibers in aortic dissection’, *Computer Methods in Applied Mechanics and Engineering*, vol. 373, p. 21, 2021.
- [148] L. Maes, T. Vervenne, L. Van Hoof, E. A. V. Jones, F. Rega and N. Famaey, ‘Computational modeling reveals inflammation-driven dilatation of the pulmonary autograft in aortic position’, *Biomechanics and Modeling in Mechanobiology*, p. 14, 2023.
- [149] C. J. Cyron, J. S. Wilson and J. D. Humphrey, ‘Mechanobiological stability: a new paradigm to understand the enlargement of aneurysms?’, *Journal of the Royal Society Interface*, vol. 11, no. 100, p. 11, 2014.
- [150] S. Brandstaeter, S. L. Fuchs, J. Biehler, R. C. Aydin, W. A. Wall and C. J. Cyron, ‘Global Sensitivity Analysis of a Homogenized Constrained Mixture Model of Arterial Growth and Remodeling’, *Journal of Elasticity*, vol. 145, no. 1-2, pp. 191–221, 2021.
- [151] A. B. Ramachandra, M. Latorre, J. M. Szafron, A. L. Marsden and J. D. Humphrey, ‘Vascular adaptation in the presence of external support - A modeling study’, *Journal of the Mechanical Behavior of Biomedical Materials*, vol. 110, p. 10, 2020.
- [152] M. Latorre, M. R. Bersi and J. D. Humphrey, ‘Computational modeling predicts immuno-mechanical mechanisms of maladaptive aortic remodeling in hypertension’, *International Journal of Engineering Science*, vol. 141, pp. 35–46, 2019.
- [153] S. J. Mousavi, S. Farzaneh and S. Avril, ‘Patient-specific predictions of aneurysm growth and remodeling in the ascending thoracic aorta using the homogenized constrained mixture model’, *Biomechanics and Modeling in Mechanobiology*, vol. 18, no. 6, pp. 1895–1913, 2019.
- [154] N. Horvat, L. Virag, G. A. Holzapfel, J. Soric and I. Karsaj, ‘A finite element implementation of a growth and remodeling model for soft biological tissues: Verification and application to abdominal aortic aneurysms’, *Computer Methods in Applied Mechanics and Engineering*, vol. 352, pp. 586–605, 2019.
- [155] J. C. Wu and S. C. Shadden, ‘Coupled Simulation of Hemodynamics and Vascular Growth and Remodeling in a Subject-Specific Geometry’, *Annals of Biomedical Engineering*, vol. 43, no. 7, pp. 1543–1554, 2015.

-
- [156] L. Maes, A. S. Cloet, I. Fourneau and N. Famaey, ‘A homogenized constrained mixture model of restenosis and vascular remodelling after balloon angioplasty’, *Journal of the Royal Society Interface*, vol. 18, no. 178, p. 12, 2021.
- [157] J. Vastmans *et al.*, ‘Growth and remodeling in the pulmonary autograft: Computational evaluation using kinematic growth models and constrained mixture theory’, *International Journal for Numerical Methods in Biomedical Engineering*, vol. 38, no. 1, p. 24, 2022.
- [158] E. Gacek, R. R. Mahutga and V. H. Barocas, ‘Hybrid discrete-continuum multiscale model of tissue growth and remodeling’, *Acta Biomaterialia*, vol. 163, pp. 7–24, 2023.
- [159] I. M. Sobol, ‘Global sensitivity indices for nonlinear mathematical models and their Monte Carlo estimates’, *Mathematics and Computers in Simulation*, vol. 55, no. 1-3, pp. 271–280, 2001.
- [160] A. Saltelli, P. Annoni, I. Azzini, F. Campolongo, M. Ratto and S. Tarantola, ‘Variance based sensitivity analysis of model output. Design and estimator for the total sensitivity index’, *Computer Physics Communications*, vol. 181, no. 2, pp. 259–270, 2010.
- [161] E. Borgonovo, ‘A new uncertainty importance measure’, *Reliability Engineering & System Safety*, vol. 92, no. 6, pp. 771–784, 2007.
- [162] F. Sarrazin, F. Pianosi and T. Wagener, ‘Global Sensitivity Analysis of environmental models: Convergence and validation’, *Environmental Modelling & Software*, vol. 79, pp. 135–152, 2016.
- [163] J. Kudela and R. Matousek, ‘Recent advances and applications of surrogate models for finite element method computations: a review’, *Soft Computing*, vol. 26, no. 24, pp. 13 709–13 733, 2022.
- [164] C. E. Rasmussen and C. K. I. Williams, ‘Gaussian Processes for Machine Learning’. The MIT Press, 2005.
- [165] J. C. Helton and F. J. Davis, ‘Latin hypercube sampling and the propagation of uncertainty in analyses of complex systems’, *Reliability Engineering & System Safety*, vol. 81, no. 1, pp. 23–69, 2003.

-
- [166] M. D. McKay, R. J. Beckman and W. J. Conover, ‘A COMPARISON OF THREE METHODS FOR SELECTING VALUES OF INPUT VARIABLES IN THE ANALYSIS OF OUTPUT FROM A COMPUTER CODE’, *Technometrics*, vol. 21, no. 2, pp. 239–245, 1979.
- [167] K. Baumler, J. Zimmermann, D. B. Ennis, A. L. Marsden and D. Fleischmann, ‘Hemodynamic Effects of Entry Versus Exit Tear Size and Tissue Stiffness in Simulations of Aortic Dissection’, *Computer Methods, Imaging and Visualization in Biomechanics and Biomedical Engineering Ii*, vol. 38, pp. 143–152, 2023.
- [168] H. Keramati, E. Birgersson, S. Kim, J. P. Ho and H. L. Leo, ‘Using a reduced-order model to investigate the effect of the heart rate on the aortic dissection’, *International Journal for Numerical Methods in Biomedical Engineering*, vol. 38, no. 6, p. 15, 2022.
- [169] A. Jafarinia *et al.*, ‘Morphological parameters affecting false lumen thrombosis following type B aortic dissection: a systematic study based on simulations of idealized models’, *Biomechanics and Modeling in Mechanobiology*, p. 20, 2023.
- [170] J. O. Campos, R. M. Guedes, Y. B. Werneck, L. P. S. Barra, R. W. dos Santos and B. M. Rocha, ‘Polynomial chaos expansion surrogate modeling of passive cardiac mechanics using the Holzapfel-Ogden constitutive model’, *Journal of Computational Science*, vol. 71, p. 13, 2023.
- [171] L. Gheysen, L. Maes, N. Famaey and P. Segers, ‘Pulse wave velocity: A clinical measure to aid material parameter estimation in computational arterial biomechanics’, *Journal of Biomechanics*, vol. 149, pp. 1–17, 2023.
- [172] H. Fehervary, M. Smoljkic, J. V. Sloten and N. Famaey, ‘Planar biaxial testing of soft biological tissue using rakes: A critical analysis of protocol and fitting process’, *Journal of the Mechanical Behavior of Biomedical Materials*, vol. 61, pp. 135–151, 2016.
- [173] I. Masson, P. Boutouyrie, S. Laurent, J. D. Humphrey and M. Zidi, ‘Characterization of arterial wall mechanical behavior and stresses from human clinical data’, *Journal of Biomechanics*, vol. 41, no. 12, pp. 2618–2627, 2008.

-
- [174] C. A. J. Schulze-Bauer and G. A. Holzapfel, ‘Determination of constitutive equations for human arteries from clinical data’, *Journal of Biomechanics*, vol. 36, no. 2, pp. 165–169, 2003.
- [175] J. Stalhand, ‘Determination of human arterial wall parameters from clinical data’, *Biomechanics and Modeling in Mechanobiology*, vol. 8, no. 2, pp. 141–148, 2009.
- [176] A. Wittek *et al.*, ‘In vivo determination of elastic properties of the human aorta based on 4D ultrasound data’, *Journal of the Mechanical Behavior of Biomedical Materials*, vol. 27, pp. 167–183, 2013.
- [177] M. L. Liu *et al.*, ‘Identification of in vivo nonlinear anisotropic mechanical properties of ascending thoracic aortic aneurysm from patient-specific CT scans’, *Scientific Reports*, vol. 9, pp. 1–13, 2019.
- [178] M. Smoljkic *et al.*, ‘Comparison of in vivo vs. ex situ obtained material properties of sheep common carotid artery’, *Medical Engineering & Physics*, vol. 55, pp. 16–24, 2018.
- [179] P. Segers, E. R. Rietzschel and J. A. Chirinos, ‘How to measure arterial stiffness in humans’, *Arteriosclerosis Thrombosis and Vascular Biology*, vol. 40, no. 5, pp. 1034–1043, 2020.
- [180] C. Vlachopoulos, K. Aznaouridis and C. Stefanadis, ‘Prediction of cardiovascular events and all-cause mortality with arterial stiffness A systematic review and meta-analysis’, *Journal of the American College of Cardiology*, vol. 55, no. 13, pp. 1318–1327, 2010.
- [181] T. R. V. for Arterial Stiffness’ collaboration, ‘Determinants of pulse wave velocity in healthy people and in the presence of cardiovascular risk factors: ’establishing normal and reference values’’, *European Heart Journal*, vol. 31, no. 19, pp. 2338–2350, 2010.
- [182] E. Hermeling, K. D. Reesink, L. M. Kornmann, R. S. Reneman and A. P. G. Hoeks, ‘The dicrotic notch as alternative time-reference point to measure local pulse wave velocity in the carotid artery by means of ultrasonography’, *Journal of Hypertension*, vol. 27, no. 10, pp. 2028–2035, 2009.
- [183] L. Marais *et al.*, ‘Arterial stiffness assessment by shear wave elastography and ultrafast pulse wave imaging: comparison with reference techniques in normotensives and hypertensives’, *Ultrasound in Medicine and Biology*, vol. 45, no. 3, pp. 758–772, 2019.

-
- [184] B. L. McComb, R. F. Munden, F. H. Duan, A. A. Jain, C. Tuttle and C. Chiles, ‘Normative reference values of thoracic aortic diameter in American College of Radiology Imaging Network (ACRIN 6654) arm of National Lung Screening Trial’, *Clinical Imaging*, vol. 40, no. 5, pp. 936–943, 2016.
- [185] R. W. Ogden, ‘Nonlinear continuum mechanics and modeling the elasticity of soft biological tissues with a focus on artery walls’, *Biomechanics: Trends in Modeling and Simulation*, vol. 20, pp. 83–156, 2017.
- [186] M. Jadidi *et al.*, ‘Mechanical and structural changes in human thoracic aortas with age’, *Acta Biomaterialia*, vol. 103, pp. 172–188, 2020.
- [187] J. L. Hebert *et al.*, ‘Relation between aortic diastolic pressure and mean aortic pressure in adults’, *American Journal of Cardiology*, vol. 76, no. 4, pp. 301–306, 1995.
- [188] F. Cuomo, S. Roccabianca, D. Dillon-Murphy, N. Xiao, J. D. Humphrey and C. A. Figueroa, ‘Effects of age-associated regional changes in aortic stiffness on human hemodynamics revealed by computational modeling’, *Plos One*, vol. 12, no. 3, p. 21, 2017.
- [189] C. W. Huang, D. Guo, F. Lan, H. J. Zhang and J. W. Luo, ‘Noninvasive measurement of regional pulse wave velocity in human ascending aorta with ultrasound imaging: an in-vivo feasibility study’, *Journal of Hypertension*, vol. 34, no. 10, pp. 2026–2037, 2016.
- [190] G. Soulat *et al.*, ‘Changes in segmental pulse wave velocity of the thoracic aorta with age and left ventricular remodeling. An MRI 4D flow study’, *Journal of Hypertension*, vol. 38, no. 1, pp. 118–126, 2020.
- [191] H. B. Atabek, ‘Wave propagation through a viscous fluid contained in a tethered initially stressed orthotropic elastic tube’, *Biophysical Journal*, vol. 8, no. 5, pp. 626–649, 1968.
- [192] M. R. Bersi, C. Bellini, J. Wu, K. R. C. Montaniel, D. G. Harrison and J. D. Humphrey, ‘Excessive adventitial remodeling leads to early aortic maladaptation in angiotensin-induced hypertension’, *Hypertension*, vol. 67, no. 5, pp. 890–896, 2016.
- [193] S. Hodis, ‘Pulse wave velocity as a diagnostic index: The effect of wall thickness’, *Physical Review E*, vol. 97, no. 6, p. 8, 2018.

-
- [194] K. Jagielska, D. Trzupek, M. Lepers, A. Pelc and P. Zielinski, ‘Effect of surrounding tissue on propagation of axisymmetric waves in arteries’, *Physical Review E*, vol. 76, no. 6, p. 8, 2007.
- [195] L. Gheysen, L. Maes, A. Caenen, P. Segers, M. Peirlinck and N. Famaey, ‘Uncertainty quantification of the wall thickness and stiffness in an idealized dissected aorta’, *Journal of the Mechanical Behavior of Biomedical Materials*, vol. 151, p. 106370, 2024.
- [196] B. Rylski *et al.*, ‘How does descending aorta geometry change when it dissects?’, *European Journal of Cardio-Thoracic Surgery*, vol. 53, no. 4, pp. 815–821, 2018.
- [197] T. Yamauchi *et al.*, ‘Equations for Estimating the Predissected Diameter of the Descending Aorta From Computed Tomographic Images at the Onset of Aortic Dissection’, *Journal of the American Heart Association*, vol. 7, no. 13, pp. 1–14, 2018.
- [198] G. Logghe *et al.*, ‘Outflow Through Aortic Side Branches Drives False Lumen Patency in Type B Aortic Dissection’, *Frontiers in Cardiovascular Medicine*, vol. 8, p. 11, 2021.
- [199] A. L. M. Eikendal *et al.*, ‘Sex, body mass index, and blood pressure are related to aortic characteristics in healthy, young adults using magnetic resonance vessel wall imaging: the AMBITYON study’, *Magnetic Resonance Materials in Physics Biology and Medicine*, vol. 31, no. 1, pp. 173–182, 2018.
- [200] S. Gao *et al.*, ‘Quantification of Common Carotid Artery and Descending Aorta Vessel Wall Thickness From MR Vessel Wall Imaging Using a Fully Automated Processing Pipeline’, *Journal of Magnetic Resonance Imaging*, vol. 45, no. 1, pp. 215–228, 2017.
- [201] A. E. Li *et al.*, ‘Using MRI to assess aortic wall thickness in the multiethnic study of atherosclerosis: Distribution by race, sex, and age’, *American Journal of Roentgenology*, vol. 182, no. 3, pp. 593–597, 2004.
- [202] V. Mani *et al.*, ‘Cardiovascular magnetic resonance parameters of atherosclerotic plaque burden improve discrimination of prior major adverse cardiovascular events’, *Journal of Cardiovascular Magnetic Resonance*, vol. 11, 2009.
- [203] B. Mensel *et al.*, ‘MRI-based Determination of Reference Values of Thoracic Aortic Wall Thickness in a General Population’, *European Radiology*, vol. 24, no. 9, pp. 2038–2044, 2014.

-
- [204] M. Peirlinck *et al.*, ‘An in silico biomechanical analysis of the stent-esophagus interaction’, *Biomechanics and Modeling in Mechanobiology*, vol. 17, no. 1, pp. 111–131, 2018.
- [205] GPy, *Gpy: A gaussian process framework in python*, Generic, 2012.
- [206] J. Herman and W. Usher, ‘SALib: An open-source Python library for sensitivity analysis’, *Journal of Open Source Software*, vol. 2, no. 9, p. 97, 2017.
- [207] S. Pirola *et al.*, ‘4-D Flow MRI-Based Computational Analysis of Blood Flow in Patient-Specific Aortic Dissection’, *Ieee Transactions on Biomedical Engineering*, vol. 66, no. 12, pp. 3411–3419, 2019.
- [208] S. F. Yang *et al.*, ‘Abdominal Aortic Intimal Flap Motion Characterization in Acute Aortic Dissection: Assessed with Retrospective ECG-Gated Thoracoabdominal Aorta Dual-Source CT Angiography’, *Plos One*, vol. 9, no. 2, p. 9, 2014.
- [209] M. Ferraro, B. Trachet, L. Aslanidou, H. Fehervary, P. Segers and N. Stergiopoulos, ‘Should We Ignore What We Cannot Measure? How Non-Uniform Stretch, Non-Uniform Wall Thickness and Minor Side Branches Affect Computational Aortic Biomechanics in Mice’, *Annals of Biomedical Engineering*, vol. 46, no. 1, pp. 159–170, 2018.
- [210] E. Georgakarakos *et al.*, ‘The Role of Geometric Parameters in the Prediction of Abdominal Aortic Aneurysm Wall Stress’, *European Journal of Vascular and Endovascular Surgery*, vol. 39, no. 1, pp. 42–48, 2010.
- [211] G. A. Holzapfel, J. A. Niestrawska, R. W. Ogden, A. J. Reinisch and A. J. Schriefl, ‘Modelling non-symmetric collagen fibre dispersion in arterial walls’, *Journal of the Royal Society Interface*, vol. 12, no. 106, p. 14, 2015.
- [212] H. Dal, A. K. Acan, C. Durcan and M. Hossain, ‘An In Silico-Based Investigation on Anisotropic Hyperelastic Constitutive Models for Soft Biological Tissues’, *Archives of Computational Methods in Engineering*, p. 32, 2023.
- [213] J. A. Niestrawska, D. C. Haspinger and G. A. Holzapfel, ‘The influence of fiber dispersion on the mechanical response of aortic tissues in health and disease: a computational study’, *Computer Methods in Biomechanics and Biomedical Engineering*, vol. 21, no. 2, 2018.

-
- [214] D. Wu, Y. H. Shen, L. Russell, J. S. Coselli and S. A. LeMaire, ‘Molecular mechanisms of thoracic aortic dissection’, *Journal of Surgical Research*, vol. 184, no. 2, pp. 907–924, 2013.
- [215] S. Sherifova and G. A. Holzapfel, ‘Biomechanics of aortic wall failure with a focus on dissection and aneurysm: A review’, *Acta Biomaterialia*, vol. 99, pp. 1–17, 2019.
- [216] L. Gheysen, L. Maes, N. Famaey and P. Segers, ‘Growth and remodeling of the dissected membrane in an idealized dissected aorta model’, *Biomechanics and Modeling in Mechanobiology*, p. 19, 2023.
- [217] A. Valentin and J. D. Humphrey, ‘Parameter Sensitivity Study of a Constrained Mixture Model of Arterial Growth and Remodeling’, *Journal of Biomechanical Engineering-Transactions of the Asme*, vol. 131, no. 10, p. 11, 2009.
- [218] J. D. Drews *et al.*, ‘Spontaneous reversal of stenosis in tissue-engineered vascular grafts’, *Science Translational Medicine*, vol. 12, no. 537, p. 13, 2020.
- [219] M. Latorre and J. D. Humphrey, ‘Modeling mechano-driven and immuno-mediated aortic maladaptation in hypertension’, *Biomechanics and Modeling in Mechanobiology*, vol. 17, no. 5, pp. 1497–1511, 2018.
- [220] S. Miyahara *et al.*, ‘Long-term follow-up of acute type B aortic dissection: Ulcer-like projections in thrombosed false lumen play a role in late aortic events’, *Journal of Thoracic and Cardiovascular Surgery*, vol. 142, no. 2, E25–E31, 2011.
- [221] E. Sueyoshi, I. Sakamoto and M. Uetani, ‘Growth Rate of Affected Aorta in Patients With Type B Partially Closed Aortic Dissection’, *Annals of Thoracic Surgery*, vol. 88, no. 4, pp. 1251–1257, 2009.
- [222] J. L. Tolenaar *et al.*, ‘Morphologic predictors of aortic dilatation in type B aortic dissection’, *Journal of Vascular Surgery*, vol. 58, no. 5, pp. 1220–1225, 2013.
- [223] M. Berezowski *et al.*, ‘Early aortic growth in acute descending aortic dissection’, *Interactive Cardiovascular and Thoracic Surgery*, vol. 34, no. 5, pp. 857–864, 2022.
- [224] A. M. Kelly *et al.*, ‘Aortic growth rates in chronic aortic dissection’, *Clinical Radiology*, vol. 62, no. 9, pp. 866–875, 2007.

-
- [225] K. J. Blount and K. D. Hagspiel, ‘Aortic Diameter, True Lumen, and False Lumen Growth Rates in Chronic Type B Aortic Dissection’, *American Journal of Roentgenology*, vol. 192, no. 5, W222–W229, 2009.
- [226] J. M. Song *et al.*, ‘Long-term predictors of descending aorta Aneurysmal change in patients with aortic dissection’, *Journal of the American College of Cardiology*, vol. 50, no. 8, pp. 799–804, 2007.
- [227] C. O. Horgan and J. G. Murphy, ‘On the tension-compression switch hypothesis in arterial mechanics’, *Journal of the Mechanical Behavior of Biomedical Materials*, vol. 103, p. 13, 2020.
- [228] C. Menichini, Z. Cheng, R. G. J. Gibbs and X. Y. Xu, ‘A computational model for false lumen thrombosis in type B aortic dissection following thoracic endovascular repair’, *Journal of Biomechanics*, vol. 66, no. C, pp. 36–43, 2018.
- [229] M. Y. Chong *et al.*, ‘An integrated fluid-structure interaction and thrombosis model for type B aortic dissection’, *Biomechanics and Modeling in Mechanobiology*, vol. 21, no. 1, pp. 261–275, 2022.
- [230] M. Akagi *et al.*, ‘Deep learning reconstruction improves image quality of abdominal ultra-high-resolution CT’, *European Radiology*, vol. 29, no. 11, pp. 6163–6171, 2019.
- [231] K. Ogawa *et al.*, ‘Visualization of small visceral arteries on abdominal CT angiography using ultra-high-resolution CT scanner’, *Japanese Journal of Radiology*, vol. 39, no. 9, pp. 889–897, 2021.
- [232] A. C. Kwan, A. Pourmorteza, D. Stutman, D. A. Bluemke and J. A. C. Lima, ‘Next-Generation Hardware Advances in CT: Cardiac Applications’, *Radiology*, vol. 298, no. 1, pp. 3–17, 2021.
- [233] E. Di Cesare *et al.*, ‘CT and MR imaging of the thoracic aorta’, *Open Medicine*, vol. 11, no. 1, pp. 143–151, 2016.
- [234] C. A. Nienaber, ‘The role of imaging in acute aortic syndromes’, *European Heart Journal-Cardiovascular Imaging*, vol. 14, no. 1, pp. 15–23, 2013.
- [235] S. Parikh *et al.*, ‘Biomechanical Characterisation of Thoracic Ascending Aorta with Preserved Pre-Stresses’, *Bioengineering-Basel*, vol. 10, no. 7, p. 16, 2023.

-
- [236] M. L. Liu, L. Liang and W. Sun, ‘A new inverse method for estimation of in vivo mechanical properties of the aortic wall’, *Journal of the Mechanical Behavior of Biomedical Materials*, vol. 72, pp. 148–158, 2017.
- [237] E. M. J. van Disseldorp, N. J. Petterson, M. C. M. Rutten, F. N. van de Vosse, M. van Sambeek and R. G. P. Lopata, ‘Patient Specific Wall Stress Analysis and Mechanical Characterization of Abdominal Aortic Aneurysms Using 4D Ultrasound’, *European Journal of Vascular and Endovascular Surgery*, vol. 52, no. 5, pp. 635–642, 2016.
- [238] A. C. Akyildiz *et al.*, ‘A Framework for Local Mechanical Characterization of Atherosclerotic Plaques: Combination of Ultrasound Displacement Imaging and Inverse Finite Element Analysis’, *Annals of Biomedical Engineering*, vol. 44, no. 4, pp. 968–979, 2016.
- [239] J. Vappou, J. W. Luo and E. E. Konofagou, ‘Pulse Wave Imaging for Noninvasive and Quantitative Measurement of Arterial Stiffness In Vivo’, *American Journal of Hypertension*, vol. 23, no. 4, pp. 393–398, 2010.

Academic curriculum vitae

CURRICULUM VITAE

Lise Gheysen (°Kortrijk, Oktober 1995) graduated (*magna cum laude*) as a biomedical engineer at the Catholic University of Leuven in 2018. Since August 2018, she has been part of the ‘Biophysical Models for Medical Applications’ (BioMMedA) lab at Ghent University and the ‘Soft Tissue Biomechanics’ (STB) lab at the Catholic University of Leuven. Under the supervision of professor Patrick Segers, professor Nele Famaey and professor Mathias Peirlinck, she has been investigating the uncertainty of biomechanical modeling of the aortic wall in type B dissections. Lise is first author of three articles in international peer-reviewed journals and six abstracts in international conferences. The PhD project was supported by a grant of the Research Foundation Flanders.

PUBLICATIONS IN INTERNATIONAL PEER-REVIEWED JOURNALS

- L. Gheysen, L. Maes, N. Famaey and P. Segers, ‘Pulse wave velocity: A clinical measure to aid material parameter estimation in computational arterial biomechanics’, *Journal of Biomechanics*, vol. 149, pp. 1–17, 2023.
- L. Gheysen, L. Maes, A. Caenen, P. Segers, M. Peirlinck and N. Famaey, ‘Uncertainty quantification of the wall thickness and stiffness in an idealized dissected aorta’, *Journal of the Mechanical Behavior of Biomedical Materials*, vol. 151, pp. 1–16, 2024.
- L. Gheysen, L. Maes, N. Famaey and P. Segers, ‘Growth and remodeling of the dissected membrane in an idealized dissected aorta model’, *Biomechanics and Modeling in Mechanobiology*, pp. 1–19, 2023.

